

KfK 4677  
EUR 11397 EN  
November 1989

# **Nuclear Fusion Project Semi-annual Report of the Association KfK/EURATOM**

**April 1989 – September 1989**

**Projekt Kernfusion**

**Kernforschungszentrum Karlsruhe**



KfK 4677  
EUR 11397 EN  
November 1989

**Nuclear Fusion Project  
Semi-annual Report of the  
Association KfK/EURATOM  
April 1989 - September 1989**

compiled by  
G. Kast

**Kernforschungszentrum Karlsruhe**

Als Manuskript vervielfältigt  
Für diesen Bericht behalten wir uns alle Rechte vor

Kernforschungszentrum Karlsruhe GmbH  
Postfach 3640, 7500 Karlsruhe 1

ISSN 0303-4003

## Preface

Fusion Technology is the main heading for the work of the KfK-EURATOM Association. Contributions address all parts of the recently reorganized European Fusion Technology Programme.

The NET / ITER design is supported by delegation of personnel and by performance of study contracts. R + D for the NET basic machine highlights areas like remote maintenance, fuel cycle technology and superconducting magnets. More emphasis has recently been placed on testing of plasma facing components. Studies of safety and environmental impact refer to tokamak subsystems as magnets and blankets, but also more generally to investigations of radioactive releases and their consequences. The development of breeding blankets with reactor specifications was given in the hands of two European development groups, KfK being a partner of the liquid metal blanket as well as of the solid breeder blanket groups. The material program, as far as metals are concerned, is concentrated on fulfilling the needs of a demonstration reactor. The other component of the materials programme, the protection materials for the first wall and electrical insulators, are already required for NET / ITER. Gyrotron development aims at supplying NET / ITER with heating power but the results of the current program are already applicable to near term plasma experiments.

The overall effort for fusion takes about 20 % of KfK's research capacity. 9 departments participate in the Nuclear Fusion Program. On the national level KfK cooperates with IPP Garching as "Entwicklungsgemeinschaft Kernfusion". KFA is a partner in the field of structural and breeder materials. Beyond the intensive collaboration among the European research installations the fusion project maintains links to research laboratories in USA, Japan and in the Soviet Union.

J.E. Vetter

## Contents

### **Report on the Technology Programme for NET**

#### Plasma Facing Components

PSM 3	Pre- and Post-Irradiation Low Cycle Fatigue of Reference 316 L Steel and Welds	1
PSM 8	Coatings and Surface Effects on 316 L	4
PPM 1	Material Characterization and Neutron Irradiation Effects in Graphites, CFCs and Ceramic Composites	5
PPM 4	Material Characterization and Irradiation Effects in Ceramic Insulators	6
PDT 1	Thermomechanical Tests of First Wall Mock-ups	8
PDT 2	Tests of Divertor Samples and Mock-ups	9

#### Magnets

MTC 1	Industrial Manufacturing of a few km of React-and-Wind Nb <sub>3</sub> Sn Conductors and of TF Model Coils	11
MOC 1	Manufacturing and Testing of Short Length Full -Size NbTi Conductor (Outer Coil)	13
MOC 2	Design and Manufacture of one Outer Coil (NbTi) and Installation in TORE SUPRA	18
MTF 2	Upgrade of the TOSKA Facility for Model Coils Testing	19
MSA 1	Safety Relevant Models and Experiments for NET Magnets	22

#### Tritium (Fuel Cycle)

TPV 1	Development of Solid Particle Separators for Plasma Exhaust	24
TPV 2	Optimization of the Cryogenic Vacuum Pumping of Helium	26
TEP 2	Plasma Exhaust Processing Alternative Options	28
TEP 3	Tritium Storage	32

#### Nuclear Engineering / Basic Blanket

NSN 1	Neutronics Data Base for Shielding	34
-------	------------------------------------	----

#### Remote Handling / Maintenance

RHS 1	Qualification of Standard Components	35
RHS 2	Material Tests for Remote Maintenance Equipment	37
RHS 3	Mock-up of In-Vessel Components and Test Facilities	38

RHI 1	Blanket Handling Device (BHD) .....	39
RHT 1	In-Vessel Handling Unit (IVHU) .....	40

**Safety and Environment**

SEP 2	Environmental Impact of Tritium and Activation Products .....	45
SEA 1	Specific Safety Related Recommendations for the Design .....	47
SEA 3	Reference Accident Sequences .....	48

**Blankets**

**BS - Solid Breeder Test Blankets**

BS DE-D-1	Solid Breeder Test Blanket Design .....	49
BS BR-D-1	Preparation of Ceramic Breeder Materials .....	51
BS BR-D-2	Characterization .....	52
BS BR-D-3	Irradiation Testing .....	53
BS BR-D-4	Tritium Release .....	55
BS BR-D-5	Physical and Mechanical Properties .....	57
BS BR-D-6	Compatibility .....	58
BS BR-D-7	Constitution, Interaction with Water Vapour .....	59
BS BR-D-8	Thermomechanical Characterization .....	60
BS NN-D-1	Helium Blanket Test Loop .....	61

**BL - Liquid Metal Test Blankets**

BL DE-D-1	Liquid Metal Test Blanket Design .....	62
BL PC-D-1	Corrosion of Structural Materials in Flowing Pb-17Li .....	65
BL EX-D-1	Tritium Extraction by Permeation and Cold Trapping .....	66
BL EX-D-2	Tritium Extraction by Solid Getters .....	67
BL MH-D-1	Liquid Metal MHD .....	68

**Long Term Program**

LAM 2.1	LAM Element Activation .....	70
LAM 3	Development of Low Activation Ferritic-Martensitic Steels .....	71

MAT 1.9	Pre- and Post-Irradiation Fatigue Properties of 1.4914 Martensitic Steel (MANET)	72
MAT 1.11	Post-Irradiation Fracture Toughness of MANET Steel	74
MAT 2.2	In-Pile-Creep-Fatigue Testing of MANET	22
MAT 9.2	Investigation of Fatigue under Dual-Beam Irradiations	77
<b>Development of ECRH Power Sources</b>		<b>80</b>
<b>NET Study Contracts</b>		
	Electrical Connectors for Remote Handling	82
	Study of a Plasma Exhaust Purification System for NET Based on Catalytic Reduction of Impurities: Phase 2 - Engineering Study	82
	NET Remote Workstation	82
	Doses due to Tritium Releases by NET-Data Base and Relevant Parameters	84
	Fatigue Characterization of Jacket Materials at 4 K	85
	Doses due to Activation Product Releases by NET Plasma Facing Components - Review and Procurement of Data Base	87
	Vacuum Pumping Support	87
	Fracture-Mechanical Investigation for the NET Microwave Window	87
<b>Appendix I: Allocation of Tasks</b>		<b>89</b>
<b>Appendix II: Table of NET Contracts</b>		<b>92</b>
<b>Appendix III: KfK Departments contributing to the Fusion Project</b>		<b>93</b>
<b>Appendix IV: Fusion Project Management Staff</b>		<b>94</b>



### PSM 3 Pre- and Post-Irradiation Low Cycle Fatigue of Reference 316 L Steel and Welds

#### Subtask 3.9

The cyclic thermal loading of the first wall in a fusion reactor causes cyclic multiaxial stress states. These cyclic stresses may initiate cracks and failure of the structure. To understand crack initiation and propagation caused by these multiaxial thermocyclic loads and to investigate, if there is an other damage than under equivalent uniaxial isothermal loading, experiments have to be performed under multiaxial cyclic thermal and isothermal stresses.

The most exposed region in the FW is the inner side of the cooling tube. Fig. 1 shows the stress distribution caused by

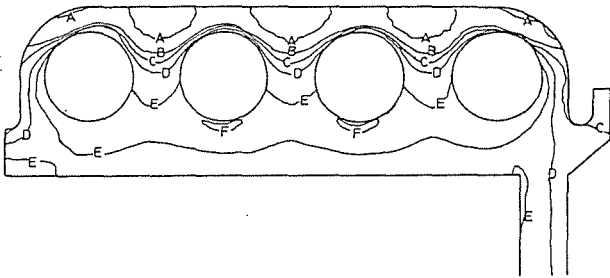


Fig. 1: Axial thermal stress distribution in the FW calculated with a plasticity model. Lines of equal stresses parallel to the axes of the holes:  
A: -225 MPa    D: 0 MPa  
B: -150 MPa    E: 75 MPa  
C: -75 MPa    F: 150 MPa

temperature gradients in a FW-model calculated in task N1. The highest tensile amplitudes arise at the inner side of the cooling tube. However there are high amplitudes at higher temperatures at the FW surface, too.

Therefore, it is useful to investigate the crack initiation on the inner and outer surface of tubes loaded in a similar manner.

#### 1. Thermal fatigue of the reference steel 1.4436

The thermal fatigue of the steel 1.4436 was investigated on watercooled tubes, comparable to the first wall. In these specimens a biaxial stress state arises by heating from the outside. For the first comparison isothermal tests with uniaxial stresses were carried out, too.

The equipment for thermal fatigue testing is a setup newly developed within the last years.

Tubular specimens are used. By induction heating the outer surface temperature rises from 100°C to 375°C within 2.2 s. For cooling, deionized water is streaming through the tube. Free thermal expansion of the specimen is possible. The temperature gradients in the wall, caused by the rapid heating, produce cyclic thermal strains. Fig. 2 shows the schematic setup.

The temperature distribution in the wall of the tube was calculated with the help of temperature measurements on the surfaces and the volumetric distribution of the heat induction. Then, the periodic strains in the wall were calculated for elastic and for a simple plastic material response. Fig. 3 shows the calculated strains in the plastic case.

It is noteworthy that high strain amplitudes arise similar to the FW at the heated outer side and at the inner side of the tube. The strains lead to crack initiation after about 30,000 cycles and to failure by wall penetrating cracks after about 100,000 cycles. During the test, crack initiation and growth was observed on the inner side and measured by an endoscope. On the outer side which has higher strain amplitudes but higher temperatures, too, no crack initiation was found. Therefore, in the FW the inner side of the cooling tube seems to be critical.

The failure of the tubes caused by wall-penetrating cracks is shown in Fig. 4 for the calculated equivalent strain. For comparison the measured failure of specimen under uniaxial isothermal loads is plotted, too. The first comparison shows that the failure occurs a little earlier in the thermal fatigue tests. Yet it isn't clear whether this is caused by the thermal loading or by the multiaxial stress state.

#### 2. Thermal and isothermal fatigue of AISI 316 LSPH under multiaxial stress states

In the thermal fatigue tests on steel 1.4436 shorter lifetimes have been found than in uniaxial isothermal tests. In further investigations thermal fatigue tests will be performed on AISI 316 LSPH. The influence of multiaxial stresses will be investigated separately.

For comparison LCF specimen for uniaxial tests were fabricated from plates of AISI 316 LSPH. Fatigue tests under isothermal conditions are under work.

To perform isothermal tests under similar multiaxial conditions as in thermocyclic tests an experimental set up is in development to test tubes under tensile loads and internal/external pressure. Fig. 5 shows the schematic setup. Two servocontrolled test machines produce tension and internal pressure controlled by extensometers. Since the circumferential stress is produced by the pressure difference,

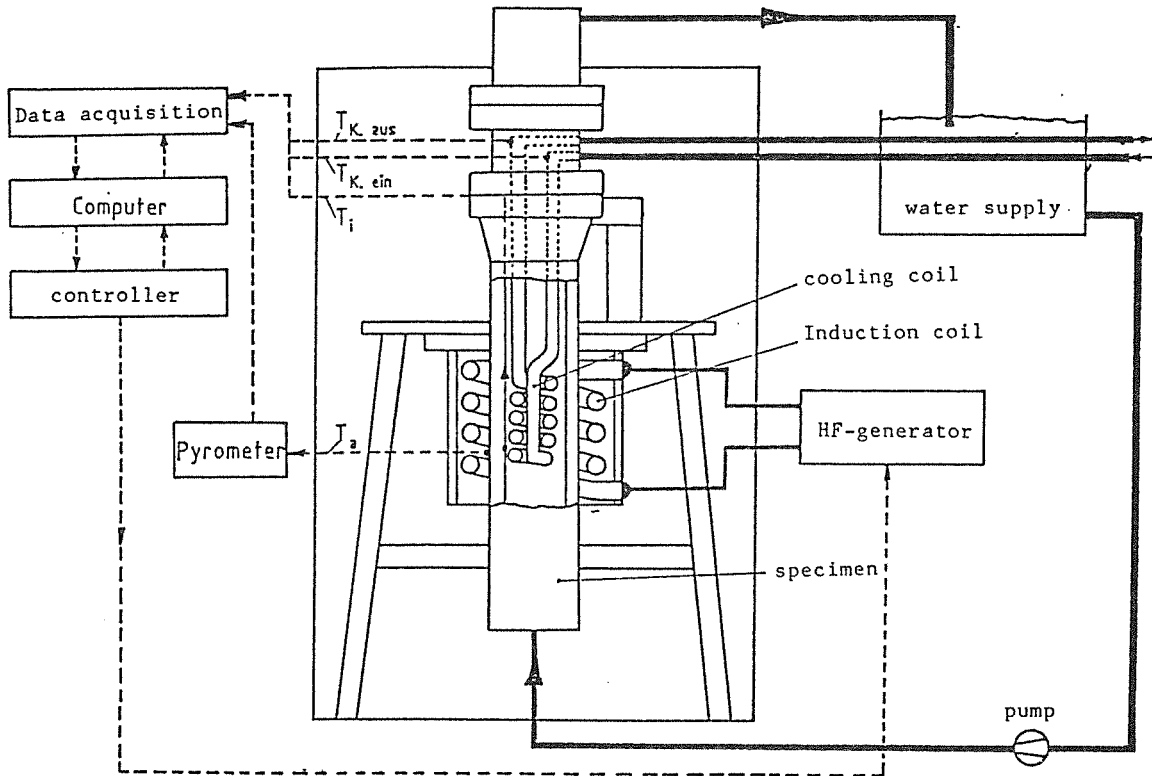


Fig. 2: Schematic sketch of the experimental set up for thermal fatigue tests

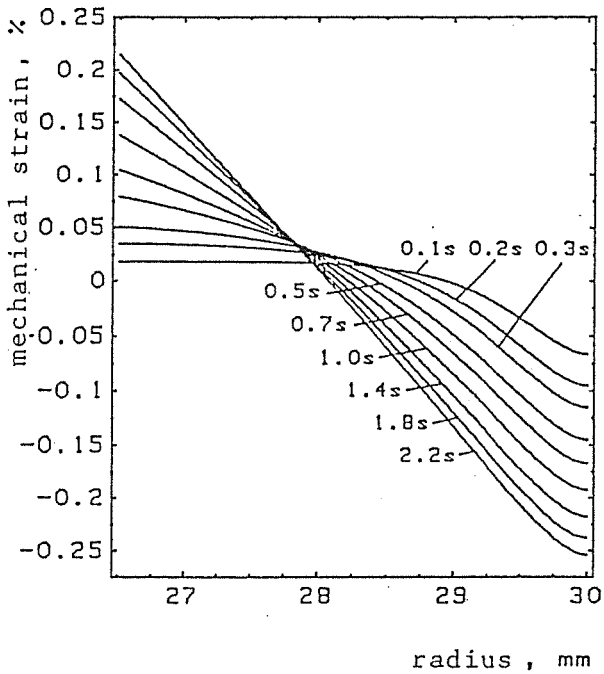


Fig. 3: Calculated principal strain in axial direction in the tube as a function of the radius for different times after the beginning of the heating

a constant external pressure is sufficient. The first tests on dummies without external pressure are under work.

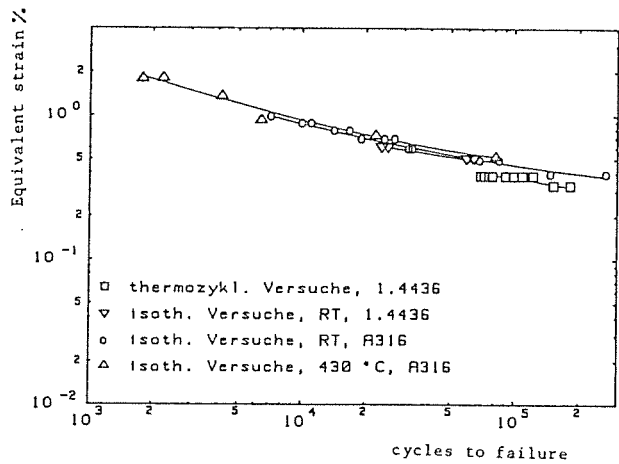


Fig. 4: Cycles to failure of specimens under thermal multiaxial and isothermal uniaxial fatigue as a function of the cyclic range of the equivalent strain

To buy tubes of 316 LSPH different dealers were contacted. No tubes with SPH fabrication specification were found in sufficient quantities. Different 316 L tubes were investigated to get knowledge about their chemical composition. Measurements to obtain the parts of  $\delta$ -ferrite and nitrogen were performed. Specimens with chemical composition near to the SPH specification are now in fabrication to compare the fatigue behaviour with 316 LSPH. Simultaneously the fabrication of tubes from raw material was ordered.

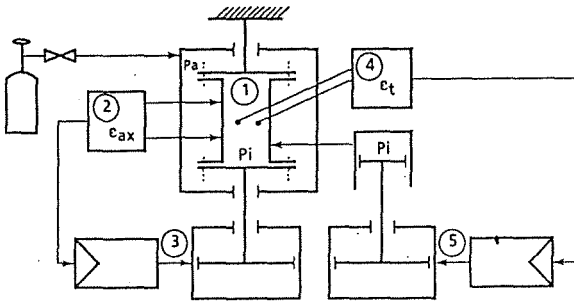


Fig. 5: Schematic sketch of the experimental setup for biaxial fatigue tests

1. Specimen is a tube with internal  $p_i$  and external  $p_a$  pressure
2. Extensometer for axial elongation
3. Machine for tension tests
4. Extensometer for tangential elongation
5. Machine to produce the internal pressure

Staff:

E. Diegele  
T. Fett  
W. Hartlieb  
J. Neumann  
B. Schinke  
E. Wiens

## PSM 8      Coatings and Surface Effects on 316 L

### Subtask 8.2

The objective of this investigation is both to study the adherence and integrity of the coatings and to investigate a possible influence of surface modifications on crack initiation in the base material.

The thermal cycle fatigue tests have to be performed with tubes made of austenitic steel, preferably AISI 316 LSPH, with outer surface coatings. An equipment for thermal fatigue testing has been developed. Yet, tubular specimens with a diameter of 60 mm, a wall thickness of 3.5 mm and a heated length of 150 mm are used. The experimental setup is described in PSM 3.9.

First tests have been made with tubes of the reference material 1.4436 and outer surface coating. The calculated strain range in the coating was about 0.25 %. The cracks initiated at the inner side of the tube as in tests without coating. After the test no cracks were visible on the surface of the coating. The integrity was good. Four more specimens of this material were fabricated still without coating and will be delivered for coating.

Further tests are planned with the same kind of tubes as in PSM 3.9 made of AISI 316 LSPH. By choosing thicker tube walls higher strain amplitudes in the coating are expected. To buy tubes of this material and geometry different dealers were contacted. No tubes with SPH fabrication specification were found in sufficient quantities. Different 316 L tubes were investigated about their chemical composition. Measurements to obtain the parts of  $\delta$ -ferrit and nitrogen were performed. Specimens with chemical composition near to the SPH specification are now in fabrication to compare the fatigue behaviour with 316 LSPH. Parallel the fabrication of tubes from raw material was ordered.

#### Staff:

T. Fett  
W. Hartlieb  
J. Neumann  
B. Schinke

## PPM 1 Material Characterization and Neutron Irradiation Effects in Graphites, CFCs and Ceramic Composites

### Subtask 1.4

SiC qualities of industrial manufacturers are to be tested concerning the durability of tiles protecting the first wall against plasma instabilities and disruptions. KfK work has concentrated on determining the critical heat load under quasi-stationary conditions, including the consideration of property changes measured after neutron irradiation.

The laboratory experiment concerned was correlated with a former KfK proposal for wall protection. Small tiles are used with a front plate of 25 mm x 25 mm x 14 mm (thickness) and a tail specially shaped to be attached and cooled between two cooling tubes each. A 50 kW acetylene/oxygen burner was designed to uniformly heat the whole front face of a single tile which is laterally insulated. The heat flux density is varied with the distance from the burner plate.

Test results are presented in Fig.6, relating to about 10 samples per SiC type. The three SiC types tested were 1) S-SiC with 1.9 % boron content and 6 % porosity (F), 2) S-SiC with 0.4 % boron and 7.5 % porosity (H), 3) HIP-SiC (E). The edges of the HIP-SiC tiles had remained unrounded, also at the transition with large width reduction from the front plate to the tail. Therefore the data set "E" in Fig. 6 is directly comparable with "F" and "H".

Fig. 6 shows that 50 % failure probability for tile fragmentation was observed at about 2.0 MW/m<sup>2</sup>. The temperature gradient in the specimens was between about 1900 °C (front face) and 1000 °C. A Weibull plot was applied to Fig. 6 to allow an extrapolation to technically relevant, low failure probability. A heat flux density of about 0.9 MW/m<sup>2</sup> appears attainable at P = 10<sup>-3</sup>, which could be sufficient for a provisional proof of qualification with regard to normal operating conditions.

The constitution of the Si-C system was reinvestigated between 1400 and 3000 °C using an arc-melting furnace and a 400 kHz induction furnace with two pyrometric temperature measurement devices. The samples were characterized by high temperature DTA and by X-ray diffraction and X-ray microanalysis. One intermediate compound, SiC, occurs in the system. Peritectic melting of SiC was observed at 2830 °C according to the reaction  $\langle \text{SiC} \rangle = \{ \text{Si}_{0.87}\text{C}_{0.13} \} + \langle \text{C} \rangle$ . The melt boils incongruently under 1 bar pressure at about 3000 °C. The condensed vapour consists of Si and cubic  $\beta$ -SiC containing altogether 43 at.% C. SiC is monotropic. Only  $\beta$ -SiC with the higher chemical potential is formed from the gas phase and the melt according to Ostwald's rule. Thermodynamic measurements show that hexagonal  $\alpha$ -SiC is the stable modification.

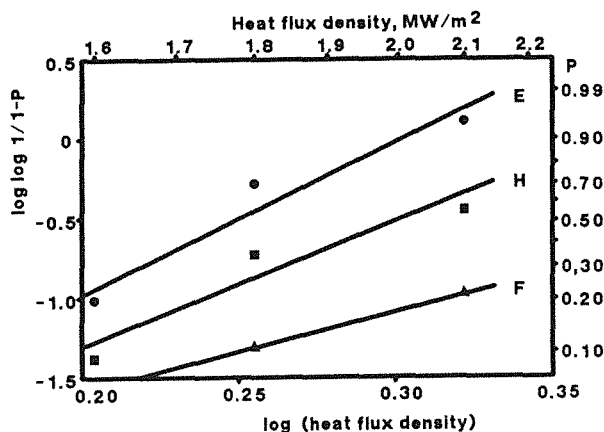


Fig. 6 : Failure probability P of SiC tiles dependent on the heat flux density at the front face

SiC samples from two neutron irradiation tests have been transported to KfK: CERAM-D217-1 (HFR-Petten, 1100 - 1200 °C, 1.2 - 1.6 x 10<sup>26</sup> n/m<sup>2</sup>) and PHENIX-MAT 6 (Phenix-Marcoule, about 500 °C, 30 dpa). Bending tests to determine UBS on about 100 specimens of HIP-SiC and CVD-SiC from CERAM-D217-1 are being started.

#### Staff:

M. Blumhofer  
 W. Dienst  
 G. Gausmann  
 H. Kleykamp  
 H. Zimmermann

## PPM 4 Material Characterization and Irradiation Effects in Ceramic Insulators

### Subtasks 4.1 and 4.2

Ceramic insulator materials (like  $Al_2O_3$ ,  $MgAl_2O_4$ ,  $AlN$ ) are to be selected with regard to their resistance to thermal crack formation by dielectric loss in RF-windows. These windows shall be applied to separate wave guides for ECR heating from the plasma vacuum. KfK work has concentrated on the extension of the data base for dielectric properties, especially at 145 GHz, including further improvement in the measuring accuracy, and on post-irradiation examination for several irradiation experiments.

PIE on samples from the LAMPF-Los Alamos irradiation (250 - 400 °C, 0.5 - 1 dpa) was continued. The thermal shock resistance of AL 23 (99.5 %  $Al_2O_3$ ) was examined in metal-melt immersion tests on 13 mm diam. pellets heated from room temperature. 50 % failure probability was found at  $\Delta T = 382$  K for unirradiated pellets and at  $\Delta T = 376$  K for irradiated pellets, which means that the thermal shock resistance was virtually unchanged. This fits the corresponding results that the ultimate bending strength appeared unchanged and that the thermal conductivity, which is of secondary importance in that thermal shock test, was only reduced by about 25 %.

The thermal conductivity of polycrystalline  $\alpha-Al_2O_3$  (AL23) under irradiation has been subject of a systematic study. The thermal conductivity of samples exposed to the radiation of four different irradiation sources is shown in Fig.7. The temperature dependence of the nonirradiated sample is included as a reference. The solid lines are least squares fits to the data according to a power law  $\lambda \sim T^{-k}$ . The experimental data of the nonirradiated sample can be fitted with  $\lambda \sim T^{-1}$  which is the usual behavior of nearly perfect insulating crystals at high temperature. The irradiation conditions were:

Fluence (part/cm <sup>2</sup> )	Irradiation Temp. (K)	Damage Dose (dpa)
KfK Cyclotron $1 \cdot 10^{17}$ (max. 100 MeV)	~ 700	< 0.1
LAMPF - SNS $5 \cdot 10^{20}$	~ 600	0.7
Petten - HFR $2.8 \cdot 10^{20}$ (> 0.1 MeV)	473	0.4
OSIRIS $2.1 \cdot 10^{21}$ (> 1 MeV)	823	5

The main features are:

1. The room temperature value of  $\lambda$  is reduced under irradiation.
  2. At temperatures above  $T \approx 1700$  K the  $\lambda$  value of the irradiated samples approaches that of the nonirradiated one.
  3. The temperature dependence of  $\lambda$  is changed, i.e. the value of  $x$  decreases.
- This is a consequence of 1. and 2.

The sample irradiated in the Petten-HFR shows nearly the same decrease in  $\lambda$  as the OSIRIS sample whereas their damage doses differ by a factor of about 10. Furthermore the reduction of thermal conductivity in the LAMPF specimen is less than that of the Petten sample. Accordingly, the irradiation temperature seems to have an important effect on the number of remaining stable irradiation defects.

Results of annealing experiments are shown in Fig. 8. The annealing temperature is held constant for 90 min. Then the sample is cooled down and measured at RT. Time dependent effects could not be observed in the annealing process. The differences in annealing behavior are mainly due to different damage doses, with exception of the sample irradiated in the Petten-HFR which reaches 100 % recovery at the lowest annealing temperature. This is an indication of a different microstructure of the irradiation-induced defects. Since the irradiation in the Petten-HFR was performed at the lowest temperature, it can be assumed that most of the defects produced are isolated point defects rather than defect clusters. The other three irradiation experiments were performed at higher temperature where a higher contribution of aggregated defects can be expected.

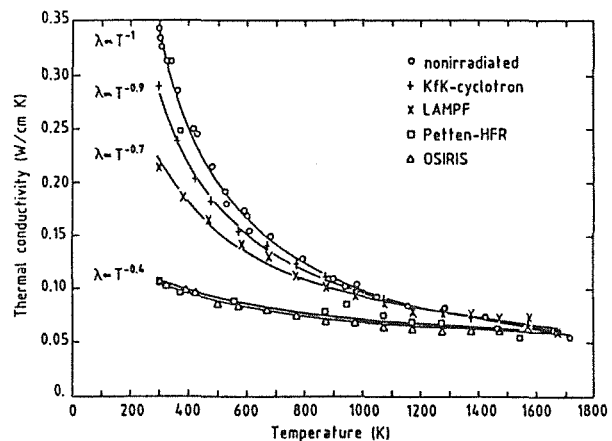
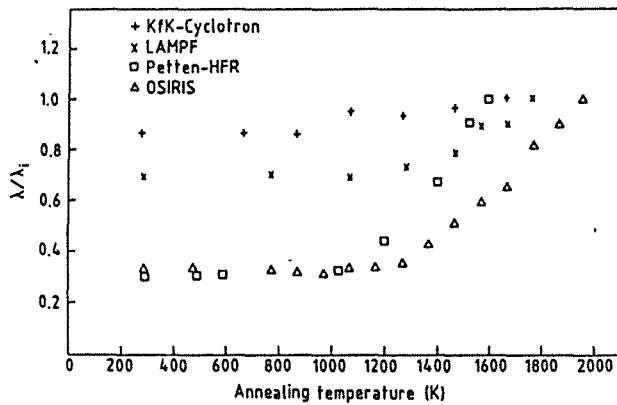


Fig. 7: Thermal conductivity data from four different irradiation tests and for a nonirradiated sample.



Staff:

- M. Blumhofer
- W. Dienst
- G. Gausmann
- R. Heidinger
- S. Hellgardt
- M. Rohde
- H. Zimmermann

Fig. 8: Normalized thermal conductivity of irradiated samples as a function of the annealing temperature.  $\lambda_i$  = intrinsic value of the nonirradiated sample.

The dielectric characterization of insulator materials with relevance to gyrotron windows was complemented by the study of ceramics which are not primarily designed as dielectrics, such as BN, quartz fiber substrates, commercial SiC, and alumina toughened with SiC whiskers. There were some promising features like a low loss level ( $\tan \delta \approx 5 \times 10^{-4}$  at 145 GHz) paired with  $\epsilon_r = 4$  in sintered BN and extremely low values of loss ( $\tan \delta < 10^{-4}$ ) as well as of permittivity ( $\epsilon_r = 2$ ) for low density fibre compacts. The dielectric parameters of the SiC based materials were not suited for a competition with the potential window materials, such as  $Al_2O_3$ ,  $MgAl_2O_4$  and AlN.

A first selection of samples now available from the LAMPF-SNS irradiation (see above) were investigated and compared as for the effects observed in the PETTEN-HFR irradiation (see above) with fission neutrons. In polycrystalline alumina and in single crystal (s.c.) alumina, the significant increase of  $\epsilon_r$  put to evidence after the PETTEN experiment could not be found after the LAMPF experiment. This observation goes along with a much smaller volume swelling and with only moderate changes in  $\tan \delta$  ( $3 (\pm 1) \times 10^{-4} \rightarrow 5 (\pm 1) \times 10^{-4}$  at 145 GHz). With the LAMPF experiment, first irradiated dielectric test specimens other than alumina are available at KfK: s.c.  $MgAl_2O_4$  and transparent AlN. Both experienced changes in permittivity:  $8.3 \rightarrow 8.4$  each.

Following the lines for a possible window operation at cryogenic temperatures, an extensive selection of materials (grades of  $Al_2O_3$ ,  $MgAl_2O_4$  and AlN) was prepared for neutron irradiations at temperatures close to ambience and to fluence levels of  $10^{18} - 10^{19} \text{ n/cm}^2$ . Two irradiations are running and will be completed by the end of the year.

## **PDT 1      Thermomechanical Tests of First Wall Mock-ups**

### Subtask 1.4

A program is performed at KfK for testing first wall (FW) sections in order to:

1. Provide an experimental basis to improve confidence in the prediction of thermal fatigue life by:

(a) Validation of computational methods for

- thermo-mechanical analysis
- crack initiation by cyclic plastic deformations
- fatigue crack propagation

in complicated geometries.

(b) Life time determination including

- observation during life
- study of failure modes for prototype FW sections under representative thermo-mechanical conditions.

2. Compare integral behaviour of different FW concepts including protection

The test specimens will be tested under mechanical boundary conditions and thermal loads as close as possible to those of NET.

The specimen will be positioned in a vacuum chamber; it will be actively cooled with water and will be heated by thermal radiation in a cyclic manner.

Pretesting of the radiative heater as a crucial part of the test apparatus is still being continued with good success. The usability of only 2 mm thick graphite laminate material manufactured into heating elements with short thermal response times has been confirmed. It seems that this will make an inexpensive heater of good thermal and mechanical properties and with reasonable life times at sufficiently high temperatures.

Since life time of the heater was found to be limited by local and strongly temperature-dependent graphite erosion which again resulted in an increasing nonuniformity of the heat flux, the test procedure was changed from pure thermal cycles with the heater being only a few seconds on the maximum temperature to test cycles with a temperature plateau and to steady state tests on a given high temperature level. The results very consistently confirm a very strong dependence of life time on temperature. A lifetime at full temperature of e.g. 70 hours is reduced to 30 hours if the temperature is increased by only 50 K from 2100 to 2150°C. Cycling itself has only a minor effect on life time. Heater lives of more than 5000 cycles with transient temperatures can be expected for maximum temperatures of at least 2150°C which seems sufficient for the experiments to be done.

The procurement of the test facility for the main tests is under way; the 4.5 m<sup>3</sup> vacuum vessel to house the test specimen has been designed, was called for tender, and will be ordered in October. The electrical power supply and some components of the cooling circuits are delivered.

Additionally, examinations on the testing techniques have been carried out. The cyclic thermomechanical behaviour of the test specimens will be controlled by thermocouples, clip gauges and strain gauges.

The magnitude of displacements and strains has been analyzed on the basis of FE-calculations considering different testing conditions and linear elastic and inelastic material models. Making use of the analytical investigation, the number and the location of measuring instruments has been determined.

For the temperature measurement in the test specimens a total of 56 thermocouples will be provided. A total number of 51 strain gauges and 16 displacement pick-ups will be used for the on-line measurements in the FW thermal fatigue experiments.

#### Staff:

E. Diegele

E. Eggert

G. Hofmann

H. Kreuzinger

B. Schinke

G. Schweinfurther



## PDT 2 Tests of Divertor Samples and Mock-ups

### Subtask 2.1

The main design issues for the NET divertor are the high heat flux, the physical and chemical erosion, and the surface damage from plasma disruptions. Current divertor concepts consist of a metallic heat sink structure protected by a heat and erosion resistant surface material. In this duplex structure the major thermomechanical concerns are material compatibility, perfect bonding, temperature limits, and cycling thermal stresses.

A testing program on the thermomechanical behavior of candidate divertor materials in a modified plasma spray facility (PSA) has recently begun with a first set of samples. Before discussing first results a brief description of the facility will be given, which was commissioned during this reporting period.

The major modifications to the commercial 120 kW plasma spray facility are the rotating sample holder at the vertical shaft with the pertaining drive mechanism (on top of the vacuum vessel), and the plasma gun swivel actuator at the horizontal vessel port (Figure 9). The water cooled sample holder carries six disc shaped samples and brings them one by one into the position facing the plasma flame, where they are heated for a predefined pulse length (Figure 10). After exposure of the six samples the gun swings downwards by about 20 degrees, while the sample holder rotates back to the first position. The next cycle starts after a selected dwell time, which is needed for sample cool-down. Typical parameters are given in Table 1. The motion is computer controlled as well as the vessel pressure and the electrical arc power to the plasma gun. Besides the process variables the sample surface temperature is monitored by a pyrometer during the heat pulse, and the rear side temperature at each sample is monitored continuously by thermocouples. All readings are stored on a personal computer, and the main parameters are on-line displayed on a monitor.

A first test with four different grades of fine grain graphite in the six positions was performed at the parameters listed in Table 1. The measured temperatures agree reasonably well with the finite element predictions to within about 10 to 20 percent giving confidence also to the calculated stress levels, which cannot be measured. Concerning the mechanical behavior it can be stated that all of the six samples survived the 1000 cycles without any visible cracks or distortions. A significant erosion crater can be observed, though, at the center of the heated surface, approximately 1 mm deep and 1 cm<sup>2</sup> in size. Metallurgical examinations are in progress.

A total of 15 such tests is foreseen with 42 different materials before entering similar tests with brazed samples.

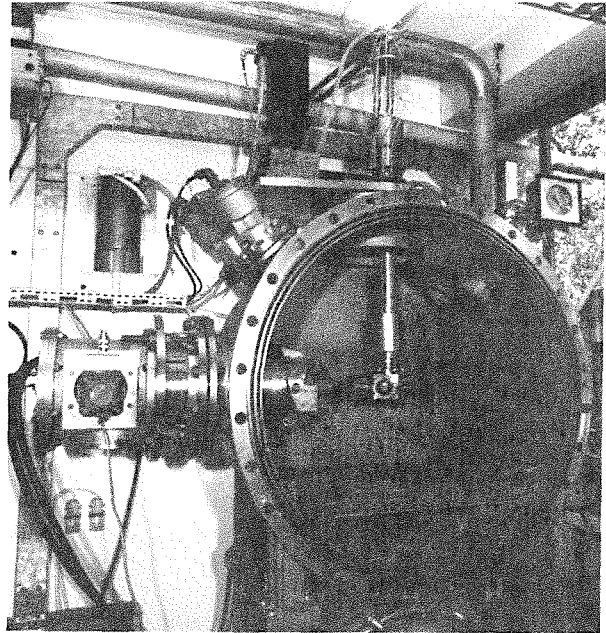


Fig. 9: Modified plasma spray facility (PSA) for thermomechanical sample tests

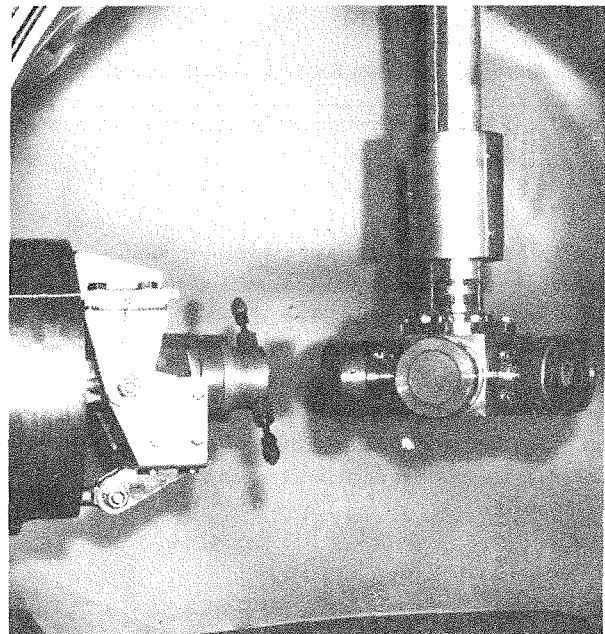


Fig. 10: Rotating sample holder carrying six samples and plasma gun

### Subtask 2.3

Definition of a 300 kW divertor test facility (DIVA) with an electron beam gun as a heat source was pursued and a formal proposal is under discussion with the NET-Team.

Meanwhile a series of pretests with a commercial electron beam gun has been performed at Leybold AG, Hanau, addressing key questions related to beam control, i.e., focusing and scanning frequency limits as well as the

Parameters for Graphite Samples	
Electric Power, kW	88
Calibrated peak heat flux, MW/m <sup>2</sup>	15
Heating time, s	2.2
Dwell time, s	30
Switching time between positions, s	< 0.2
Total number of cycles	1000
Temperature at begin of pulse, °C	100
Vacuum vessel pressure, mbar	80
Plasma flame feed gas	Ar + 7%N <sub>2</sub>
Finite element predictions: <sup>a)</sup>	
Max. Surface temperature, °C	1340-1470
Max. rear face temperature, °C	810-825
Max. compressive stress, MPA	-30 to -50
Max. tensile stress, MPa <sup>)</sup>	20
<sup>a)</sup> For fine grain graphites EK 986, V1325, V1383, V1393	

Table 1: Typical parameters for thermomechanical cycle tests in PSA

principal capability for plasma sweeping simulation. The pretests have demonstrated that such a gun can meet the requirements envisaged for DIVA, if several improvements to the present beam control system are implemented. This implies upgrading of the beam deflection system (including coils, current control hardware and software) to allow higher deflection frequencies at well defined amplitudes and path patterns. Also the diagnostics needs early attention.

Staff:

G. Class

K. Kleefeldt

K.H. Lang

K. Schramm

E. Wolf

## MTC 1 Industrial Manufacturing of a few km of React-and-Wind Nb<sub>3</sub>Sn Conductors and of TF Model Coils

### Subtask 1.1

For studying both the fabrication procedure and the physical properties of react-and-wind conductors a reduced size NET conductor at the scale of 1 : 1.75 with  $I_c < 10$  kA at 12 T has been industrially manufactured by Vacuumschmelze (VAC) and tested at KfK. This subscale conductor, shown in Fig. 11 without the steel conduit, can be divided into three major components: the core, the electrical stabilizer and the steel jacket.

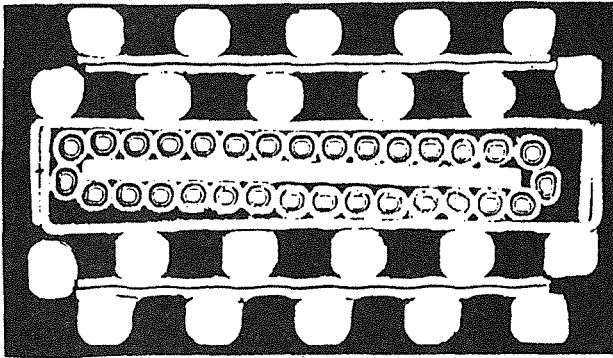


Fig. 11: NET/KfK subscale conductor, consisting of the rectangular core and the Cu stabilizers (the steel jacket is not shown)

The rectangular core of 14.3 x 3.0 mm<sup>2</sup> consists of a flat cable, soldered after the reaction heat treatment (64 h/700°C) into two U shaped 0.25 mm thick CuNi sheets. The cable consists of 31 multifilamentary Nb<sub>3</sub>Sn wires of 0.8 mm Ø with a transposition pitch of 120 mm, either with or without a 0.5 mm thick bronze foil. The electrical stabilizer has been separately fabricated by Roebel processing of 11 copper sections (1.5 mm<sup>2</sup> each) around a stainless steel strip of 2 x 0.2 mm and then soldered at both sides of the core.

For testing the current carrying characteristics of short sample NET subscale conductors a new test facility, FBI, has been built and was used in addition to the already existing smaller facility with loads up to 10 kN and 3 kA. The new FBI facility extends this range and has the following main parameters:

- Axial force,  $F \leq 100$  kN
- Magnetic field,  $B \leq 13.5$  T
- Sample current,  $I \leq 10$  kA.

The axial force is supplied by a hydraulic machine with  $F \leq 630$  kN, installed at the upper floor level, connected to the sample by the pull rod and the upper force grip. The hydraulic cylinder also allows a load cycling operation of the sample. For providing the sample current a 10kA/10V power supply is

used, connected with helium gas cooled current leads and the current grips of the sample. The gas cooled current leads are designed for pulse operation in order to reduce the LHe losses. The lower part of the 100 kN - 10 kA FBI test facility is shown in Fig. 12.

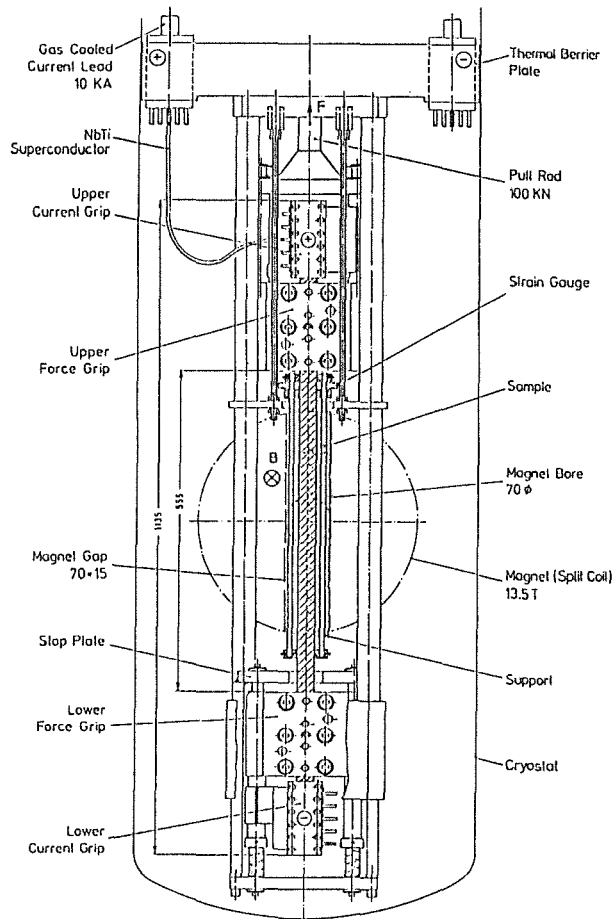


Fig. 12: Lower part of the 100 kN - 10 kA FBI test facility

One of the most important tests for fusion conductors is the behavior of  $I_c$  after several stress/strain cycles. Therefore the sample shown in Fig. 11 was cycled at 12 T and 4.2 K at different strain levels, shown in Fig. 13. The conductor was first statically strained from  $\epsilon_a = 0$  to 0.18 %, resulting in an increase of  $I_c/I_{cm}$  from 0.72 to 0.91. At this point the sample was cycled 73 times up to 0.46 % with a cycling rate of about 0.01 Hz without any degradation of  $I_c$ . Then the strain was enhanced to  $\epsilon_a = \epsilon_m = 0.32$  % and  $I_c/I_{cm} = 1$  and cycled 25 times between 0.32 and 0.70 % with the same cycling rate. After further straining to 0.50 % and a lower value of  $I_c/I_{cm} = 0.91$  the sample was finally cycled 25 times between 0.50 and 0.94 %. In all cases a complete reversibility of  $I_c$  was observed, irreversible behavior being expected at  $\epsilon_{irr} \geq 0.94$  % under the mentioned cycling parameters. This confirms earlier results on Nb<sub>3</sub>Sn wires, where cyclical straining up to 10<sup>3</sup> cycles within the statically reversible range showed no  $I_c$  degradation.

Thus,  $I_c$  for the NET/KfK subscale conductor behaves reversibly up to the measured static strain of  $\epsilon_a = 1.06$  %. This has also been observed for the other cable samples,

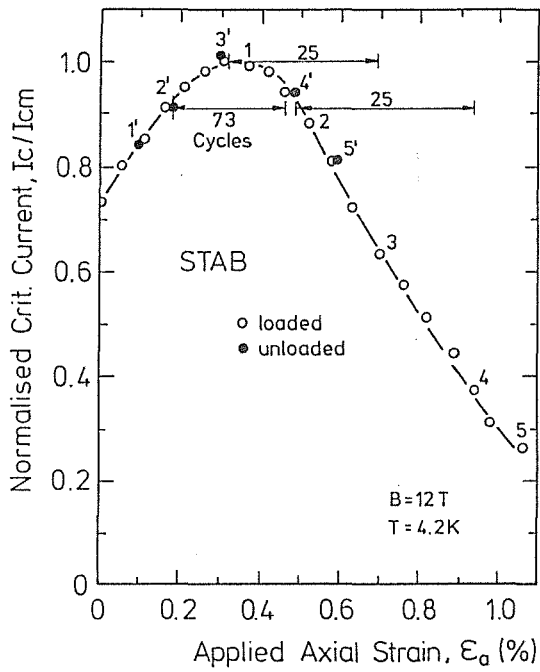


Fig. 13: Normalized critical current,  $I_c/I_{cm}$ , versus applied axial strain,  $\epsilon_a$ , at 12 T and 4.2 K after static and cyclical straining of the subsize conductor.

leading to an irreversible strain of  $\epsilon_{irr} \geq 1.06$  % under static conditions. Below this strain value no physical damage by filament cracking is expected.

Staff:

R. Flükiger

W. Goldacker

A. Kling (till 30.06.89)

M. Klemm

A. Nyilas

H. Orschulko

H. Raber

W. Specking

## MOC 1 Manufacturing and Testing of Short Length Full-Size NbTi Conductor (Outer Coil)

### Subtask 1.2

The aim of the task is the development, manufacturing and testing of NbTi conductors for the outer poloidal field coils of NET. The development steps are

- Development and testing of a subscale (15 kA) conductor in an overall verification test of a model coil (M 4.)
- Manufacturing and testing of a PF coil in TORE SUPRA using previous developments and design principles (MOC 2).
- Manufacturing and testing of a full size (40 kA) conductor for the outer PF coils of NET (MOC 1).

The first step is being performed at KfK. A superconducting poloidal model coil is under construction. The typical specifications for the operation of a poloidal field coil were taken from TORE SUPRA. The basic design principles of conductor and coil components are relevant for the TORE SUPRA and NET outer PF coils, respectively.

Both tasks MOC 1 and MOC 2 are joint efforts of KfK and CEA.

### Conductor fabrication

The manufacturing line for the laser beam welding was set up in May. 300 m U-shaped sections were successfully produced by Laser beam welding from two quarter sections. The start of the fabrication of complete conductor by enclosure of the round cable in two U-shaped sections by welding with two laser beams failed. The lenses for laser beam focussing were not suitable to keep welding parameters stable enough over the whole production length. In contrary to U-shaped section fabrication which was a through welding, the welding depth had to be kept in smaller tolerances. This was not possible with the existing focussing system. A mirror system for laser beam focussing was proposed by the manufacturer. Improvements in adjusting the laser beam line and quality control of the weld seam were proposed, too. The proposed improvements are being checked and realized now. A qualification test of the mirror focussing system and the stability of the laser were performed successfully by welding 150 m long helical weld seams on a tube. A micrographic investigation will be performed checking the constant welding depth.

An alternative manufacturing method of the Polo conductor by pulling the round cable in a premanufactured jacket looks promising after the first development steps. A complete fabrication line was set up. The manufacturing line produces the round cable including the wrapping with two stainless steel tapes by swaging. The ss-tapes replace the welded and swaged protection tube. 50 m dummy cable and 50 m jacket

were produced. The cable was successfully pulled into the jacket. Thereafter the jacket was compacted by drawing through a die, all procedures worked well. The preparation of the ss-tapes need more care and quality control. The analysed cable pieces showed damaged Kapton insulation not only between subcables and outer tube but also between subcables and inner tube. Sharp edges of the tapes wrapped around the subcables were the reason.

The stability experiment of a full size cable with CuNi wrapped subcables was evaluated [1]. The pulse field height  $B_m$ , which just induces a quench, was investigated as a function of the transport current  $I$ , the pulse length  $t_0$  and the cooling conditions. Fig. 14 shows measured  $B_m$  values as a function of transport current for  $t_0 = 10$  ms pulses, and supercritical cooling.

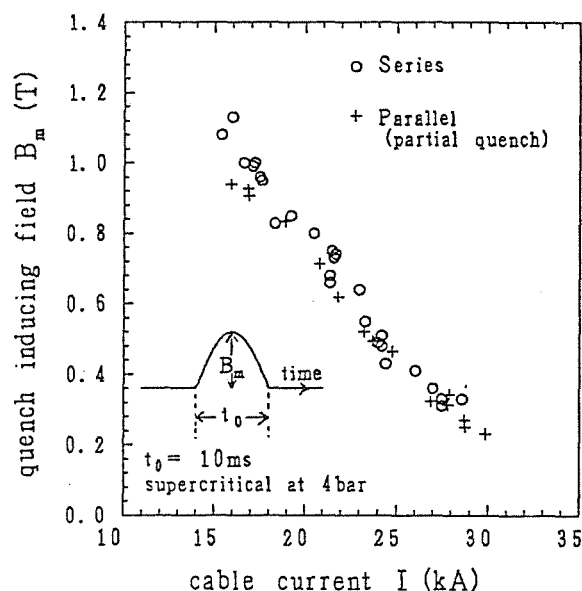


Fig. 14:  $B_m$  vs.  $I$  for parallel and series connection of the subcables

The parallel connection of the subcables has a slightly lower stability limit than the series one, the quench behaviour is however different. For the parallel connection, the quench is, for not too high currents, usually partial, i.e. not all of the subcables quench. For a complete quench of all subcables, the  $B_m$  values are about 10 - 15 % higher and almost similar for parallel and series connection. The recovery current  $I_R$  is about 15 kA, which is slightly lower as compared to the basic strand. This is mainly owing to the reduction of cooled surface. A suitable quantity for the discussion of the stability limit is not  $B_m$ , but input energy per cooled surface area calculated from  $B_m$ . The input energy is the sum of AC loss energy and the Joule heat energy of the quenching conductor.

The energy dissipation per cooled surface area,  $E/s$ , is plotted in Fig. 15. Joule losses are plotted separately. They represent only a small part of the total losses. The  $E/s$  curve of the basic strand (supercritical at 4 bar,  $t_0 = 10$  ms) is shown as solid line for comparison.

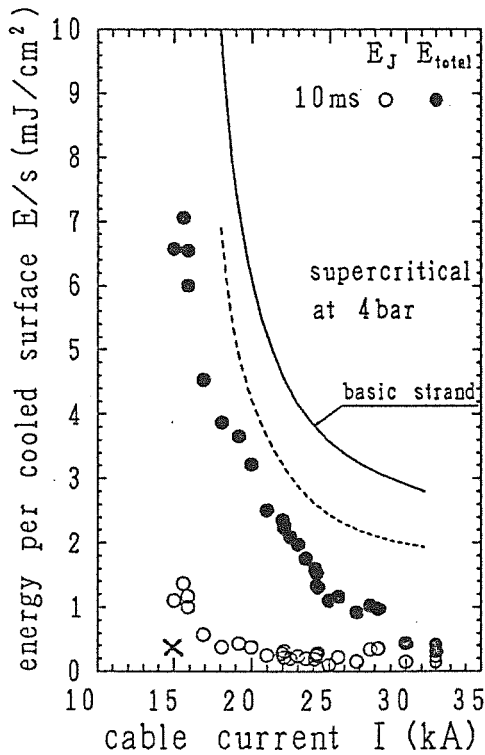


Fig. 15: Quench inducing energy dissipation per unit cooled surface area vs transport current. The cross left corner are the working point of Tore Supra.

The results of the stability experiments of the Polo conductor can be summarized as follows:

- There is almost no difference in the stability limit for liquid and supercritical cooling. This is a consequence of the small helium volume, in which the pressure rises rapidly above the critical pressure during a disturbance.
- In the high current range, the stability limit is much lower than expected from the strand experiment. This is understood qualitatively by an inhomogeneous distribution of the cable ac-losses, which follows from the scattering in the values of contact resistances between strands and subcables.
- From a practical point of view, however, the stability requirements on the cable are largely fulfilled. The cross in the lower left corner of Fig. 15 shows the working point of the cable in the TORE SUPRA poloidal field coil.

### Construction of the Model Coil

The detailed design of the model coil is finished. The prototype of the midpoint connection was completed and tested. The midpoint connection was exposed to 10 thermal cycles down to 77 K and 50 pressure cycles up 2.5 MPa. The measured leak rate was about  $1.4 \times 10^{-8}$  hpa l/s at 80 K and 2.5 MPa and was within the specifications. There will be no further helium tests. The midpoint will be dismantled for inspection. For excersising soldering of joints for the

midpoint connection type (three subcables have to be soldered) four samples were manufactured. The resistance was measured at 2000 A and were between  $18 \mu\Omega$  to  $42 \mu\Omega$  (specified  $\sim 20 \mu\Omega$ ). The joints will be analysed by cuts. A series of 27 axial breaks passed successfully leak, and pressure tests at 4.2 K and a high voltage test at room temperature. Only 1 piece had to be rejected.

One type of high voltage instrumentation cable was selected from the three prototype cables. The AC test voltage had to be reduced from 42 kV AC to 20 kV AC in order to meet better the real operation condition. An optical displacement transducer is being tested. The adhesion of the strain gauges on the coil surface and their accuracy under strain is checked.

### Insulation Testing

In the cryogenic high voltage laboratory a non destructive test method on the basis of the analysis of partial discharges (PD) was developed in order to determine delaminations caused by thermal or mechanical stress in superconducting magnets [2]. Partial discharges are microdischarges which develop in vacancies due to the field strength enhanced locally.

Following specified mechanical loading in a test machine the samples were investigated regarding their partial discharge characteristics. 50 test samples have been manufactured corresponding to the shape of the Polo model coil conductor (Fig. 16). The insulation consists of fiberglass reinforced epoxy resin with thickness of 1 mm between the conductors. The epoxy impregnation was made under vacuum for 25 samples and in air (wet impregnation) for the other 25 samples.

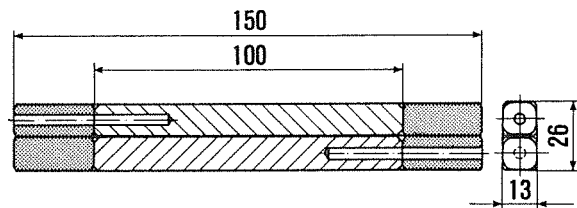


Fig. 16: Test sample for investigation of the insulation materials by partial discharge activity

The samples were mechanically loaded in the "short-beam testing mode" to ensure high stress at the epoxy bonded mid sectional area. A load of 5 kN causes a shear stress of 11 MPa, which is the operational shear stress of the conductor. The dynamic loading was performed with sinusoidal wave forms. The testing facility was a 25 kN servohydraulically driven mechanical tensile/compression machine (see M 9). The mechanical testing unit was placed in a helium flow cryostat. This system allowed test samples between 300 K - 5 K under dynamic mode ( $< 40$  kHz).

The PD measuring circuit is located in a Faraday cage in order to reduce external electromagnetic noise (Fig. 17). A

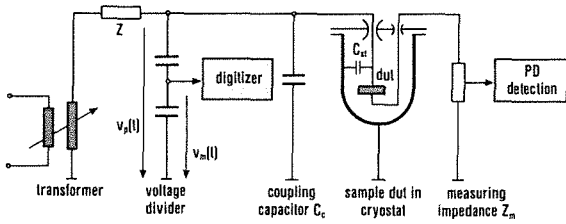


Fig. 17: Partial-discharge measuring circuit (DUT; Device Under Test).

high-precision gas insulated capacitive voltage divider is employed to measure the voltage up to 100 kV<sub>rms</sub>. The medium surrounding the test object may be air or an insulating liquid such as oil or liquid nitrogen. A cryostat permits working at low temperatures, down to 4 K. The measuring impedance  $Z_m$  is arranged in series with the test sample. The PD impulses decoupled from the test circuit with the measuring impedance  $Z_m$  are first processed by a wide-band PD-detector (Fig. 18). The amplitude of the PD response

energy distributions) are derived. When a measurement is terminated, the desired presentations are available on screen, from printer or plotter.

The summed charge distribution over 400 cycles for a wet impregnated sample are shown in Fig. 19. A linear relation was found for the summed charge and the stress level in the insulation material (Fig. 20). The dynamic loads have been varied from 5 kN (11 MPa shear stress) to 25 kN (55 MPa), each for 10.000 cycles.

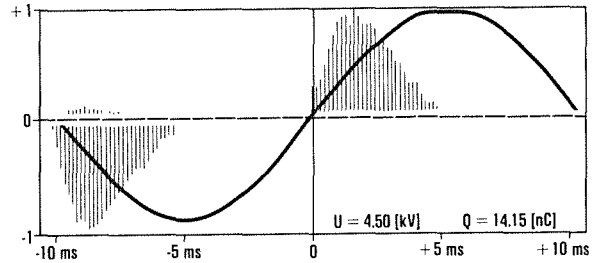


Fig. 19: Summed-Charge distribution of a wet impreg. sample (400 cycles,  $V_p = 4.5 \text{ kV} = \text{const.}$ )

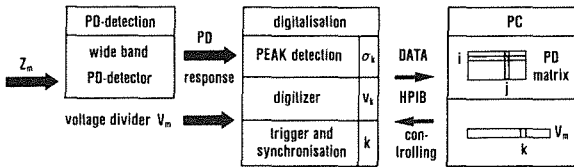


Fig. 18: Schematic diagram of measuring system.

is related to the apparent charge  $q_a$ . Therefore, peak detection from this signal is performed in the digitizing unit. The test voltage  $v_p$ , being kept constant during the test interval, is digitized once per measuring cycle. Further, it is used to synchronize the repetitive recording of full cycles. The trigger and synchronization unit enables in-phase acquisition of PD for the given number of cycles. The test voltage  $v_p$  and the apparent charge  $q_a$  can be established from the scanned values  $v_k$  and  $q_k$  using calibration factors  $F_v$  and  $F_q$ ,  $v_p = F_v \cdot v_k$  and  $q_a = F_q \cdot q_k$ .

Data transfer to the scanned values to the PC (computer) and controlling of the digitizer are effected via an IEEE 488 Bus (HPIB). After each complete recording of one cycle the scanned values are transferred to the PC for preprocessing. That is, the values  $q_k$  corresponding to the apparent charge are stored in the memory in matrix form (PD matrix). This is repetitively done until the desired number of voltage cycles is obtained. The values  $v_k$  corresponding to the test voltage are stored in vector form. The measured data are compressed in the PD-matrix (Fig. 18). The row corresponds to a certain apparent charge amplitude while the column corresponds to the phase angle. From the PD matrix the graphic presentations of results (apparent charge distributions,

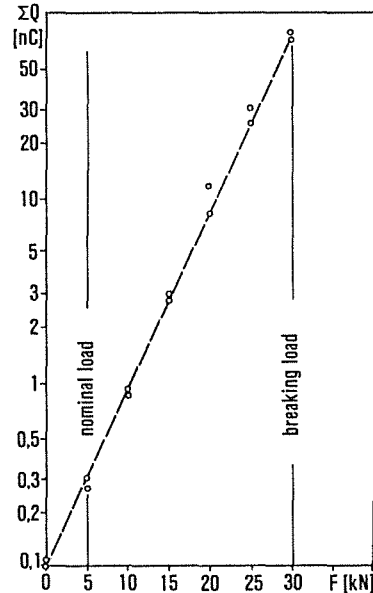


Fig. 20: Summed-Charge results (400 cycles, 50 Hz, 4 kV) as a function of sample shear loading.

The computer aided PD measurement, especially the Summed-Charge evaluation and analysis, is a powerful reproducible method allowing not only detection of delaminations but also detailed quantitative assessment of progressing degradation. The developed computer aided measuring system combined with the use of a "PD matrix" and suitable postprocessing (e.g. mapping of the PD matrix) allows a very precise evaluation of specific PD processes.

### Optimization of Current Leads

Current leads from room temperature to 4 K have to be carefully optimized with respect to reduction of cryogenic losses. The problem well known from bath cooled leads was extended to forced flow cooling conditions.

For the design of Polo current lead and further current leads a computer code named CURLEAD was written solving the one-dimensional heat equation and the energy balance for the helium coolant simultaneously [3]. The choice of variables sensitive to parameter changes has been investigated and shown by means of a low conductivity copper heat exchanger, (Fig. 21). Two current leads built in the past have been recalculated.

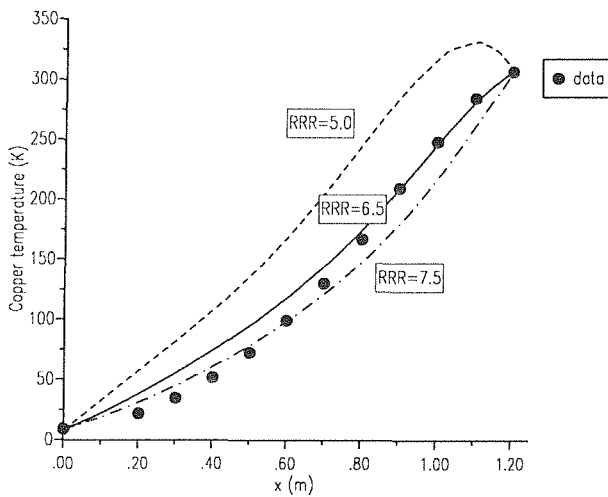


Fig. 21: Temperature distributions obtained for RRR = 5, 6.5, and 7.5 for the TORE SUPRA current lead. Differences between calculations and measurements can be explained by the uncertainty of thermal conductivity and electrical resistivity.

The transient behaviour of a low and a high conductivity heat exchanger have been studied and compared with respect to stability. The optimization study for a low conductivity current lead for the POLO model coil has been performed. Special attention was given to the forced flow mode and to the superconducting cold end appendix, too (Fig. 22). The importance of the knowledge of the thermal conductivity, and the electrical resistivity as well, as a function of temperature was mentioned because they are important for the optimization procedure. The main aim of writing CURLEAD is the optimization of a current lead by taking into account the real heat transfer. This means the calculation of the heat transfer coefficient assuming physical models which describe the hydrodynamic behaviour. One model is represented by the Dittus-Boelter equation (parallel-flow model), the other one uses empiric formulas for a flow perpendicular to a series of rods (cross-flow model). Using the temperature dependent heat transfer it has been shown that it is important to model the cold end region very carefully because the heat transfer

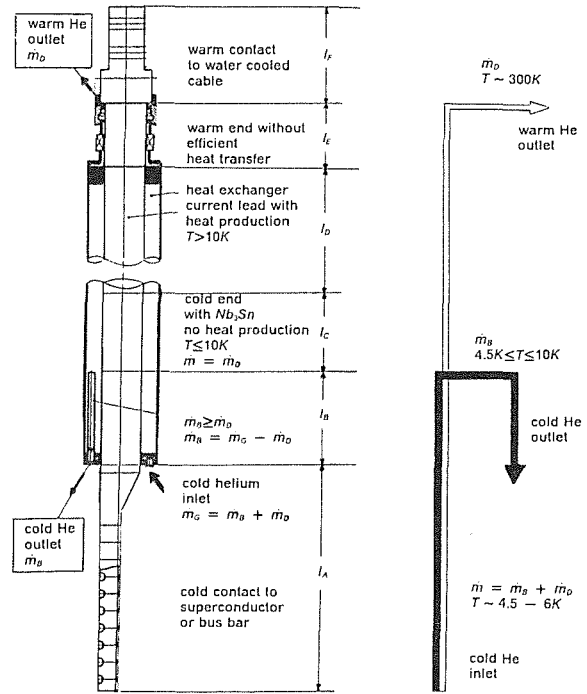


Fig. 22: Schematic view of the POLO current lead and its section (left) resp. mass flow scheme (right).

will be small in this region and the temperature difference between the copper lead and the helium coolant will be larger than in the warmer parts of the lead.

In general the use of a temperature dependent heat transfer also leads to a shorter length of the current lead because especially at lower temperatures the heat transfer is not as good as in the warm end region. In addition it is possible to obtain a heat loss at the cold end which depends on the cooling perimeter, i.e. the heat transfer properties of the heat exchanger. If an ideal heat transfer would be assumed the upper end will have a lower temperature which results in a longer length.

In addition the modelling of the warm end terminal, which in general will be poorly cooled, changes the temperature distribution of the heat exchanger significantly, e.g. as has been shown for the POLO current lead. The result of the addition of the warm end terminal is a shorter length of the heat exchanger.

As has been shown for the POLO current lead, the use of superconducting wires at the cold end parallel to the copper bar is essential to reduce the heat generation at low temperatures. In addition it is possible to get a "self-adjusting" heat exchanger with respect to different running conditions, Fig. 23. The helium mass flow rate will also be reduced. This means that the current lead will be optimized for a minimum and a maximum current,  $I_{min}$  resp.  $I_{max}$ . Smaller currents can be run by increasing the helium mass flow at the cold part of the heat exchanger by leaving its warm end optimized.



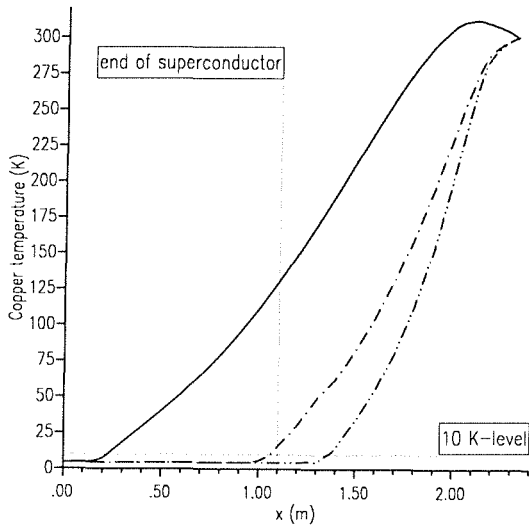


Fig. 23: Temperature distributions obtained by using the self adjusting for different currents (superconducting length) for the POLO current lead. Smaller currents can be run by increasing the mass flow at the cold end and leaving the warm end of the heat exchanger optimized.

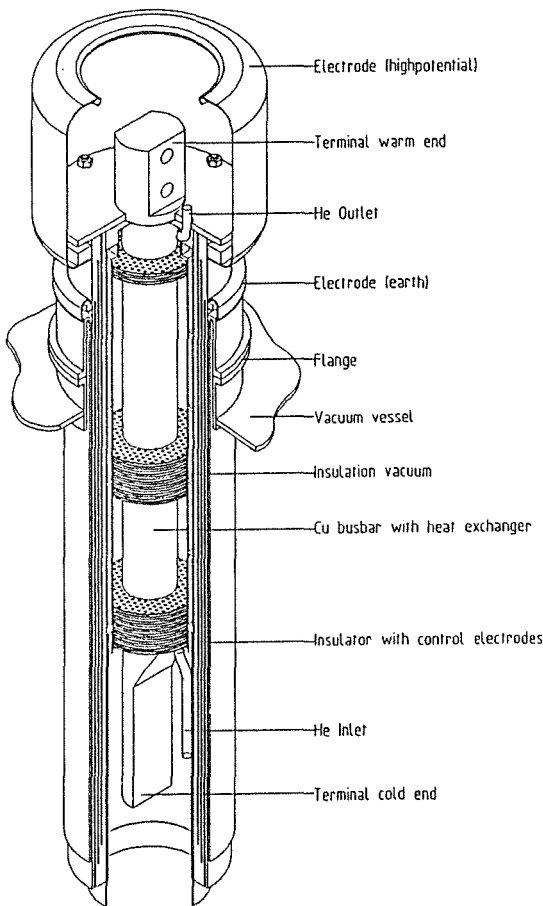


Fig. 24: 22 kA, 23 kV vapour cooled lead for the Polo-Model coil.

The detailed design of the optimized Polo current lead for 22 kA and 23 kV is now finished (Fig. 24). The main components

for three leads are being ordered. The manufacturing procedure is being discussed. The test for the lead is being discussed. A superconducting bus for shorting the both leads was ordered. The bus terminals will be the same design as the coil terminals.

Staff:

- H. Bayer
- I. Donner
- P. Duelli
- S. Förster
- P. Gruber
- T. Hardy
- W. Heep
- R. Heller
- U. Jeske
- D. Li
- G. Nöther
- A. Nyilas
- M. Oehmann
- U. Padligur
- K. Rietzschel
- L. Schappals
- G. Schenk
- C. Schmidt
- K. Schweikert
- E. Specht
- H.-J. Spiegel
- J. Seibert
- F. Süß
- M. Süßer
- A. Ulbricht
- A. Vogt (till June 30, 1989)
- D. Weigert
- F. Wüchner
- V. Zwecker

Publications:

- [1] H. Tateishi, C. Schmidt: Stability Experiment on the KfK Poloidal Field Coil Cable, Proc. MT-11, Tsukuba, Japan, Aug. 28 - Sept. 11, 1989.
- [2] G. Schenk et al: Partial-Discharge Measurements for Superconducting Magnets - a Non-Destructive Test Technique for the Compound-Insulation System. Proc. 5th Int. Symp. High Voltage Eng., New Orleans, Louisiana, Aug. 28 - Sept. 1, 1989.
- [3] R. Heller: Numerical Calculation of Current Leads for Fusion Magnets, KfK-4608, August 1989, KfK-Karlsruhe.

## **MOC 2      Design and Manufacture of One Outer Coil (in NbTi) and Installation in TORE-SUPRA**

### **Subtasks 2.1 and 2.2**

The aim of the task is the development and test of a superconducting poloidal field (PF) coil able to withstand the operating conditions of the outer PF-coils of TORE-SUPRA in order to validate the design principles for the outer NET-PF-coils. The TORE-SUPRA PF-coils will have the objectives to demonstrate the operations due to start up, control and disruptions as well as to confirm on a fairly large scale coil construction processes proposed for NET.

The activity is carried out by CEA. KfK contributes by its experience in the construction of the Polo-Model coil and component testing.

The main effort is concentrated to succeed in the industrial fabrication of the Polo-conductor as described in MOC 1. The applicability of one of the technologies for conductor manufacturing is a key question for TORE-SUPRA and NET conductors.

Two current leads designed for TORE-SUPRA by CEA, Grenoble, are being installed and prepared for test. The results of CEA current leads tested about 1.5 years ago were used for checking the computer code described in MOC 1.

#### **Staff:**

G. Friesinger

R. Heller

U. Jeske

C. Schmidt

K. Schweikert

A. Ulbricht

## MTF 2 Upgrade of the TOSKA-Facility for Model Coils Testing

### Subtask 2.1

The aim of the task is the upgrading of the TOSKA facility for the operation of the EU-LCT coil at 1.8 K up to about 10 T and the subsequent testing of NET TF/PF model coils.

TF model coils prepared in task MTC shall be operated in this facility as close as possible to NET conditions in order to prove the development of the entire industrial manufacturing process of the conductors and the test coils.

The upgrading of TOSKA will take place in the following steps

- The EURATOM-LCT coil shall be operated by forced flow superfluid helium at 1.8 K and tested up to the limits of the coil and/or conductor loading capability to prove the possibility of using this successfully tested conductor and coil design for NET-TF-coils as a back up solution. The step included a reinforcement of the coil case.
- For first NET model coil tests this coil is expected to give a sufficiently high background field to a neighbouring test coil (TWIN configuration, see Fig. 25).
- As soon as more model coils will be available a solenoid configuration shall be composed and tested.

The summary report about the possibilities of the TWIN configuration was distributed [1]. The low temperature subatmospheric pressure circuit for 1.8 K cooling of the LCT-EUR coil was ordered. Start of installation will be expected in November/December 89.

A first simplified finite element model (FEM) for the EURATOM LCT coil was created by means of the preprocessor PATRAN in order to assess symmetric and out of plane load cases for the design of the coil case reinforcement. The FEM code applied was ABAQUS. As a first test calculation the single coil load case was used. Material data for winding and case were taken from the FEM calculations by the NASTRAN code (Siemens, Interatom). The NASTRAN code is not implemented in KfK. Obtained stresses and displacements were compared with the earlier NASTRAN FEM calculations and measurements. The agreement was partially good. A more detailed FEM model is needed for further investigations. This model will be created by the conversion of the NASTRAN model into an ABAQUS model which can be run on the KfK computing system. The conversion will be performed by INTERATOM (Siemens AG). The finite element model will then be transferred to the KfK computer system.

A first design of the reinforcement of the LCT-coil for single coil operation is finished (Fig. 25). It will be the first starting

point for FEM calculations of the structure for reinforcements.

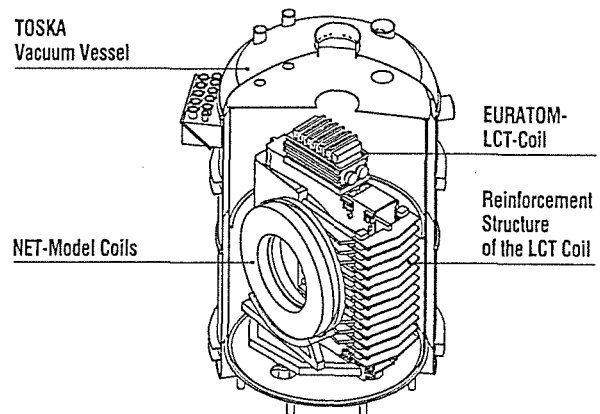


Fig. 25: TOSKA cryostat with reinforced LCT coil and NET conductor model coils

The specification for a 50 kA power supply was set up and a call for tender was sent out. For fast current changes a circuit similar to those of the Polo model coil (MOC 1) was discussed.

#### Publication:

- [1] A. Grünhagen et al., NET Model Coil Test Possibilities in the TOSKA TWIN Configuration, Report KfK 4602, July 1989, KfK-Karlsruhe

#### Staff:

A. Grünhagen  
R. Heller  
W. Herz  
K. Jentzsch  
H. Kapulla  
B. Kneifel  
W. Maurer  
L. Siewerd  
A. Ulbricht  
A. Vogt (till June 30, 1989)  
G. Zahn

### Subtask 2.2

The aim of the task MTF 2/2 is to develop the basic understanding and the technology for operating large superconducting coils with a forced flow of helium II. KfK activities are concentrated on a) the development of He II coolant loops operated with thermomechanical pumps and b) on investigation of stability and transient behavior of coils operated with internal flow of He II.

**Test loop operation**

A small size test loop with a self-sustained thermomechanical pump (Fountain Effect Pump) has been operated at steady and unsteady heat loads [1]. The scheme is shown in Fig. 26 and the dimensions of the components are given in Table 2. For sufficiently high steady heat load, applied to the heater HTSM in the middle of the test section simulating the coolant channel of a superconducting coil, the operational characteristics such as flow rate and temperatures at different positions are well understood. It is adequately described by our computer code HE2PPFF.

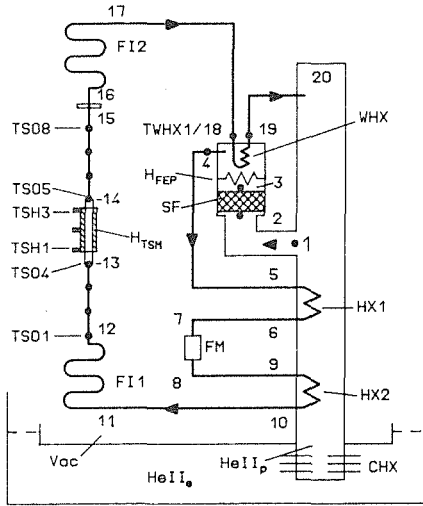


Fig. 26: Scheme of the test loop

Pos.	L (m)	Def (mm)	$\Delta p$ (%)
1-2			0.
2-3	SF	0.1	35
3-4	WHX	0.1	35
4-5	VT1	1.46	3.28
5-6	HX1	1.0	3.28
6-7	FM	0.3	4.0
7-8		0.44	3.28
8-9	HX2	1.00	3.28
9-10		0.43	3.28
10-11	FI1	3.45	1.88
11-12	TS1	0.5	3.0
12-13	TSH	0.13	4.00
13-14	TS2	0.40	3.00
14-15	HTC	0.005	4.00
15-16	FI2	3.75	1.88
16-17		0.6	3.28
17-18	WHX	1.4	3.28
18-19	VT2	0.71	3.28
19-20			

Table 2: Components of the loop

At small heat loads, however, there are operational ranges where the flow becomes instable such that it oscillates with high amplitudes. It could be verified that such oscillations can be prevented by simple means, namely by applying a small amount of power to the heater  $H_{FEP}$  which is

incorporated in the pump. The limits between stable and oscillatory operation are mapped by Fig. 27. The curve most relevant for superconducting coils is given by line 4. It is shown that in a loop which is capable to evacuate a heat load of up to 8 W from a coil, a power of less than 0.2 W must be supplied directly to the pump to prevent the occurrence of oscillations. In our reference design for NET [2] it is foreseen to provide this "stabilizing load" by parasitic losses resulting from current leads and from the helium supply.

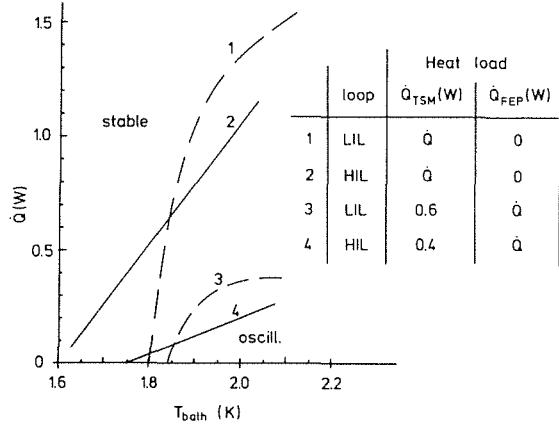


Fig. 27: Ranges of stable and oscillatory operation of the loop for heat at different positions of the loop (HTSM and HFEP, resp.)

**He II flow through narrow pore filters [3]**

Another series of experiments was done to find the most appropriate material for the filter of the thermomechanical pump. First we still disregarded mechanical stability and we draw the attention to the pore sizes of filter plugs. For this purpose we have made filter plugs from stacks of well defined membranes which are commercially available for chemistry and biology applications. Three types of filters with quoted filtration grades of 200, 50 and 10 nm have been used (Sartorius (R) cellulose nitrate membrane filters, type SM 11317/28/18). The flow rate versus heater power measurements have been analysed and it was found that there is no friction as long as the velocity of the superfluid component is smaller than a critical value  $V_s(c)$  which depends on the warm end temperature of the plug and on the pore size. This quantity namely the critical superfluid flow velocity related to the total cross section area of the plug (which is different from that within the pores) is shown by Fig. 28. The smaller pore material provide higher flow rates but the more pronounced temperature dependance is disadvantageous for operation close to the  $\lambda$ -line temperature.

**Modified loop for conductor tests**

Future investigations on operation of small coils operated with forced flow of He II require a largely modified apparatus. The main design parameters are:

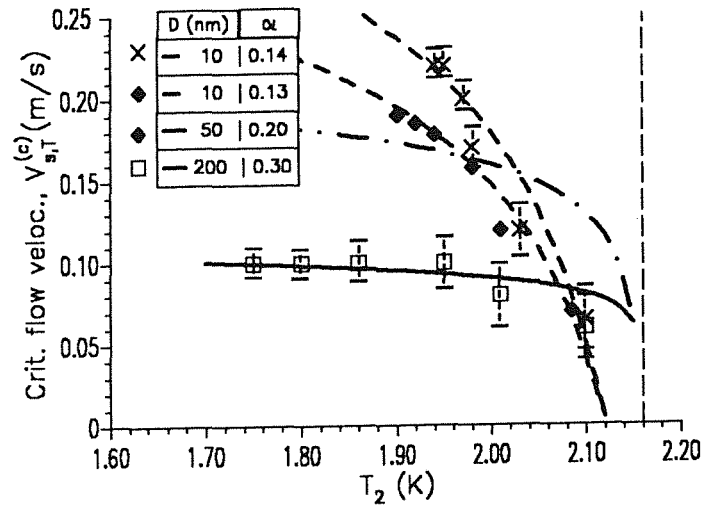


Fig. 28: Measured and calculated critical flow velocities as function of outlet temperatures for materials with different filtration grades D ( $\alpha$  is a fit parameter as described in the text).

- Continuous operation at 1.8 K with 5 W heat load and about 5 g/s flow rate
- 2000 A current feed through
- Volume for conductor tests ca. 220 mm  $\varnothing$ , 200 mm long
- Possibility of operation in 10 T background field of the HOMER test apparatus.

The fabrication of the components is going on.

Publication:

- [1] A. Hofmann and S. Kasthuriengan: 'Fountain effect pump driven helium flow at steady and unsteady heat load', presented at the CEC/ICMC 89 Conference, Los Angeles, USA, July 1989 (Primärbericht 03.03.07P07A).
- [2] A. Hofmann and A. Khalil, Considerations on magnet design based on forced flow of He II in internally cooled cables, in "Fusion Technology 1986", Vol. 2, published for CEC by Pergamon Press Oxford, p. 1811.
- [3] A. Hofmann: 'Critical velocity of superfluid helium flow in fine narrow pore filters', presented at the 1989 Space Cryogenics Workshop, Pasadena, USA Aug. 1989 (to be presented in Cryogenics).

Staff:

A. Hofmann  
 M. Kempf  
 K. Wagner  
 B. Vogetley

## MSA 1 Safety Relevant Models and Experiments for NET Magnets

### Subtask 1.2

During operation of superconducting magnet systems disturbances are conceivable which could finally result in the destruction of a magnet. The energy discharged thereby into an electric arc may lead to damage of the surroundings of the magnet. Cause and course of the disturbances, their detection and identification as well as their possibly destructive consequences are to be investigated using the superconducting torus arrangement TESPE-S. Through development of codes and their verification on the TESPE-S experiment an attempt will be made to transform the results to larger magnet systems.

The experimental investigations of arcs supplied by the magnet's energy and burning under spatial restrictions like in magnet windings could be finished, except for a series with the arcing chamber exposed to a relevant external magnetic field. Earlier experiments with a small field of only 0.1 T had shown the significant influence of magnetic field on the arc's behaviour, therefore a superconducting magnet supplying about 4 T in a warm bore of 40 cm has been installed. The magnet was taken successfully to its design values. The corresponding arcing experiments will be performed in October.

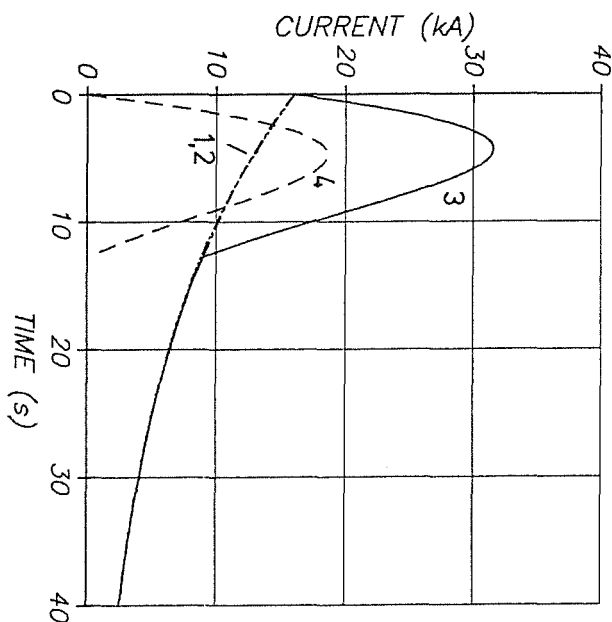


Fig. 29: MSCAP results for the current distribution in the NET TF coil circuit with a short across one pancake at start of discharge turning to an arc above 1 kA (1 - faulty coil, 2 - second circuit, 3 - arcing pancake, 4 - short and arc).

The continued evaluation of the performed experiments and analyses with the code MSCAP of INEL showed good agreement of calculation and experiment when the input characteristics of the arcs were taken from experiment, i.e. the program was validated and could be applied to NET with the arc characteristics transferred from the TESPE-S experiments. Two examples of calculations are shown in the Fig. 29 and 30. In Fig. 29 an electrical short of  $1\text{ m}\Omega$  is assumed to bridge one pancake of a NET TF coil at the beginning of a system discharge and to melt when 1 kA is reached in the short forming an arc with a burning voltage of 100 V. For a quench resistance of  $4\text{ m}\Omega$  the electromagnetic coupling takes the current through the shorted/arcing pancake to double the operating current. The arc's energy, i.e. the destructive potential, is here 13.6 MJ or in terms of damage that could lead to melting of roughly 20 kg of copper in case of localised heating. In Fig. 30 the case is calculated when one complete coil in circuit 1 of the two TF coil circuits is short-circuited with  $1\text{ m}\Omega$  at start of discharge assuming that this short can carry the full current. The current in the shorted coil by chance increases again to double the operating current although the total coil quenches already at 24 kA. That current distribution leads to highly asymmetric forces with heavy loading of coil and inter-coil structure

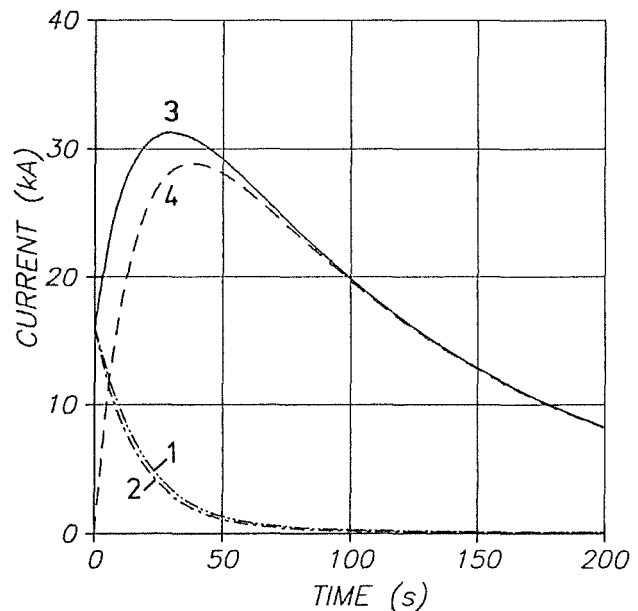


Fig. 30: MSCAP results for the current distribution in the NET TF coil circuit with a massive short across one coil during system discharge (1 - faulty circuit, 2 - second circuit, 3 - shorted coil, 4 - short resistor).

The evaluation and transfer to NET conditions is being continued for a short period. This work which belongs to the former task S+E 4.1.3 is then coming to its end. Activities for MSA 1.2 were started. In collaboration with ENEA and the NET Team the available test facilities were reviewed finding SAFFO at ENEA and possibly STAR at KfK. In SAFFO a first preliminary test with an available NbTi conductor will be performed. Based on earlier experimental evidence and first results of theoretical work at KfK and NET Team the definition of experiments (milestone 1, Dec. 89) takes shape.

Publication:

K.P. Jüngst and H. Kronhardt, 'Electric Arcs, Behavior and Influence on Safety of Superconducting Fusion Magnets', IAEA Technical Meeting on Fusion Reactor Safety, Jackson, Apr. 4-7, 1989

Staff:

P. Duelli

K.P. Jüngst

H. Kiesel

H. Kronhardt

G. Obermaier

M. Oehmann

J. Seibert

E. Süß

## TPV 1 Development of Solid Particle Separators for Plasma Exhaust

### Subtask 1.1

Solid particles generated during plasma/wall interaction can be transported into the plasma exhaust pumping system where they can influence the operation of the vacuum components (valves, pumps). The objectives of the task are to investigate the transport of solid particles during normal operation and during accidents and to develop solid particle separators for installation in front of the plasma exhaust pumping system.

To investigate particle transport in steady-state gas flow such as in the burn or dwell modes, and to measure the ratio of resuspension and the transport properties under non-steady-state conditions, such as sudden venting or rupture of a coolant pipe, experiments will be performed in a 1:15 scale model of a NET I resembling configuration with particulates of original size. This model equipment called SPARTA (Solid Particles Transport) is shown in Fig. 31.

Its design is based on similarity laws governing the similarity of flow [1] and the similarity of particle transport [2].

#### Similarity of flow

The Knudsen number is characteristic of the transition from continuum flow to free molecular flow and it is proportional to

the quotient of the Mach number (M) and the Reynolds number (Re) [1].

The M/Re similarity ensures for sub-problems a similarity of complicated flow events. The flow of rarefied gases with the same ratio of specific heats across pipes with the same ratio of diameter to length in the absence of heat transport can be treated using similarity variables, which is implicit in the calculation of the coefficient of resistance of the pipe according to Ackeret [2] and in the calculation of conductance according to Santeller [3], respectively. The similarity of flows passing a pipe is satisfied by identical values of the Reynolds number and of the Knudsen number.

#### Similarity of particle transport

To satisfy similarity between the model and the industrial-scale variant, the following requirements must be made on dust-air mixtures [2]:

- The geometric similarity shall be satisfied.
- The flows shall be similar.
- The material loading shall be the same and the ensemble of particulates shall be maintained.
- The dynamic similarity (1) shall be satisfied.

$$\left(\frac{v_g^2}{g \cdot D}\right)_M = \left(\frac{v_g^2}{g \cdot D}\right)_G \quad (1)$$

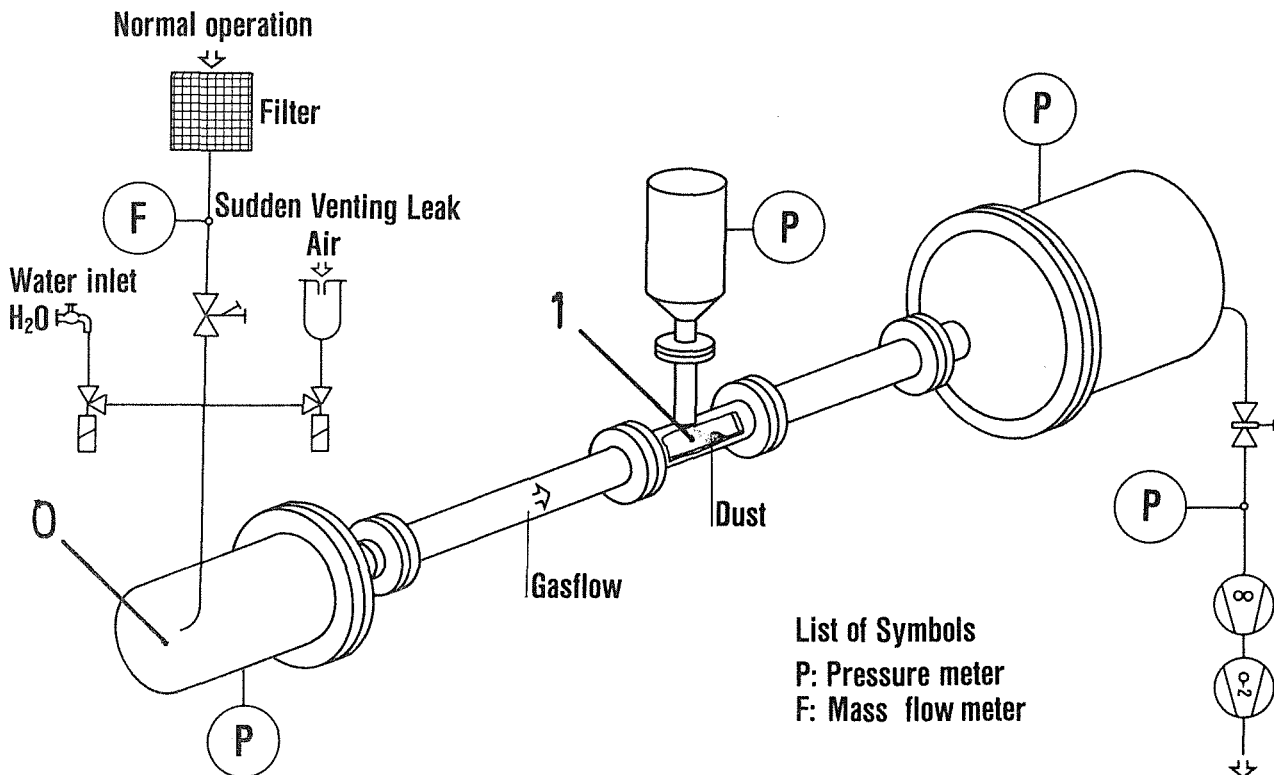


Fig.31 : Engineering Flowsheet of SPARTA



where  $v_g$  = terminal settling velocity  
 $g$  = local acceleration  
 $D$  = characteristic dimension  
subscript M = model  
subscript G = industrial-scale version

Staff:

W. Höhn  
B. Kammerer  
M. Lieberknecht  
D. Perinic

References

The dynamic similarity depends on the law of resistance applicable to the particulate and its terminal settling velocity, respectively. The resistance of particulates in the rarefied gas can be described by the slip correction of the Stokes law of resistance and by the Epstein formula [4].

The design and construction of SPARTA are almost completed so that it is possible to describe the facility in more detail.

Description of the SPARTA experimental facility

In steady-state experiments a rarefied gas flow expanded by a Pneurop dome enters the equipment at point O, passes the pipe and is exhausted in a steady-state mode. At point 1 particulates are dosed in which deposit on a probe covering the bottom of the pipe. The dusts dosed in with a brush dosage system are commercially available dusts such as ultra-fine graphite dust of the familiar spectrum of grain sizes. At the end of the experiment the probe is withdrawn and examined under the microscope.

It is examined whether the spectrum of grain sizes has been maintained during dosing in or whether it has been influenced by agglomeration. Besides, the macroscopic transport path from the dosage system to the point of deposition on the probe is evaluated as a function of the grain size.

In non-steady state experiments a mass flow of air and water vapour, respectively, is supplied at point O which causes the pressure to rise. The set of pumps is inoperative during that process.

At point 1 and the point of deposition determined in the steady-state experiments, respectively, a defined amount of dust covering the familiar spectrum of grain sizes has spread. The amount of dust resuspended by the flow is determined by weighing at the end of the experiment. It is extremely difficult to measure the dust transport under the transient test conditions (pressure, type of flow, concentration, velocity). Therefore, an indirect conclusion is drawn with respect to dust transport on the basis of balancing the dust raised and the dust deposited along the transport path. For this purpose, the probe covering the bottom of the pipe is withdrawn at the end of the experiment and the surface-specific distribution of the number of particulates deposited over the probe length is counted under the microscope.

- [1] J. Zierep: Similarity Laws and Modelling  
Marcel Dekker, Inc. New York, 1981
- [2] P. Grassmann: Physikalische Grundlagen der  
Verfahrenstechnik  
Verlag Sauerländer Aarau und Frankfurt a.M.,  
1970
- [3] Santeler et.al.: Vacuum Technology and Space  
Simulation  
NASA, 1966
- [4] S.K. Friedlander: Smoke, Dust and Haze  
J. Wiley and Son, 1977

## TPV 2 Optimization of the Cryogenic Vacuum Pumping of Helium

### Subtask 2.1

The objective of this task is the development and optimization of cryogenic vacuum pumping of plasma exhaust including helium. To develop cryosorption panels a variety of eligible material combinations for helium cryosorption will be tested on a reduced scale. The best suited technical solutions will be optimized on a technical scale under simulated NET operation conditions. The result of the investigations will be design data and requirements with respect to the operation of the compound cryopumps to be used in the plasma exhaust pumping system of a fusion machine.

### TARZAN - testing facility

In the TARZAN testing facility all manufactured specimens not exhibiting any flaws or loss in sorbent material are subjected to thermal cycling. The general layout of the facility is visible from Fig. 32. It comprises mainly the functional components of specimen holder, specimen holder-transport system, electrically heated furnace, and dewar for liquid nitrogen.

Up to 100 times the specimens are alternately immersed into liquid nitrogen and heated up to the respective reactivation temperatures  $T_R = 150\text{ }^\circ\text{C}$  and  $300\text{ }^\circ\text{C}$ , respectively, in a furnace. Specimens which after thermal cycling exhibit mechanical changes such as cracks, bubbles, foaming or detachment of the sorbent/binder layer are not eligible for the subsequent examinations.

The cycling tests with liquid nitrogen cannot cover the entire temperature range down to 4,2 K. But the very steep temperature range obtained during quenching of hot samples in the LN bath guarantees thermal stresses to occur in the bonding at least by one order of magnitude higher than during the normal pump operation cycles.

### Results of the cycling tests

Table 3 shows the specimens cycled up to now and the fields of the matrix which have still to be evaluated.

#### Brazing alloy specimens:

The brazing alloys CH1 (0,2 mm foil) and CH1 AP (soldering powder) wetted well the activated carbon particles and likewise withstood well thermal cycling. Failures occurred only during brazing with ceramic round plates which became detached due to the differences in thermal expansion behaviour in copper and stainless steel, respectively, during cycling. 32 specimens were subjected to cycling; 28 passed the test successfully.

#### Sintered metal fibre fleece specimens:

None of the two specimens passed the test successfully.

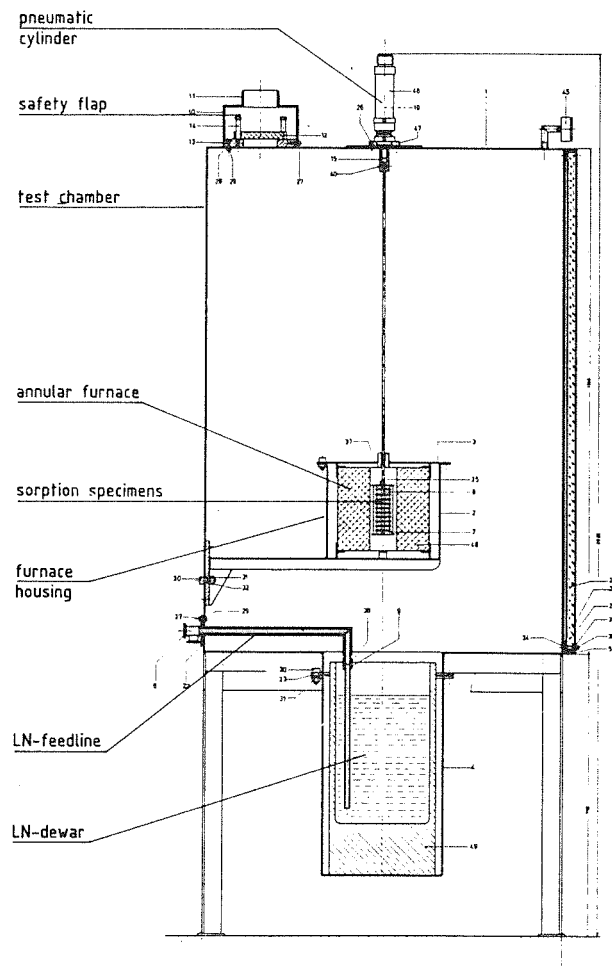


Fig. 32: TARZAN testing facility for thermal cycling of sorption specimens

#### Plasma sprayed specimens:

55 plasma sprayed specimens have been subjected to cycling so far. They had been prepared both by homogeneous deposit spraying with different thicknesses of the sprayed layers (0.1 - 2.5 mm) and by adhesive spraying of adsorber particles. 47 specimens passed successfully the thermal cycling test. On two specimens flaws in the sprayed layer were observed. As  $\text{Al}_2\text{O}_3$  powder with Cu powder added had been sprayed onto copper plates giving coatings of 1.38 mm and 1.26 mm thicknesses, it can be assumed that also in that case the difference in thermal dilation behaviour of the materials used was decisive for failure.

#### Cemented specimens:

162 specimens were subjected to thermal cyclic loading. 126 specimens passed the test successfully. A distinction has been made between thin cement coating applied with and without the addition of a heat conducting agent, and thick cement coating applied with and without the addition of a heat conducting agent. It became evident, that the thickness of the cement coating applied is of major importance. 38.2 % of specimens with a thin layer of cement

applied fail after cycling, but only 10.6 % of specimens with a thick cement coating applied. 50 wt% Cu powder has no negative influence on the stability of cementings.

Considering both specimen fabrication and cycling, Cerastil C3 (11.1 % failed) and Thermoguß 2000 (13.0 % failed) proved to be the best bonding material.

**TITAN testing facility**

Within the framework of acceptance testing all cryo-vessels were leak tested in the factory by application of 1.3 bar overpressure externally and 4 bar overpressure internally. The facility was cold operated with LN. The rates of evaporation and homogeneity in temperature determined in this process were accepted. The facility was cleared for shipping to KfK and is at present prepared for final acceptance with LHe.

**Staff:**

- H. Haas
- J. Hanauer
- W. Höhn
- B. Kammerer
- U. Kirchhof
- H. Lukitsch
- A. Mack
- D. Perinic
- D. Zimmerlin

Survey of material combinations for sorption specimens			Number of specimens subjected of cycling tests																		
			Cement				Brazing alloy				Solder				Plasma		Sinter		Pack		
			Cerastil C3	Cerastil C10	Ceramics 530	Thermoguß 2000	CH1 Mg/Cu/Al/Ti	CH1 Ni/Al/Cu/Al/Ti powder	CH1 Ni/Al/Cu/Al/Ti	CH1 Ni/Al/Cu/Al/Ti	CH1 Ni/Al/Cu/Al/Ti	CH1 Ni/Al/Cu/Al/Ti	CH1 Ni/Al/Cu/Al/Ti	CH1 Ni/Al/Cu/Al/Ti	CH1 Ni/Al/Cu/Al/Ti	CH1 Ni/Al/Cu/Al/Ti	CH1 Ni/Al/Cu/Al/Ti	CH1 Ni/Al/Cu/Al/Ti	CH1 Ni/Al/Cu/Al/Ti	CH1 Ni/Al/Cu/Al/Ti	CH1 Ni/Al/Cu/Al/Ti
<b>Activated carbon</b>																					
Degusorb F12/47D	cylinder, 1.0 mm dia.	Degussa	3	3	3	2	5	2	1												
Degusorb AS16/45D	cylinder, 1.5 mm dia.	Degussa	3	3	3	3	6	2	4	1											
Degusorb F30/47D	cylinder, 3.0 mm dia.	Degussa	4	3	4	3	6	3	3	1											
Degusorb C25	particles < 2.0 mm	Degussa	4	3	3	5	7	3													
Picacilf TA spec. 6=3.5	particles 2 - 10 mm	Pica	3	3	4	4	5	5	2												
Carbopal P1	powder, < 80 µm	Lurgi																	5	4	
Carbon (C)	tissue 0.5 mm thick	Goodfellow																			
<b>Molecular sieve</b>																					
S I, S705	pearl, 2.0 mm dia.	Merck	5	5	4	4	8													3	
S I	cylinder, 1.6 mm dia.	Union Carbide	4	4	2	2	9														
S I	cylinder, 3.2 mm dia.	Union Carbide	4	3	3	2	8														
S I	powder < 50 µm	Union Carbide																	5		
<b>Ceramics</b>																					
Friall Degussil AL25	ceramic fragments	Friedrichsfeld								3											
Friall Degussil MG25	ceramic fragments	Friedrichsfeld								2											
Friall Degussil ZR25	ceramic fragments	Friedrichsfeld																			
Al <sub>2</sub> O <sub>3</sub> PEM 105 SFP	powder	Metco																		7	
<b>Porous metal</b>																					
Sikan - Ni	disk 50 dia = 2 mm	Krebssope																			
Cu-55	powder, 44 - 88 µm	Metco																		9	
Ni-56F - NS	powder, < 88 µm	Metco																		10	
<b>Metal fibre fleece</b>																					
2700 g/cm <sup>2</sup>	1.4404, 2 µm fleece	Bekaert																			1
5400 g/cm <sup>2</sup>	1.4404, 2 µm fleece	Bekaert																			

Table 3: Thermally cycled sorption specimens

## TEP 2 Plasma Exhaust Processing Alternative Options

### Subtask 2.1

Endurance tests of the key components from future plasma exhaust processing loops are required prior to the construction of large technical installations. For this purpose, an experimental loop consisting essentially of a palladium/silver permeator, several circulation pumps, a buffer vessel, a ZrCo getter bed, two infrared analysers for the surveillance of methane, carbon monoxide and carbon dioxide, and two nickel catalyst beds has been planned in detail and is now under construction. Nearly all components of the loop are already available. The analytical equipment is presently being calibrated. The loop, which will be installed in a glove inside the tritium laboratory, is designed for long-term operation with 1 g of tritium, using helium as a carrier gas and several impurities to simulate conditions during fuel clean up.

In technical experiments employing a 1 kg nickel catalyst reactor in combination with a palladium/silver permeator having a permeation surface area of 0.12 m<sup>2</sup> up to 0.8 l STP CH<sub>4</sub>/min could be decomposed over an extended period of time. In addition, extended tests with the same permeator were carried in a flow system using the back pressure as a parameter. It was shown that the non-permeated hydrogen fraction is directly proportional to the back pressure on the secondary of the permeator. Presently, large scale experiments involving the installation of several 15 and 150 N m<sup>3</sup>/h NORMETEX pumps are in preparation.

#### Staff:

M. Glugla

R.-D. Penzhorn

K.H. Simon

### Subtask 2.2

The plasma chamber of a fusion reactor is filled with a large gas volume (about 100 kmol) after an accidental air inbreak. It consists essentially of > 95 % air with water vapor up to a value corresponding to the water vapor pressure at the prevailing temperature (< 2.8 %) together with hydrogen isotopes (< 3 %) and some minor impurities. In addition, up to 2 kg of DTO can be released from the torus wall when the gas is pumped out. To process this gas a concept based on a combination of catalytic reactors and palladium/silver permeators has recently been proposed. In this communication some preliminary results that demonstrate the feasibility of this process concept are reported.

Water was vaporized employing a constant temperature bubbler with CO as a carrier gas (see. Fig. 33). The CO flow

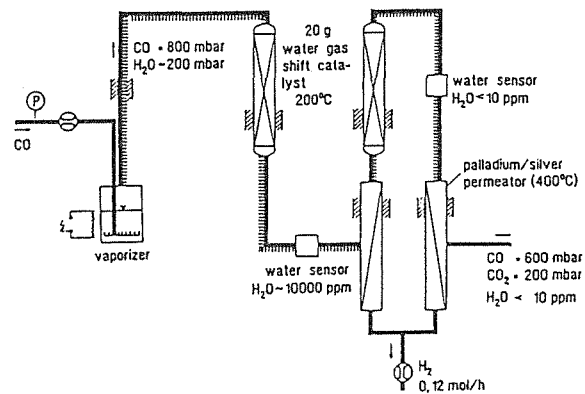
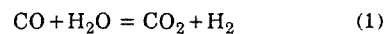


Fig. 33: Schematic drawing of the experimental arrangement (the comb shape lines indicates heat tubing)

rate and the temperature of the vaporizer were selected as the experimental parameters. The moisture content to the CO carrier gas was controlled after each of the two water gas shift catalyst reactors employing Panametric Systems monitors. The sensor installed behind the first catalyst bed had a range of 100 - 10000 ppm and that after the second bed a range of 10 - 1000 ppm. All other gases were analysed gas chromatographically employing either a Porapak R (for CO and CO<sub>2</sub> using He as a carrier gas) or a Porapak Q (for H<sub>2</sub> using N<sub>2</sub> as a carrier gas) column. The catalyst beds were filled with 20 g each of a zinc stabilized copper chromite catalyst. The catalytic bed was packed with pellets ( 5 mm outer diam. and 5 mm high) up to a 81 mm high column with an outer diameter of 16 mm. The catalyst beds were operated at 200°C. Hydrogen produced in the so called water gas shift reaction



was removed from the CO/CO<sub>2</sub> carrier gas with the help of a palladium/silver permeator (total permeation surface = 285 cm<sup>2</sup>). The permeation membrane was kept at a temperature of 400°C to avoid (reversible) poisoning by CO. The hydrogen permeated was pumped with a turbomolecular pump system.

Typical break-through curves observed after the first catalyst bed as a function of the CO flow rate have been plotted in Fig. 34 for various initial water partial pressures. Water concentrations in the effluent gas, shown on the lower left side, were calculated from known thermodynamic data ( $K_p(200^\circ\text{C}) = 255.67$ ). It is seen that with decreasing initial water partial pressure the break-through occurs at increasingly higher CO flow rates. As expected, the measured water partial pressures in the effluent gas were at all times higher than the calculated equilibrium partial pressures. In addition, experimental results on the conversion of water via two consecutive water gas shift catalyst reactors operated at 200°C with a palladium/silver permeator placed in between were obtained. In accordance with material balance considerations, the partial pressure of CO<sub>2</sub> and H<sub>2</sub> in the effluent gas of the first catalyst bed were found to be approx.

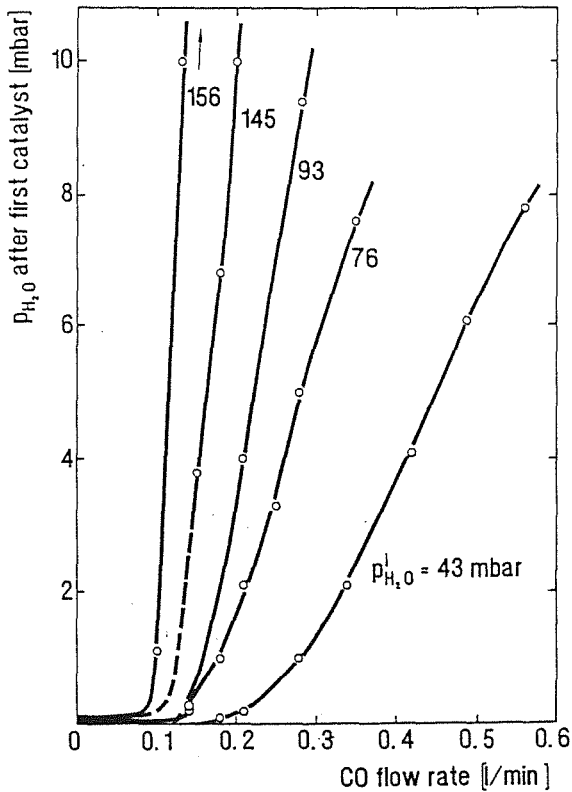


Fig. 34: Experimental H<sub>2</sub>O break-through curves after the first catalyst bed. The initial water partial pressure  $p_{H_2O}^i$  at the inlet of the catalyst bed are indicated on each break-through curve. The horizontal lines on the lower left side of the figure give the calculated equilibrium concentrations as obtained from thermodynamics

equal. The equilibrium water partial pressures at the outlet of the second permeator were calculated using the highest water partial pressure measured after break-through behind the first catalyst reactor. Even under these conditions the H<sub>2</sub>O partial pressure in the effluent gas from the second permeator was in all cases lower than the detection limit of the used sensor, i.e. 10 ppm. This high overall conversion is ascribed to the increase in CO/H<sub>2</sub>O ratio from the inlet of the first to the inlet of the second catalyst reactor (a high ratio favours the displacement of the equilibrium of reaction (1) towards the products).

From the results described above it is concluded that with a combination of two water gas shift reactor/palladium silver permeator stages a nearly quantitative conversion of hydrogen isotopes bonded in water into molecular hydrogen of high purity (99.9999%) can be achieved; the waste gases CO and CO<sub>2</sub> contain very small fractions of unconverted water and hydrogen. If required, the process performance can be further improved by the inclusion of additional catalyst/permeator stages.

With the experimental apparatus used in this work up to 58 g H<sub>2</sub>O/day could be converted into molecular hydrogen. To

increase the throughput a scaled up version of the equipment is presently under construction.

Staff:

M. Glugla  
K. Günther  
R.D. Penzhorn

Subtask 2.3

1. Introduction

An experimental program is carried out at the PEGASUS facility to investigate the applicability of metallic getters for gas purification in tritium technology. The aim is to remove gaseous impurities like N<sub>2</sub>, CO, and CO<sub>2</sub> from a helium gas stream and to recover chemically bound hydrogen isotopes by decomposition of hydrocarbons, ammonia and water.

The main program steps are:

- A. Inactive tests with various getter alloys to study sorption rates, retention capacities, and cracking capabilities as a function of temperature, flow rate, and presorption.
- B. Tracer level tests with tritium and tritiated compounds to study isotopic effects and the influence of the  $\beta$ -activity on the kinetics of the gettering and cracking processes.

2. Experiments

Test with five different non-uranium getter beds were carried out with the following aims:

- a) to find out the getter with the best properties for the removal of the most crucial impurities, i.e. the hydrocarbons;
- b) to compare the hydrogen equilibrium pressures as a function of the hydrogen load on the getters;
- c) to study the co-sorption behavior of CO and H<sub>2</sub> with respect to the potential formation and release of CH<sub>4</sub>.

3. Results

- a) The sorption of CH<sub>4</sub> on a getter bed during continuous gas circulation is described by the concentration half life  $t_{1/2}$  which can be derived from the experimental concentration curves as follows:

$$c(t) = c_o \cdot \exp\left(-f \cdot \frac{D}{V} \cdot t\right)$$

with  $c_0$  = initial concentration  
 $f$  = purification factor  
 $V$  = gas volume (NTP)  
 $D$  = gas flow rate

and

$$t_{1/2} = \frac{V \cdot \ln 2}{D \cdot f} \quad f = \frac{V}{D} \left( - \frac{d \ln c}{dt} \right)$$

Results for the purification factor  $f$  and the half period  $t_{1/2}$  are shown in Table 4 for several tests. In addition, this table includes other experimental parameters like the mass  $m$  of the getter material and the getter temperature  $T$ . The gas flow rate was 1 l/min and the pressure at the getter input was 1.2 bar in all cases.

Table 4: Results for Getter Tests with CH<sub>4</sub>

Test No.	Getter *)	m (g)	T (°C)	f	t <sub>1/2</sub> (min)
PV-2c	ST-707	700	400	0.631	21.5
PV-2e	St-707	700	600	0.830	17.0
PV-5	ST-101	700	600	0.665	21.4
PV-6	ST-198	700	600	0.977	15.0
PV-8	ST-198	700	400	0.330	45.3
PV-4	HTR-1	3000	400	0.392	37.4
PV-9	HTR-1	3000	500	0.736	19.5
PV-14	HTR-2	3000	400	0.955	15.0

\*) getters ST-101, ST-198, and ST-707 were purchased from SAES/Milano;  
 getters HTR-1/2 were purchased from HWT in Mülheim/Ruhr

The most attractive result was obtained for the getter HTR-2 with a high purification factor of  $f = 0.955$  at already  $T = 400$  °C. This is obviously due to the catalytic effect of Ni, which is additionally contained in this getter (Ti-V-Fe-Ni-Mn) in comparison to the getter HTR-1 (Ti-V-Fe-Mn).

b) The hydrogen equilibrium pressure of the getter ST-707, which is known from the literature, has been compared with the results of a H<sub>2</sub> loading and de-loading test carried out with the getter HTR-1 at 400 °C. Figure 35 indicates that  $p_{eq}$  is several orders of magnitude higher for HTR-1 than for ST-707. ( $p_{eq}$  for ST-198 and ST-101 is even lower than for ST-707.) The high equilibrium pressure is a great advantage of the HWT getter, because it is undesirable to have a high tritium inventory in the getters during the purification process

and, furthermore, to need long pumping times at UHV pressures to remove the residual tritium when the getter is to be disposed after exhaustion of its getting capacity.

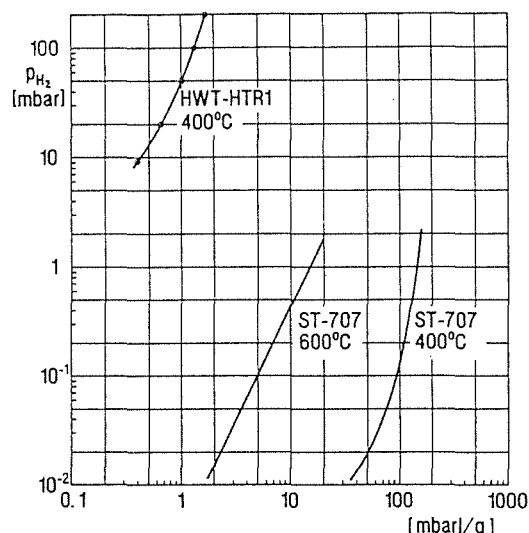


Fig. 35: H<sub>2</sub> Equilibrium Pressure for Getters HTR-1 and ST-707

c) A co-sorption test was carried out with 10.5 mbar CO, 49.5 mbar H<sub>2</sub> and 1290 mbar of He to study the interaction of CO and H<sub>2</sub> on the getter HTR-1 as a function of temperature. The gas was circulated through the getter for 20 min at  $T_G = 50, 150, 200, 250, \dots, 400$  °C and analyzed following to each temperature step.

The results reveal (see Fig. 36) that by the contact of the gas with the getter an increased amount of methane is formed at  $T > 200$  °C due to:



The oxygen is completely gettered while a considerable fraction of the CH<sub>4</sub> is not sorbed under these conditions.

As a consequence we propose to use two getters in series: the first to be operated at 250 - 300 °C for the removal of O<sub>2</sub>, H<sub>2</sub>O, CO, and CO<sub>2</sub> and the second to be operated at 400 - 500 °C for the removal of residual amounts of these species as well as for the removal of N<sub>2</sub> and CH<sub>4</sub>.

#### 4. Preparations for Tritium Tracer Tests

A tritium retention system (TRS) for the glovebox atmosphere has been installed and tested by adding 0.1 % H<sub>2</sub> to the air of the glovebox. During the purification process, the H<sub>2</sub> is oxidized by a Pd/alumina catalyst and then retained as H<sub>2</sub>O on a X-13 mol sieve. In the first tests, the TRS was found to work very inefficiently: a time of 330 min was needed to reduce the H<sub>2</sub> concentration by 90 %. After activation of the catalyst at 300 °C, however, it was possible to reduce the H<sub>2</sub>

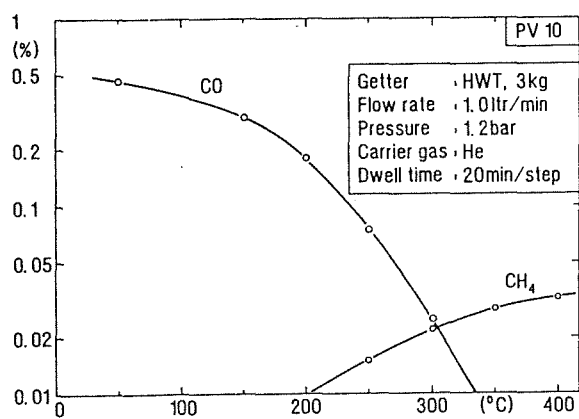


Fig. 36 : Sorption of CO and Formation of CH<sub>4</sub> during Stepwise Temperature Increase

concentration by 99 % within about 30 min. After these tests, it was decided to install a heating device for the catalyst to further increase its efficiency and to allow an in-situ regeneration when necessary.

Staff

H. Albrecht

W. Asel

U. Kuhnes

## TEP3 Tritium Storage

### Subtask 3.1

Intermetallic compounds that absorb large quantities of hydrogen gas are of technological interest to tritium processing facilities, provided the hydrogen is rapidly absorbed, the immobilized gas can be easily recovered and the hydride is reasonably stable towards air and other gaseous impurities of the fusion fuel cycle. One promising intermetallic compound that could substitute uranium for the transport, storage, and pumping of tritium is ZrCo. ZrCo alloy with a 1:1 ratio of the component atoms was selected because an intermetallic compound of this composition absorbs the largest amount of hydrogen.

Large samples of ZrCo alloy powder in the hydride form were prepared by high pressure hydrogenation ( $0.4 < p_{H_2} < 17.5$  MPa) of small pieces of the alloy ingot (each of about 10 g) at room temperature. The approx. hydrogen content of the samples was determined by weighing and by thermogravimetry. The mean loading from 14 different experiments with excess hydrogen was found to be  $ZrCoH_x$  with  $x = 2.91 \pm 0.04$ , which yields a stoichiometry close to  $ZrCoH_3$ . To produce activated ZrCo powder the hydride was dehydrogenated under high vacuum ( $10^{-4}$  Pa), first at 500 °C for 4 hours and then at 700 °C for another hour. Under these conditions a material with a specific surface area of  $0.40 \pm 0.03$  m<sup>2</sup>/g was obtained.

XPS depth profiles of the ZrCo hydride up to 30 nm yielded, in addition to the signals of the main surface components ( $ZrO_2$  and a Zr suboxide), another signal at 179.6 eV, i.e. 0.4 eV higher than that of Zr<sup>0</sup> in ZrCo alloy. This value agrees well with that reported for Zr-H in  $ZrCoH_3$  if the influence of the H<sub>2</sub> concentration on the binding energy of the Zr peak is taken into account. The chemical shift of the Zr 3d level to higher binding energies indicates an electron transfer from the metal to the hydrogen atom. On the other hand, the hydridation was found to have no effect on the Co 2p<sub>3/2</sub> binding energy, suggesting that upon hydriding the charge adjustments proceed only through electron density withdrawal from Zr atoms. Analogous observations have been reported for ZrNi.

Pressure-composition isotherms for the loading and deloading processes of the ZrCo/H<sub>2</sub> and ZrCo/D<sub>2</sub> systems were determined in the temperature range 150 - 300 °C employing a volumetric procedure (Fig. 37). Two different samples, one obtained from SAES, Italy, and the other from JAERI, Japan, were used in these experiments. The isotherms obtained with the two samples were practically identical. In agreement with data from the literature the isotherms show slightly sloping plateaus at the higher temperatures within the composition range  $ZrCoH_{0.5}$ - $ZrCoH_{2.0}$ , the length of the plateaus decreasing with increasing temperature. The equilibrium pressures of D<sub>2</sub> over the ZrCo deuteride were found to be somewhat higher than those of H<sub>2</sub> over the corresponding hydride at temperatures above 250 °C.

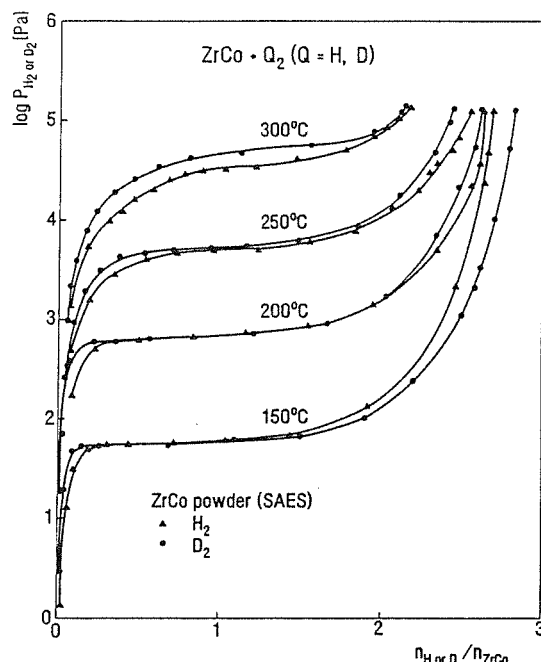


Fig. 37: Pressure-composition isotherm of the systems ZrCo/H<sub>2</sub> and ZrCo/D<sub>2</sub>

For a given hydrogen/metal ratio, the temperature dependence of the equilibrium pressure can be described by the relationship

$$\log P_{H_2 \text{ or } D_2} = -A/T + B \quad (1)$$

in which P is the pressure (Pa) and T the temperature (K).

Table 5 gives A and B parameters together with  $\Delta H_{Q_2}$  and  $\Delta S_{Q_2}$  values obtained from p-T data at various  $ZrCoQ_x$  (Q = H or D). At low temperatures the ZrCo deuteride is expected to be more stable than the corresponding hydride, i.e. the deuteride has a lower equilibrium pressure than the hydride. Using the A and B values estimated over the plateau regions dissociation pressures at room temperature of  $4 \times 10^{-3}$  and of  $2 \times 10^{-3}$  Pa were calculated for the hydride and the deuteride, respectively. Because of the dominance of the entropy term at higher temperatures a reversal in stability is observed. Using the data in Table 5, the temperature at which the stability cross over takes place is estimated to be 160 °C. A desorption equilibrium pressure of 100 kPa is reached at 342 °C with the hydride and at 325 °C with the deuteride, in line with the above discussed stability considerations. It is concluded that the temperature required for the recoverability of tritium from ZrCo tritide is comparatively moderate.

#### Staff:

Dr. M. Devillers (visiting scientist)

Dr. R.-D. Penzhorn

M. Sirch

Dr. E. Willin



x	A	B	-ΔH (kJ/mol)	-ΔS (J/mol K)
hydrogen				
0.8	4266	11.80	81.7	130.2
1.0	4311	11.91	82.5	132.3
1.2	4315	11.94	82.6	132.9
1.5	4346	12.06	83.2	135.2
1.8	4113	11.76	78.7	129.4
2.0	4216	12.12	80.7	136.3
mean values	4261 ± 85	11.93 ± 0.14	81.5 ± 1.6	132.7 ± 2.7
deuterium				
0.8	4537	12.46	86.9	142.8
1.0	4575	12.56	87.6	144.7
1.2	4604	12.64	88.1	146.3
1.5	4623	12.73	88.5	148.0
1.8	4579	12.73	87.7	148.0
2.0	4508	12.76	86.3	148.6
mean values	4571 ± 42	12.65 ± 0.12	87.5 ± 0.8	146.4 ± 2.3

Table 5: Van't Hoff parameters and thermodynamic functions for the absorption of H<sub>2</sub> and D<sub>2</sub> by ZrCo alloy in the plateau region (0.8 < x < 2.0)

## NSN 1      Neutronics Data Base for Shielding

Within the frame of the newly established task NSN1 KfK supports the evaluation and improvement of basic nuclear data, relevant for shielding calculations, and their critical use in test calculations with the newly developed transport code system GANTRAS using double-differential cross-section data (DDX) in a rigorous way.

### Subtask 1.1

In the beginning phase of task NSN1 the cross-section data of the iron isotopes Fe-54, -56, -57 and -58 have been reevaluated in the resolved resonance range.

The evaluation of covariance data for these cross-sections is underway.

### Subtasks 1.3 and 1.4

For the test shielding calculations the one- and two-dimensional transport modules ANTRA1 and ANTRA2 of the GANTRAS-system will be used. ANTRA2 has been further developed to include an improved calculational procedure for the integration of the scattering kernel over the scattering angle. The previously used integration procedure, based on the so-called I\*-method, has been proven to be not well suitable for the treatment of two-dimensional transport phenomena.

### Staff:

F. Fröhner

U. Fischer

A. Schwenk-Ferrero

E. Wiegner

## RHS 1      **Qualification of Standard Components**

The main objective of this task is, to standardize and qualify basic machine components and to develop remote techniques to assemble and disassemble these items. The output from this task will result in data sheets for the NET Remote Handling Manual which will define the standard components to be used in the NET design. The basic machine components to be qualified are:

- Electrical connectors
- Pipe connectors
- Fluid connectors
- Welded connectors
- Cryogenic connectors

of special importance is the demonstration of connecting techniques.

### Subtask 1.1

The objective of this sub-task is to select and rationalize a range of electrical connectors suitable for remote handling.

This work follows from the results of the work carried out under the NET contracts No. 201-85-1 and 313/88-7.

The electrical connectors will be selected after carrying out a series of remote operations on a mock-up using typical remote handling equipment.

In the period under review the preselection of the NET remotely handled electrical connectors (RHEC) for normal application has been made.

A proposal for a test program for the push-pull connectors has been arranged and submitted to NET. The mock-up has been designed and manufactured. The items to be tested have been identified, the procurement has been completed.

### Subtask 1.2

The aim of this task is to select and rationalize a range of flange connectors suitable for remote handling.

These connectors will be used for connecting pipes which may contain water, liquid metal, or vacuum.

In the period under review the rationalisation of water, vacuum and liquid metal connectors has been completed. The drafted data sheets for the Remote Handling Manual have been provided.

The fatigue and remote handling tests with a JET vacuum flange of nom. dia of 225 mm have been finished.

The new clamping ring connector using toggle joints as elements creating forces in between the flanges has been mounted and first functional tests have been successfully

performed. The test of the soft iron material as a gasket material for liquid metal pipe connections has been continued. The description of the test rig and the general test results have been submitted to NET. The draft of the first test report is under preparation.

### Subtask 1.3

This subtask intends to select and rationalize a range of small bore fluid connectors suitable for remote handling.

These connectors will be used for coupling flexible hoses which may contain water or compressed air.

Work has been started with the preparation of a Requirement Definition Document (RRD). The draft of the RRD has been discussed with the NET-Team. The state of the art has been investigated.

### Subtask 1.4

The main objective of this task is to develop remote techniques and tools to provide welded pipe connections and welded vacuum lip seals for flanges.

In the period under review the tools for lip welding and -cutting have been manufactured and assembled. The electrical installation of the test devices is in progress. The welding source and the control system for the welding device has been selected and ordered.

The design of a pipe welding unit for welding pipe diameters of  $\geq 250$  mm is under preparation. In the test rig FEROS basic tests with remotely operated welding and cutting units have been continued.

### Subtask 1.5

**BERT is a full** size mock-up of the NET connector box which houses the feed pipes leading to the blanket segments.

The BERT test rig is used to test and develop remote handling techniques for pipe connectors and pipe jumpers as well as procedures and equipment for remote cutting and leaktight rejoining of individual blanket segments.

The test rig has been fully equipped with pipe jumpers. The remotely operable overhead crane has been commissioned. The remote exchange of pipe jumpers has been started.

The design of the segmentation and layout of the lips has been finished. The draft of the first intermediate report has been completed.

### Subtask 1.6

Within the framework of this subtask development work is carried out on remotely operated cryogenic connections

suitable for NET remote handling devices used inside the biological shield.

Remote handling devices to be used for the disassembly and reassembly and past maintenance inspection are being investigated.

Work is focusing on the basic design of multipipe - type cryolines similar to that shown in an internal report submitted to NET in April 1989.

Two alternative solutions for cryogenic connections are under discussion. The remote handling capability and the application of remote welding and cutting devices are under investigation for the most envisaged solution, i.e. a connector for a number of concentric pipes in a circumferential outer pipe.

Staff:

L. Gumb

U. Kirchenbauer

A. Schäf

M. Selig

D. Stern

M. Trettin

R. Ullrich

## RHS 2      Material Tests for Remote Maintenance Equipment

### Subtasks 2.1 and 2.3

With view to the planned gamma irradiation test for angular sensors in the BR-2 reactor, the main activities were directed to the design and construction of a test-rig for a couple of multi-turn resolvers identically mounted and operated by the use of pneumatic drives. Four resolvers were pretested in the meantime and two selected devices will become calibrated and temperature hardened in a heat chamber with the objective to determine their properties and to get a reference before starting the gamma irradiation test. Most of the pneumatic drive and supplying components are already available and their assembly was started. The manufacture of the test-rig enclosure and protecting tube with its mechanical supports and adapters was started mid 1989. Particular attention was paid to the availability of radiation hardened instrumentation cables, type RADOX, to be used for the resolvers. They are covered with the longest delivery time.

Due to residual errors associated with mechanical inherent and external coupling inaccuracies, investigations with standard and low-cost angular encoders were performed in parallel [1]. The aim was to study the drive and coupling errors under severe and representative temperature conditions up to 150° C. From these tests it was shown that all three chosen Heidenhain incremental encoders implied systematic errors in the same magnitude as it is anticipated for the absolute measuring resolvers, and, consequently an accurate calibration of the resolvers is essential. It is foreseen to perform the individual calibration in a mock-up equipped

with an oven and a high precision angular reference system type inductosyn.

Besides the radiation hardening tests for sensors, KfK started to investigate also motors and cables for the transporter and work units of the in-vessel handling unit. These tests are subdivided in out-of-pile and in-pile tests. The first ones will be performed at a motor torque bed of KfK and serve as reference measurements. For this the test bed is installed and will be equipped now by a temperature chamber. Also the test samples are ordered and will be available by April 1990. In-pile tests will be carried out at the BR2 in MOL.

### References:

- [1] Rohrbacher, H.A., Bartholomay, R.: Winkel-Mess-Systeme fuer die NET-IVHU-Grundlagen und erste Labor-Experimente.  
unpublished report of KfK, 6.3.1988

### Staff:

I. Aberle  
B. Bartholomay  
B. Haferkamp  
D. Klein  
K.H. Lang  
W. Link  
G. Mueller  
H.A. Rohrbacher  
P. Schultheiss  
A. Suppan

### **RHS 3      Mock-up of In-Vessel                  Components and Test Facilities**

#### **Subtask 3.2**

In-vessel plasma facing components will be subject to the most demanding operation conditions and are expected to require relatively frequent maintenance. To ensure that it will be possible to carry out these activities safely and efficiently by remote handling techniques, these maintenance tasks have to be demonstrated in mock-ups. KfK has taken charge to construct mock-ups for divertor and first wall armour tiles. The activity is closely connected with the construction of the testbed EDITH (Experimental Device for In-Torus Handling). The planning has a delay due to the lack of requirements definition which will be available by the end of October 1989.

#### **Staff:**

H. Hübener

A. Suppan

## **RHI 1      Blanket Handling Device (BHD)**

### **Subtask 1.1**

In continuation of the NET contract 282/87-10FU D NET, NET Blanket Handling Device, KfK has finished the investigation of handling concepts. The results including a proposal for a handling device to change blanket segments are documented in the draft of a final report which was sent to NET. Their comments will be discussed in a meeting in October 89. In the following a design review meeting is envisaged to get conclusions, requirements and recommendations for the preliminary design of the handling device.

No activities were performed regarding the control of the handling device during this period, but the control system was considered as an important subsystem to be controllable via the NET Remote Handling Workstation.

#### **Staff:**

B. Haferkamp

W.E. Hörl

K. Leinemann

W. Link

E.G. Schlechtendahl

A. Suppan

## RHT 1 In-Vessel Handling Unit (IVHU)

The main objective of this task is the design of an In-Vessel Handling Unit (IVHU) for inspection, repair and replacement of NET in-vessel components. Main component of this equipment is a transport system with attachable multi-purpose and special work units. KfK is developing such a system on the basis of an articulated boom.

### Sub-task 1.1

The work for the preliminary design of the IVHU transporter was continued. It is based on the results of the design review meeting in March 1989 and the revised requirements definition documented in [1].

### Mechanics

The transporter (Figure 38) is composed of the transport carrier with a cantilever arm at which the articulated boom is linked. Based on a reach envelope of  $\pm 90^\circ$  of the torus the boom has 4 links. They are symmetrical and have a box cross section with a height of 1.5 to 2 m and a width of 0.6 m. Its front link is designed as an interface for the different work units. The operating range of the link joints is  $240^\circ$ . They are operated by coaxial drive units. Their design was launched on the basis of JET experience. Alternative drive unit options were considered and within the frame of this investigation also linear actuators were designed.

Conceptual design work was carried out for the work units. Their preliminary design can be started at the end of October 1989 when the requirements of divertor and tile handling will be fixed by the NET-Team.

### Control system

Based on previous NET remote handling control system design work the requirements for the In-Vessel Handling Unit (IVHU) control system were specified [2]. In the three-level hierarchy of the NET remote handling control system the IVHU control system represents the motion control subsystem. It is controlled by the Remote Handling Workstation, which provides the man-machine interface and several task level support tools for the operator. The basic requirement for the IVHU control system is a reasonable dynamic behaviour of the IVHU, but the integration into the overall control system demands for special functions. These are mainly single command execution (manual mode), program execution (automatic mode), on-line teach/repeat, backtracking, logging, and monitoring. All functions of the control system and all relevant parameters have to be accessible from the remote handling workstation. A NET proposed investigation shows, that the JET TARM control system fulfills a reasonable subset of these requirements. That means that the TARM control system with some modifications can serve as a basis for the IVHU/EDITH control system development. This collaboration with JET saves costs and facilitates the transfer of further KfK results also to JET, especially in the areas of man-machine interface development and advanced closed loop control system techniques.

The spatial simulation system KISMET, designed as a subsystem of the NET and JET Remote Handling Workstations was enhanced by new features:

- graphic supported camera and video crossbar-switch control for 4 CATROB cameras demonstrating the integrated viewing concept,

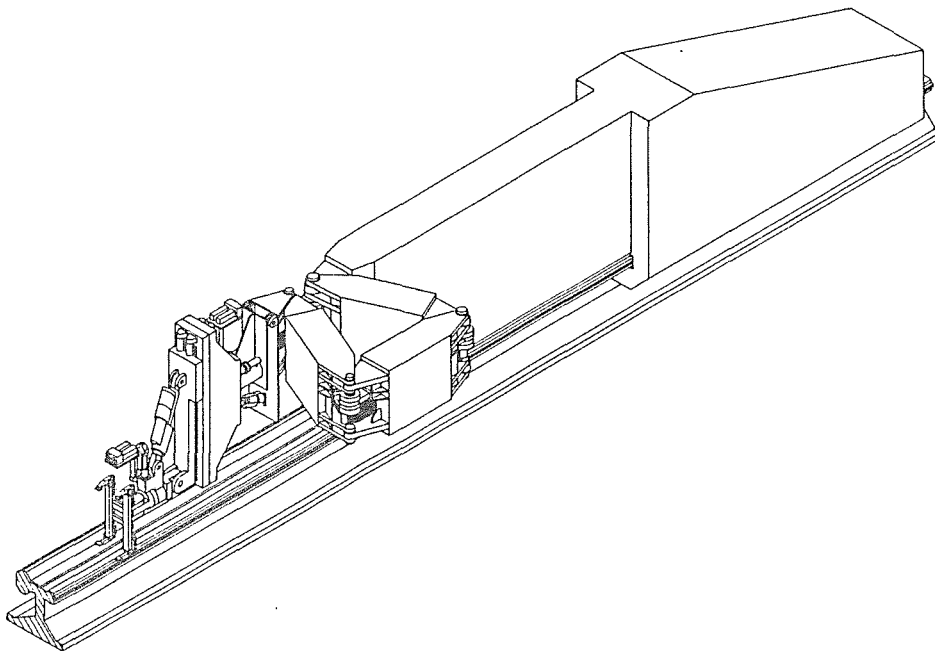


Fig. 38 : Transporter with divertor handling unit



- completion of the IRDATA interpreter needed for program transfer between workstation and control system,
- completion of the CATROB environment model by modelling the divertor cassette, which will be used for remote handling tests.

Tests were done successfully in the CATROB test site, special features of the simulator were tested within the EMIR context.

As spin-off, KISMET is being used by DLR Oberpfaffenhofen for remote handling applications in space, and by DWK IPA Stuttgart for simulation of maintenance work in a hot cell of WAK. IPA Stuttgart has signed a license agreement, and DTH (Danish Technical University) plans to use KISMET for off-line programming of industrial robots. First practical experiences of these partners in those different applications led to improvements of the KISMET command set and useful modifications.

The documentation of KISMET is nearly completed.

The generation of models, which are suited for real-time simulations, is also one of the purposes of the program ROBOT, running in the APPLICON-BRAVO-CAD environment. Version 1.0 has been used again for kinematic design studies, especially in the framework of the dynamic simulations for the NET-boom as well as for EDITH. During the last months, however, a version 2.0 of ROBOT has been completed, which is dedicated mainly to the generation of geometrical and kinematical models for use by real-time simulation systems. It is supporting now all modelling features which are used within KISMET.

ROBOT version 2.0 has been tested extensively in the framework of a task, where a really existing complex scenario with nuclear context had to be modelled for simulation of repair work in KISMET. The scenario has been modelled successfully within BRAVO/ROBOT, and the models transferred to KISMET worked satisfactorily.

For the application of KISMET to JET maintenance a solid model of the ex-vessel environment was generated on the CATIA CAD-system and then transferred to KISMET. This can be seen as a successful acid-test of the CATIA-KISMET model transfer processors. At this stage the model represents the torus hall, the main parts of the machine and the remote handling Equipment including the BOOM and the TARM (Figure 39). The data model allows the user to choose from up to three geometrical representations of one and the same object.

The AMBOSS dynamic simulation system was used in the EDITH redesign cycles for the actuator layout, especially for computing the bearing loads and needed drive torques. The determining loads for the drives are not the motion loads but the reaction torques against loads at the tip of the boom.

The **motion control** of the IVHU can be roughly characterized as a standard industrial robot controller combined with a part which is devoted to manual mode operation. Hence the motion control permits essentially two operation modes:

- In manual operation mode an operator controls the system by single commands which are executed immediately.
- In automatic mode programs written by an operator e.g. by offline teach-in are downloaded from the remote handling workstation to the motion control and executed automatically.

Other essential features for example are:

- The online recording of paths.
- Backtracking. This means that each movement of the boom is recorded automatically in manual mode to be able to move the arm backwards, e.g. to support the operator in cases of recovery.
- Reconfiguration.
- The possibility to control the transport unit in world coordinates (resolved motion control).

Position control is a vital part of the motion control system. The position control has to convert as exactly as possible and without delay the desired values given for example from a pathplanning-modul into a real motion. The effects of disturbances, e.g. force impacts, have to be compensated.

To meet the requirements for motion control and to achieve a good dynamic performance of the whole system, it may be necessary to implement advanced control algorithms like Inverse Model techniques [4] or adaptive control schemes. In a first stage it is intended to use and test a single joint control. A corresponding control design for EDITH was carried out in [5]. First a dynamic model of the boom was derived with the program-system AGRIS [4] supposing a rigid structure and some implications of the drive system. Based on this model a PD-controller was designed for each joint. Simulation results using the program-system ManDy [6] show that under the assumptions which were made in [5] a satisfactory dynamic performance is achievable.

Some theoretical work was done on the topic "Active Damping". This means in principle to stop mechanical oscillations. The oscillations have to be measured by special sensors (e.g. acceleration sensors) and then the control system has to calculate the corresponding movements to stop or at least to damp actively these oscillations.

The **drive unit control** is the lowest level of the control system. It will get the required control signals like revolutions and torques from the motion control. The drive units are equipped with brushless AC-servomotors. Their control behaviour is similar to those of DC-motors.

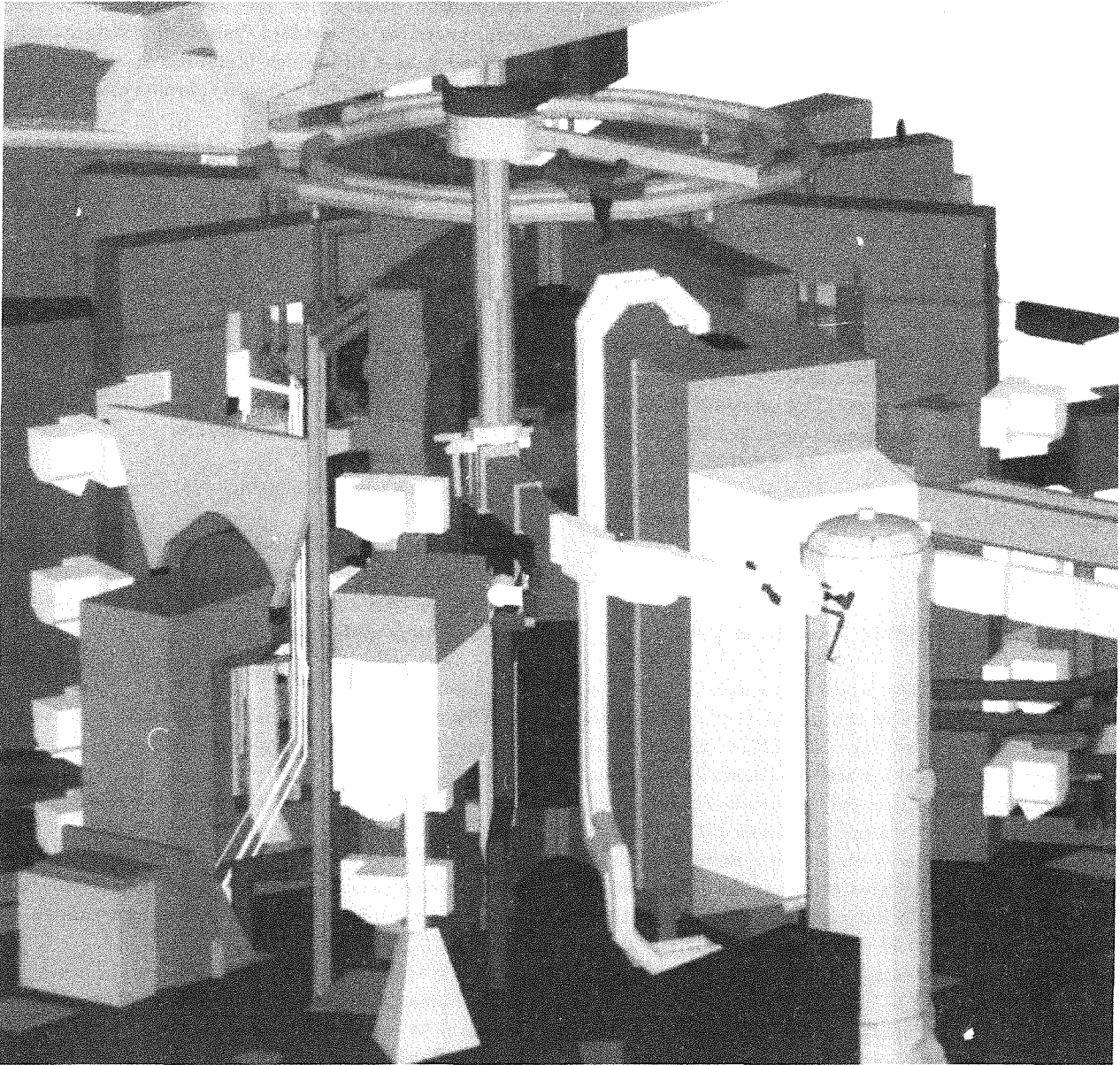


Fig. 39: KISMET model for JET ex-vessel maintenance

In order to eliminate backlash and to stiffen the transporter the drive units which are composed of two single drives each will have electrical backlash removal. Eventually possible oscillations of revolutions will have to be damped at the level of the motion control.

#### Ex-vessel surveying

The remote-controlled and CAD-supported surveying system GMS (Geometry Measurement System), developed by KfK, is equipped with two digital theodolites, a laser- and a camera-theodolite, completely controlled by a computer. To show the feasibility of the GMS-draft a prototype system, equipped with a single camera-theodolite is built up presently. The software needed for the data transfer CAD→GMS and the software for the control of the surveying process is already implemented and successfully tested. During the whole

surveying process the operator is guided interactively by the GMS-software and several theodolite parameters (e.g. the speed of the repeating motors) can be changed menu-driven. After an initialization procedure the theodolite is turned automatically into the direction of the nominal point position. For correcting the theodolite pointings, the operator can use a joystick, the cursor keys or a mouse.

To support the operator a computergraphic can be selectively superimposed on the TV-picture. This graphical support contains both the wire-frame model of the object and the target points of the theodolite. By this graphical support the operator can recognize easily the positions of the target points.

Up to now the operator has to level the theodolite manually using inclination adjusting screws. To realize the complete remote control, KfK has developed a servo-driven levelling

mechanism (s. Figure 40). This levelling mechanism is equipped with two inclinometers and the measured inclination is corrected by motor-driven spindles. The operating range is  $\pm 8$  gon and first tests had shown, that the levelling accuracy is better than  $\pm 0.01$  gon with respect to the horizon. The residual inclination will be compensated by the automatic height-index of the theodolite.

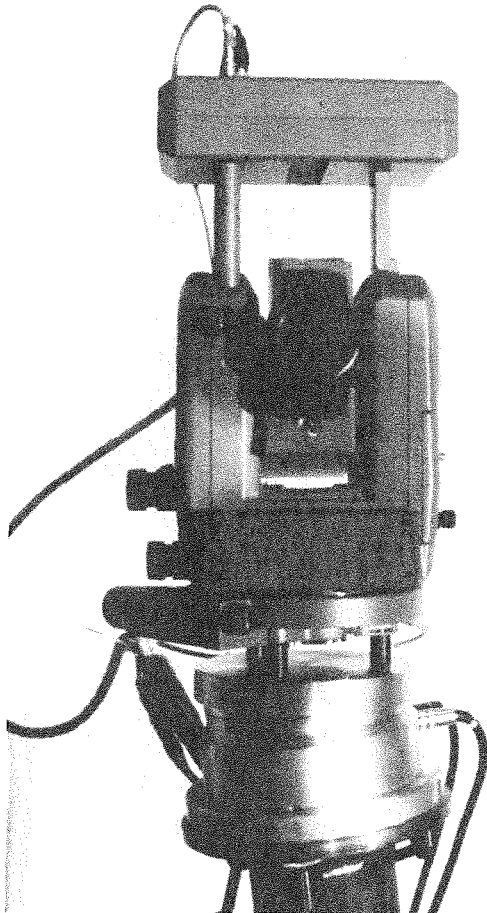


Fig. 40: Theodolite mounted upon the automatic levelling mechanism

### In-vessel surveying

In order not to break the vacuum, periscopes have to be used for the in-vessel surveying. Based on the experiences with the ex-vessel surveying a first design concept for a theodolite periscope has been outlined; for building up detailed designs definite informations about the in-vessel surveying processes are needed.

### Sub-task 1.2

The testbed EDITH (Eperimental Device for In-Torus Handling) is supposed to be the basis for the demonstration of in-vessel maintenance tasks for NET and to test components for the IVHU like drive units, the control system, sensor integration or signal transfer. The planning for EDITH is finished, call for tenders launched and available, respectively. Contracts for the mechanical parts, the drive

units and the control system will be placed by the end of 1989. Thus EDITH can go into operation by the end of 1990.

### Mechanics

EDITH consists of the articulated boom as it will be used also for the IVHU with a reach envelope of  $\pm 90^\circ$ . The boom is linked with a cantilever arm which again is connected with the support structure. The interface of the boom is supposed to carry the different work units. The testbed will be completed by mock-ups for tile and divertor plate handling.

**Structural Analysis** with respect to the re-design of the IVHU, and the optimization of the link cross-section for the testbed EDITH was carried out. The requirements of maximum vertical stiffness and minimum dead weight were taken into account.

One way to obtain a higher stiffness is to increase the link cross-section. The width of the links (0.6 m) is limited by the width of the entry port (0.8 m). But the height of the links was varied from 1.2 m to 2 m. This results in a reduction of the deflection (due to the dead weight and payload) from 62.3 mm to 51.8 mm.

Another way is to increase the wall thicknesses of the links. For a cross-section of  $1.2 \times 0.6 \text{ m}^2$  the wall thicknesses were increased from 6, 6, 8 and 12 mm to 6, 8, 20 and 50 mm, respectively. The deflection was reduced from 62.3 to 41.3 mm, but the dead weight was increased from 4.7 t to 7 t.

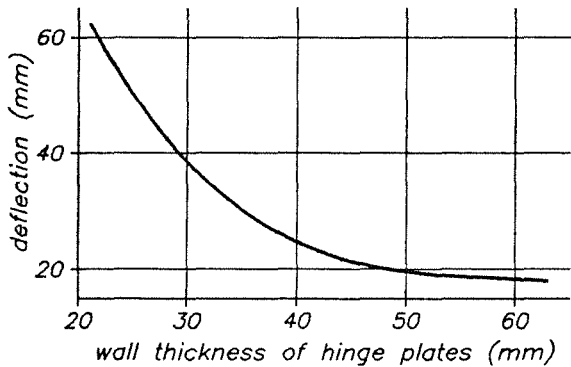
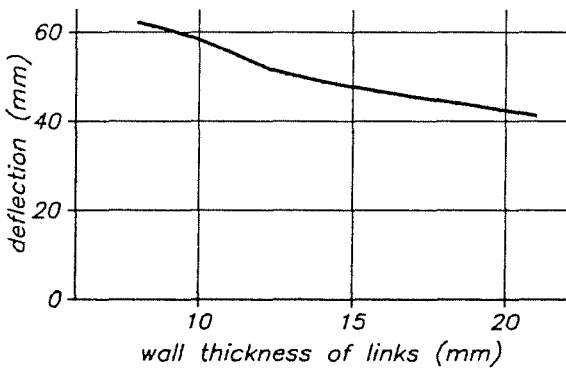
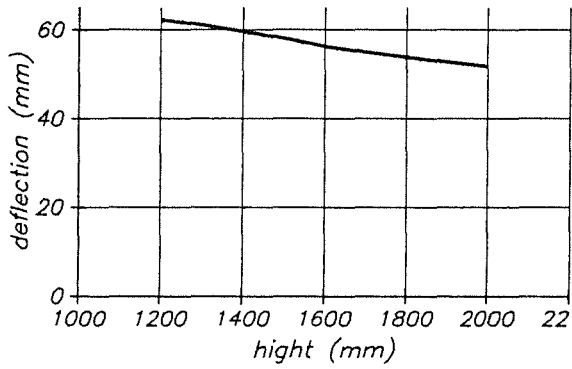
A third way is the increase of the wall thicknesses of the hinge plates. For a given cross-section ( $1.2 \times 0.6 \text{ m}^2$ ) and given wall thicknesses of the links (6, 6, 8 and 12 mm), the wall thickness of the hinge plates were increased from 21 mm to 63 mm. As a result the deflection was reduced from 62.3 mm to 20 mm and the dead weight was increased from 4.7 t to 5.8 t. In addition the hinge plates were reinforced by vertical stiffening plates.

The final thicknesses of link walls and hinges depend on fabrication problems and will be discussed with the supplier.

Figure 41 shows the deflection of EDITH for different cross-sections, different wall thicknesses of the links and of the hinge plates.

### References:

- [1] Maisonnier, D.:  
NET/ITER In-Vessel Transporters Requirements  
Definition for its Conceptual and Preliminary  
Design, NET N2/P/3240/1/A, draft 10.05.89
- [2] Leinemann, K.:  
IVHU Control System Requirements.  
unpublished Report of KfK, September 1989.



[7] Suess U.:  
Das Manipulatorsimulationssystem ManDy Version  
0.88,  
Unpublished report of KfK, December 1988

Staff:

- H. Breitwieser
- J. Fröhlich
- E. Holler
- B. Haferkamp
- J. Hübener
- H. Knüppel
- B. Köhler
- I. Kornelson
- R. Krieg
- U. Kühnapfel
- K. Leinemann
- W. Link
- A. Ludwig
- M. Mittelstaedt
- G. Müller
- J. Reim
- W. Pleschounig
- E.G. Schlechtendahl
- P. Schultheiss
- U. Süß
- A. Suppan
- E. Wehner

Fig. 41: Deflection of EDITH. Effect of wall thickness of the links, wall thickness of hinge plates and link height on the vertical deflection

[3] Breitwieser H.:  
TU-motion control specification -first draft-  
Unpublished report of KfK, May 1989

[4] Weber W.:  
Regelung von Manipulator- und Roboterarmen mit  
reduzierten, effizienten inversen Modellen.  
Fortschritt-Berichte VDI Reihe 8 Nr.183989

[5] Suess U.:  
1. Ansatz eines Modell- und Regelungsentwurfs  
für EDITH.  
Unpublished report of KfK, March 1989

## SEP 2 Environmental Impact of Tritium and Activation Products

### Subtasks 2.1 and 2.2

The foodchain model COMA which calculates the quasi dynamic transfer of tritium through the different parts of the ecosystem, was extended in the number of compartments considered during one run (Fig. 42), and also modified in the number and the declared values of the transfer rates. The atmospheric dispersion model for tritium transport in the environment MOTTE and the modified foodchain model COMA were combined to the model UFOTRI.

Within an ITER benchmark exercise, acute and long-term organ doses for accidental releases of tritium in the chemical forms of HT and HTO and for fixed atmospheric, soil and plant physiological conditions were calculated and compared with the results of other participants (Task 1). Here the importance of the consideration of the reemission process for the resulting dose was again established. Table 6 shows that for an HT release under stable atmospheric conditions the doses from inhalation and skin absorption increase by more than two orders of magnitudes, if reemission and transport processes (here for an integration time of one week) are taken into account.

The comparison of the benchmark results for the ingestion pathway showed large discrepancies between the different participants, what leads to the conclusion, that further analysing work has to be done. The present activities concentrate on describing the model UFOTRI, testing the foodchain model and the future coupling of UFOTRI to the program system UFOMOD.

Deterministic runs with the UFOMOD code were analysed for activation product releases assumed within the ITER benchmark Task 2. No dose assessments could be performed for the ingestion pathway due to missing nuclides in the corresponding data base. Therefore, a contract has been given to the Gesellschaft für Strahlen- und Umweltforschung (GSF) mbH to calculate with the foodchain model ECOSYS the data required in the ingestion model of UFOMOD.

Within the next half-year, these data will be implemented and the benchmark tasks will be completed.

#### Staff:

J. Ehrhardt

I. Hasemann

W. Raskob (DTI)

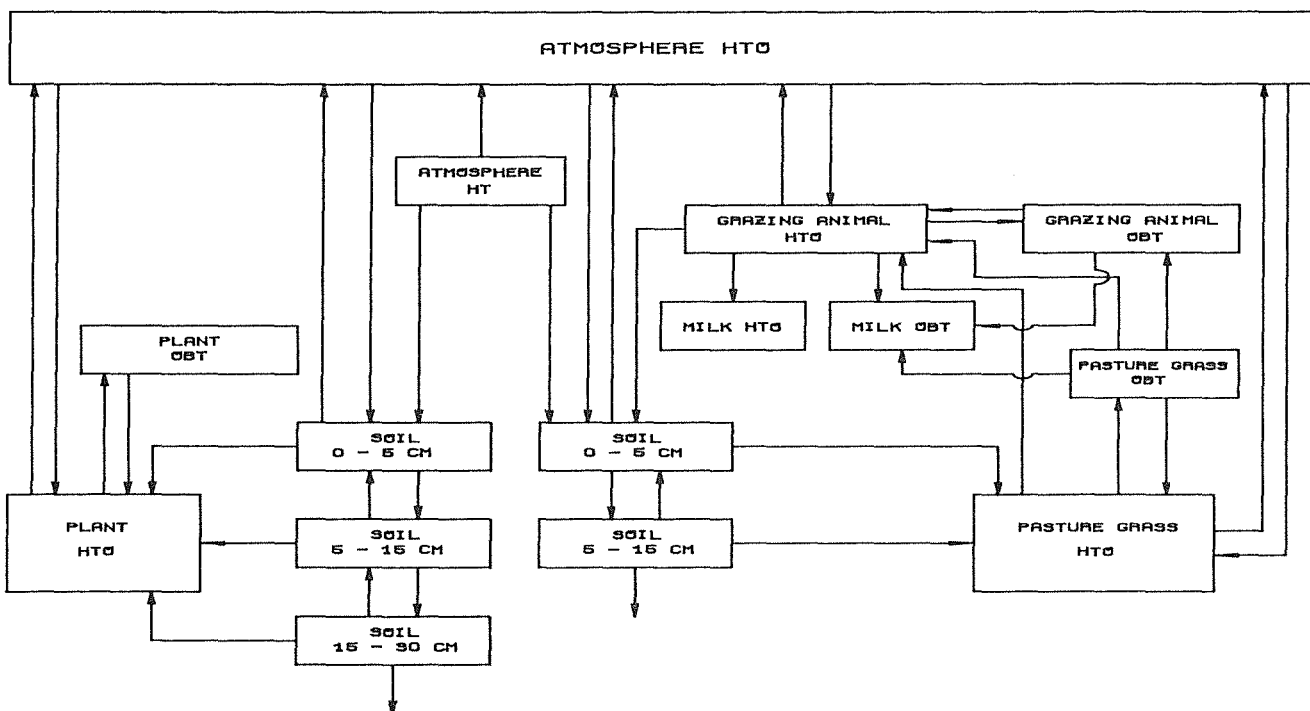


Fig. 42: Diagram of the modified foodchain model COMA

release height	early dose (inhalation and skin absorption) from plume passage (Sv)	early dose (inhalation and skin absorption) from pl. pas. + reemission (Sv)	chronic dose (inhalation and skin absorption) from pl. pas. + reemission (Sv)	early dose from ingestion (Sv)	chronic dose from ingestion (Sv)	sum of early doses (Sv)	sum of chronic doses (Sv)
10 m	3.1 E-7	1.8 E-4	4.9 E-4	3.6 E-4	7.8 E-3	5.4 E-4	8.3 E-3
20 m	2.1 E-7	8.9 E-5	2.4 E-4	2.2 E-4	4.6 E-3	3.1 E-4	4.8 E-3
60 m	5.9 E-8	9.3 E-6	2.5 E-5	3.7 E-5	8.9 E-4	3.8 E-5	9.2 E-4
20 m with building wake effects	2.3 E-7	1.2 E-4	3.2 E-4	2.4 E-4	5.5 E-3	3.6 E-4	5.8 E-3

Table 6: Plume centerline dose in 1 km distance for an HT release of 100g and dispersion category F

## **SEA 1      Specific Safety Related Recommendations for the Design**

### **Subtask 1.1**

Preparation of safety related recommendations aims at ensuring advice to the NET Team on safety and environmental questions. The task is performed in the frame of a working group consisting of members from CEA, ECN, JRC-Ispra, KfK, Riso National Laboratory, The NET Team and UKAEA.

In the period under review the previous draft on protection against non-ionizing radiation was revised.

In contrast to the existing international and national regulatory limits for ionizing radiation the situation in the field of non-ionizing radiation is more complex and the development of exposure limits is less consistent. In different countries there exist recommendations rather than regulations. Nevertheless, strong efforts in developing health criteria and exposure limits have been and are being made by the International Non-Ionizing Radiation Committee

(INIRC) of the International Radiation Protection Association (IRPA) in cooperation with the WHO.

Hence, a great number of details presented in the revised document is based on IRPA/INIRC recommendations.

The first part deals with static electric and magnetic fields, and with extremely low frequency fields. The second part is devoted to radiofrequency fields.

Since shielding and administrative measures for the protection of the station staff are mandatory anyway the potential hazard to the public is drastically reduced due to the present protection of the workers. For example, concerning the magnetic field in the environment of the plant an exposure in the order of magnitude of the earth's background is considered to be acceptable.

By the way, shielding measures against non-ionizing radiation will be necessary also for the protection of different electronic components of the plant.

#### **Staff:**

W. Kramer

### SEA 3 Reference Accident Sequences

#### Sub-Task 3.1

In cooperation with ENEA a list of reference accident sequences, to be considered for the magnet system, was set up. The Magnet Reference Accident Sequences (MRAS) are the following:

- MRAS-1: Growing normal conducting zone and failure of the magnet dumping system.
- MRAS-2: Low Ohm short at the coil terminals and emergency shutdown of the magnets.
- MRAS-3: Sudden loss of cryostate vacuum
- MRAS-4: Arcing at the current leads followed by a shutdown
- MRAS-5: Loss of coolant in a main coolant supply line
- MRAS-6: Fire in the magnet auxiliary system housing
- MRAS-7: Severe plasma disruption
- MRAS-8: Loss of site power
- MRAS-9: Earthquake
- MRAS-10: Drop of a heavy load (e.g. the in-vessel handling unit)

MRAS-11: Local heat spike at the TF magnet caused by a LOCA of the blanket cooling system in the upper connection box.

The work on MRAS-1 has been already started (see SEA3.2 and MSA 1). For the other reference accidents more detailed accident scenarios must be specified, based on the present design. The most important sequences will be investigated first to setup a preliminary report on magnet safety.

#### Sub-Task 3.2

For the performance and layout of experiments in the field of MRAS-1 it is necessary to get some feeling on the expected jump times between windings and pancakes. As presently no code is available to do this analysis it was concluded to perform a 2D anisotropic conduction analysis. The precision of this analysis is not very high, it is more an estimation of the order of magnitude. A small code was set up and some analyses were performed. The detailed results are given in an internal report (03.08.02.P06A). According to this simplistic analysis the jump time between windings for a conductor of the KfK-NET-TF type is 4 to 8 seconds. Between the pancakes the jump time is larger than 11 seconds.

To test the results of this analysis a winding / winding jump, observed at LCT with the KfK-LCT coil was recalculated. It turned out that the calculated jump time is much larger than the observed jump time. The reason for this discrepancy will be analysed.

Staff:  
R.Meyder



## BS DE-D-1 Solid Breeder Test Blanket Design

The KfK solid breeder blanket concept is described in detail in Ref. 1 and in previous semi-annual Reports, only the recent changes will be mentioned here.

The NET test blankets should be DEMO relevant. Therefore a design study has to be conducted showing that the blanket concept envisaged has the potential to be used in a DEMO reactor. As a first step the coolant system of the canister blanket concept previously designed for NET was slightly modified to satisfy the tentative DEMO parameters. This required a slight increase of all coolant tube diameters and an increase of the helium pressure from 6 MPa to 8 MPa. In order to maintain the tritium breeding ratio, space on the back side of the canister was saved by using the coolant supply tubes as the back wall of the canisters (see Figure 43)..

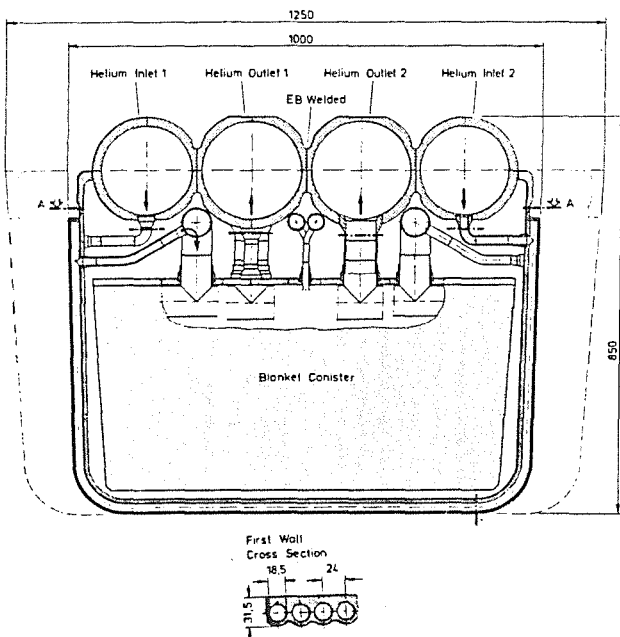


Fig 43: Cross section of DEMO outboard Blanket Segment

At the same time the bolts fixing the canisters to the back wall were strengthened to withstand the electro-magnetic forces during disruptions.

Characteristic for DEMO is an increased wall load ( $2.2 \text{ MW/m}^2$  instead of  $1 \text{ MW/m}^2$ ) and longer operation time than in NET but with the same toroidal field coil dimensions and similar plasma geometry. This makes inboard shielding a critical issue. Therefore a careful optimization of shield and blanket was performed, leading to a thickness of 200 mm for the beryllium/breeder region of the inboard blanket.

The electro-magnetic forces and stresses on the NET box were calculated with a 3d version of the CARIDDI code coupled with ABAQUS. The maximum stresses exceeded the ASME design limits. This holds also for dynamic loads including the damping effect of eddy currents in a magnetic field. To reduce these stresses the boxes should be fixed at the lower end and

the copper saddle loop has to be electrically insulated from the box.

For the NET test module 3d thermohydraulic calculations were performed on the temperature distribution inside the canister. Fig. 44 shows an isomeric view of one substructure in the calculations.

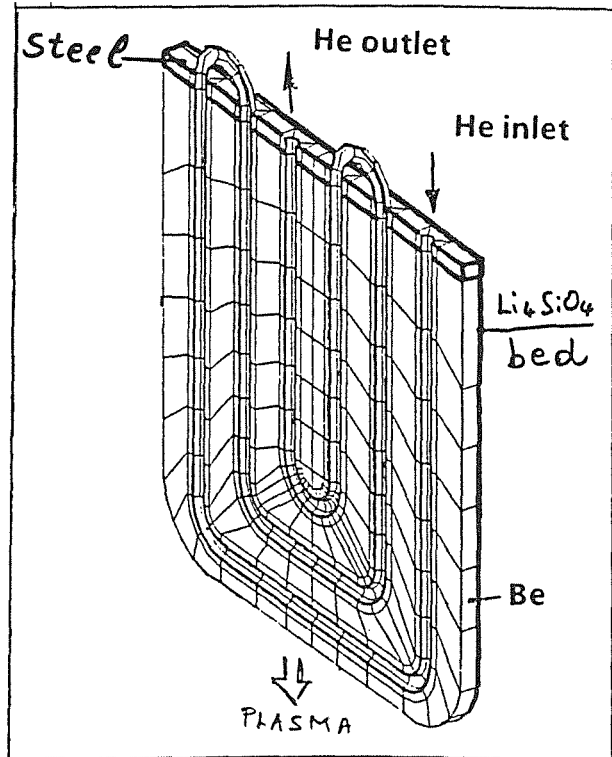


Fig. 44: One slab of the canister blanket concept consisting of ceramic pebble bed layer, beryllium plate and coolant coil

Next to this follows a similar structure but with the helium inlet and outlet connections reversed (180 degree rotation of Fig. 44). This has the effect that the minimum temperature in  $\text{Li}_4\text{SiO}_4$  is much higher than it would be with equally arranged coolant systems. In Fig. 45 the poloidal distribution of the temperature in the pebble bed, beryllium, and steel is shown for the NET blanket (21 canisters). The higher  $\text{Li}_4\text{SiO}_4$  temperature leads to a significantly smaller tritium inventory when compared with the values obtained from 2d-calculations and reported in Ref. 1 (6g tritium instead of 400 g).

For the NET-test-object, 5 canisters in a port position, the tritium extraction system was specified. It consists essentially of a cooler, a room temperature water adsorber for  $\text{H}_2\text{O}$  and HTO removal, a silver palladium permeation filter to extract the  $\text{H}_2/\text{HT}$  mixture and a cold trap to extract the heavier gas impurities from the helium purge gas. For DEMO a different system operating at high temperature is foreseen.

Staff:

L. Boccaccini  
E. Bojarsky  
M. Dalle Donne  
U. Fischer  
M. Kühle  
P. Norajitra  
G. Reimann  
H. Reiser  
G. Sordon

Reference:

1. M. Dalle Donne et al.  
Pebble-Bed Canister: The Karlsruhe Ceramic Breeder  
Blanket Design for the Next European Torus Fus. Techn.  
Vol. 14 (1989) 1357.

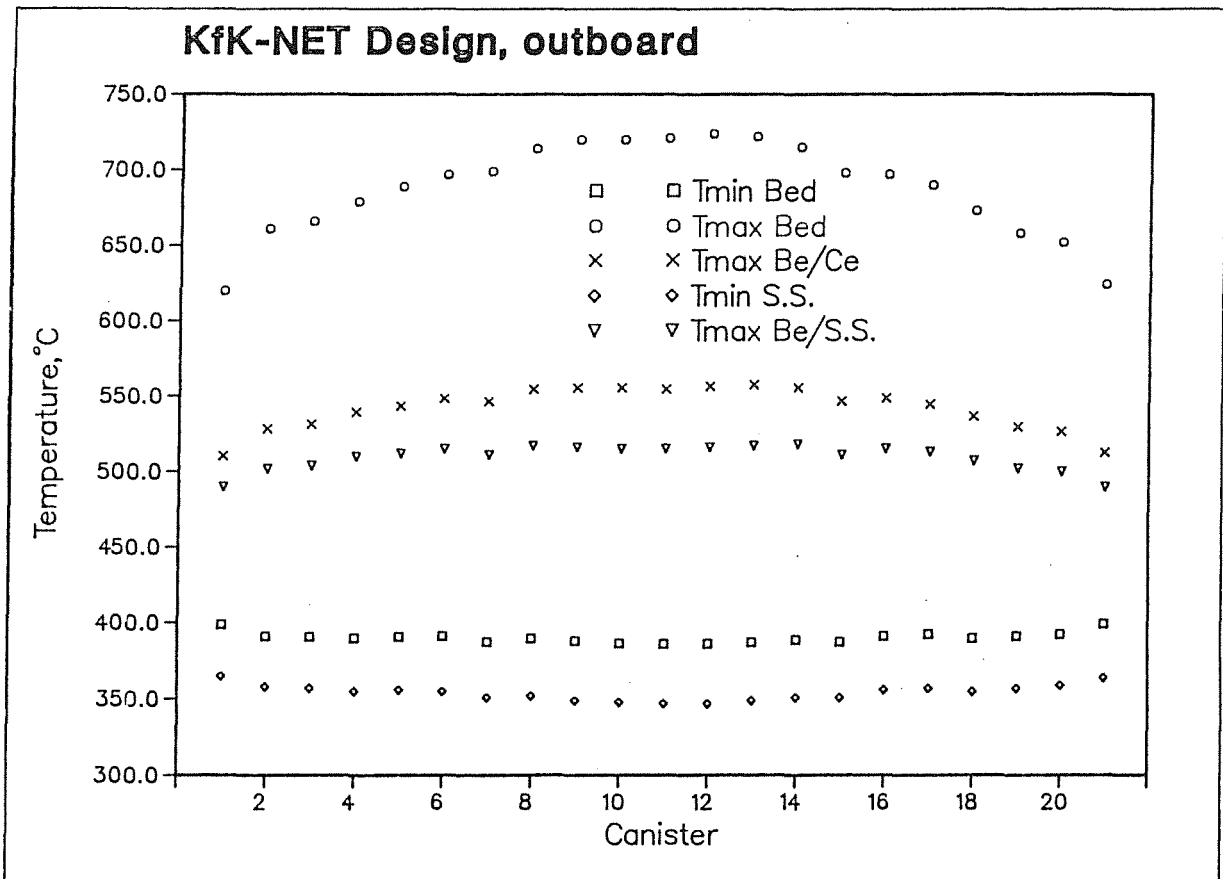


Fig 45: Solid Breeder Test Blanket  
poloidal temperature distribution

## **BS BR-D-1      Preparation of Ceramic Breeder Materials**

The preparation and characterization of lithium containing monosilicates, especially  $\text{Li}_4\text{SiO}_4$ , and lithium metazirconate,  $\text{Li}_2\text{ZrO}_3$ , are under development to be used as breeder materials within the European Fusion Program. The development was concentrated on the optimization of lithium orthosilicate pebbles concerning the density and the shape of the granules.

A tap-density of at least  $1.3 \text{ g/cm}^3$  for the  $\text{Li}_4\text{SiO}_4$  pebble-bed, as foreseen for the KfK blanket concept, has been achieved with the sintered granules by optimization of the homogeneity of the mixture of  $\text{Li}_4\text{SiO}_4$  powder and binding additives as well as the sintering process in fluidized beds. A second step of rounding the granules on a rotating disk leads to a more spherical shape of the pebbles, which was shown to have a significant influence on the final tap-density of the pebble bed.

First results have been achieved with the preparation of lithium metazirconate pebbles. The granules were prepared by the same method as used for the preparation of the  $\text{Li}_4\text{SiO}_4$  pebbles. Work is continued to obtain dense granules with spherical shape to meet the specification of the KfK blanket concept.

### Publications:

D. Vollath, H. Wedemeyer:

The Use of Solid Solutions of the System Lithium Orthosilicate - Eucryptite as Breeder Material, 91st Annual Meeting and Exposition of the American Ceramic Society, Indianapolis, USA 1989

### Staff:

B. Dörzapf

E. Günther

J. Heger

D. Vollath

H. Wedemeyer

M. Wittmann

**BS BR-D-2 Characterization**

COMPLIMENT, an irradiation experiment with different Lithium ceramics, which are tentative breeder materials for a fusion reactor blanket, was performed in parallel in the HFR-reactor in Petten/Netherlands and in the OSIRIS-reactor in Saclay/France. The objectives of this irradiation are (1) to compare the radiation damage in a single lithium ceramic compound caused by fast neutron scattering with the damage caused by the  $\alpha$ - and T-particles out of the  $\text{Li-6}(n, \alpha) \text{T}$ -reaction, and (2) to compare the radiation damage and the irradiation behaviour of various lithium ceramics in an identical test environment.

Samples for this irradiation test were supplied by 5 partners, CEA, ENEA, CEN Mol, UKAEA and KfK.

The following materials were supplied by KfK:

- $\text{Li}_2\text{O}_3$  pellets
- $\text{Li}_4\text{SiO}_4$  pellets
- $\text{Li}_4\text{SiO}_4$  sintered spheres
- $\text{Li}_4\text{SiO}_4$  molten spheres.

For the characterization the following methods were applied:

- Chemical and isotopic analysis for composition
- Geometry of the pellets and spheres
- Mercury intrusion porosimetry
- Helium pycnometry
- Specific surface determination
- Ceramography.

The analysis of the composition using atomic adsorption spectroscopy, gravimetry, and mass spectrometry showed a minor deviation from stoichiometry and an impurity level below about 10 ppm for most impurities with exception of Fe and Si. The geometric and structure data of the 4 species are compiled in table 1. The He-pycnometer density is nearly identical with the theoretical density. This leads to the conclusion, that there is almost only open porosity. The density values, measured by He-pycnometry, which show a higher than the theoretical density for the  $\text{Li}_4\text{SiO}_4$ -specimens indicate, that there are either impurities in the material or a notable amount of  $\text{Li}_2\text{SiO}_3$  (e.g.  $\sim 10\%$ ). In contrary to the high mean bulk density of 91.1 % th.d. for the  $\text{Li}_2\text{SiO}_3$ -pellets and 87.5 % th.d. for the  $\text{Li}_4\text{SiO}_4$ -pellets, the corresponding values for the tap density of a pebble bed are much lower. They are 50.6 % th.d. for the  $\text{Li}_4\text{SiO}_4$  sintered spheres and 56.9 % th.d. for the molten spheres.

Table 7 also contains the porosity data, the specific surface area and the grain size.

Table 7: Geometric and structure data of the KfK lithium silicate specimens

	$\text{Li}_2\text{SiO}_3$ pellets	$\text{Li}_4\text{SiO}_4$ pellets	$\text{Li}_4\text{SiO}_4$ sintered granulates	$\text{Li}_4\text{SiO}_4$ molten spheres
Mean diameter (mm)	4.51	4.97	0.5	0.5
Specimen density by Hg- porosimetry ( $\text{g}/\text{cm}^3$ ) (% th.d.)	2.37 93.7	2.15 90.0	2.19 90.8 <sup>1)</sup>	2.23 92.9 <sup>1)</sup>
Total porosity (%)	6.3	10.0	9.2	7.1
Matrix density by He- pycnometry ( $\text{g}/\text{cm}^3$ ) (% th.d.)	2.51 99.2	2.38 99.6	2.41 <sup>2)</sup> $\sim 100$	2.40 <sup>2)</sup> $\sim 100$
Closed porosity (%)	0.8	0.4	$\sim 0$	$\sim 0$
Open porosity (%)	5.5	9.6	$\sim 9$	$\sim 7$
Specific surface area ( $\text{m}^2/\text{g}$ )	0.67	1.54	2.1	5.9
Mean diameter of cross sections through grains ( $\mu\text{m}$ )	19	45	36	19

Remark<sup>1)</sup> Referred to He-pycnometer density

Remark<sup>2)</sup> These high values may be caused by impurities or by about 10 %  $\text{Li}_2\text{SiO}_3$

Theoretical density  
of  $\text{Li}_2\text{SiO}_3$ :  $2.53 \text{ g}/\text{cm}^3$   
of  $\text{Li}_4\text{SiO}_4$ :  $2.39 \text{ g}/\text{cm}^3$

Staff:

- H. Elbel
- R. Hanselmann
- W. Laub
- H.-J. Ritzhaupt-Kleissl
- R. Scherwinsky
- D. Vollath

### BS BR-D-3 Irradiation Testing

The first irradiation experiments, DELICE 01 and 02, involving encapsulated KfK specimens, were performed in the OSIRIS reactor, Saclay, as early as in 1985/86. In the framework of an international comparative irradiation campaign with breeder ceramic specimens, termed COMPLIMENT (Comparison of Lithium Materials Damage Effects by Fast Neutrons and  $6\text{Li}(n,\alpha)\text{T}$ -Reactions) two further irradiations of 36 encapsulated specimen stacks each have been completed meanwhile. For the DELICE 03 in-pile experiment performed in the thermal flux of the OSIRIS reactor, terminated after 77 FPD in February 1989, a modified COLIBRI test rig was used (Fig. 46). This is a double-walled capsule type test rig accom-

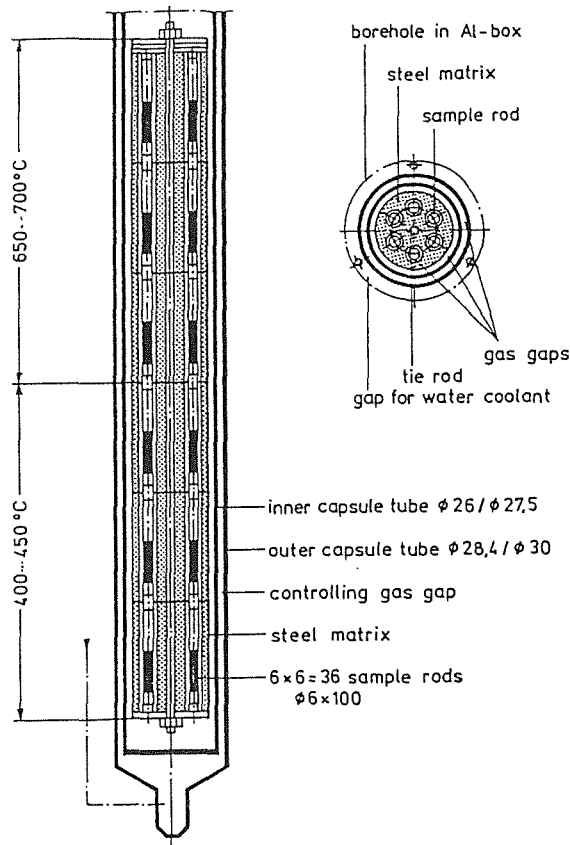


Fig. 46: DELICE 03 irradiation capsule with breeding ceramic materials in the OSIRIS reactor

modating at six levels six specimen rods each in a steel matrix. Half of the specimens were kept at 400-450 °C and at 650-700 °C, respectively. The temperatures are adjusted via gas gaps and controlled by means of a gas mixture provided in the controlling gap between the inner and outer containments.

The corresponding experiment, ELIMA 2, conducted in the fast flux (behind a cadmium screen) of the HF-reactor in Petten was terminated in January 1989 after 178 FPD. Figure 47 shows the irradiation rig used in that experiment. The 36 specimen rods are arranged at four levels in that experiment. The temperature can likewise be controlled via gas gap with the possibility of providing in addition axial com-

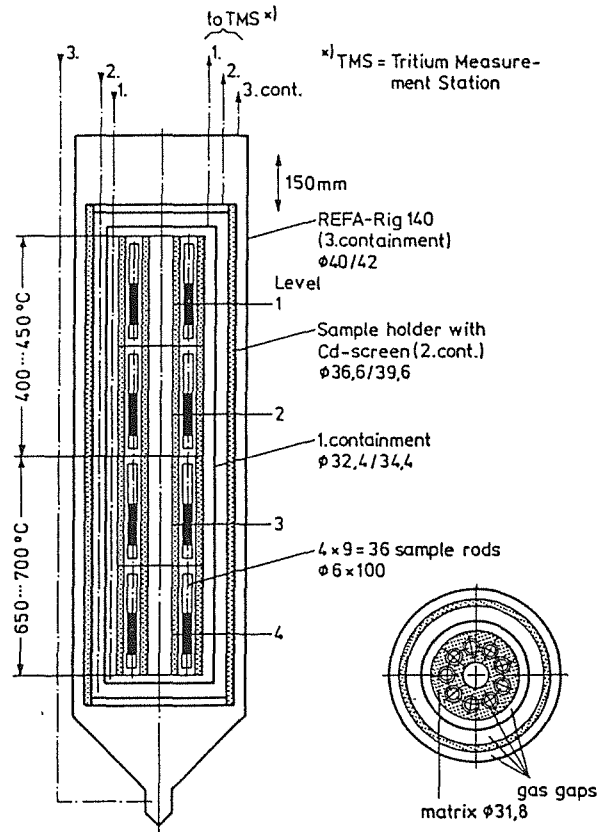


Fig. 47: ELIMA 2 irradiation capsule with breeding ceramic materials behind a cadmium screen in the HFR/Petten

penation of changes in the position in the maximum of neutron flux by means of a shifting mechanism.

For the COMPLIMENT comparative irradiation specimen material was provided by CEA/Saclay, ENEA/Cassacia, UKAEA/Springfield, CEN/Mol and KfK and encapsulated under identical conditions at the KfK Institute for Materials and Solid State Research (IMF III) which is also responsible for coordinating the experiment as a whole. Specimen loading for the two experiments ELIMA 2 and DELICE 03 was already described on pages 14/15 of the Semi-annual Report KfK 4339/EUR 10539e.

Disassembly of the two irradiation rigs after irradiation at Petten and Saclay, respectively, has already been performed. The 2x36 specimen rods will be returned in the 4<sup>th</sup> quarter of 1989 for post-irradiation examinations in Karlsruhe.

LISA 1 and 2 were the first "purged KfK in-pile experiments" with continuous measurement of tritium release, carried out as early as in 1985 until 1987. The first joint German-French irradiation experiment, LILA/LISA, involving a direct comparison of specimens of both partners started in Grenoble in spring 1989. The irradiation is performed in a CHOUCA rig in the SILOE reactor with three specimen stacks each arranged at two levels (Fig. 48). The joint experiment related to three pellet stacks each (8 mm dia. x 80 mm) of CEA and KfK. CEA has provided lithium aluminate and KfK three breeder

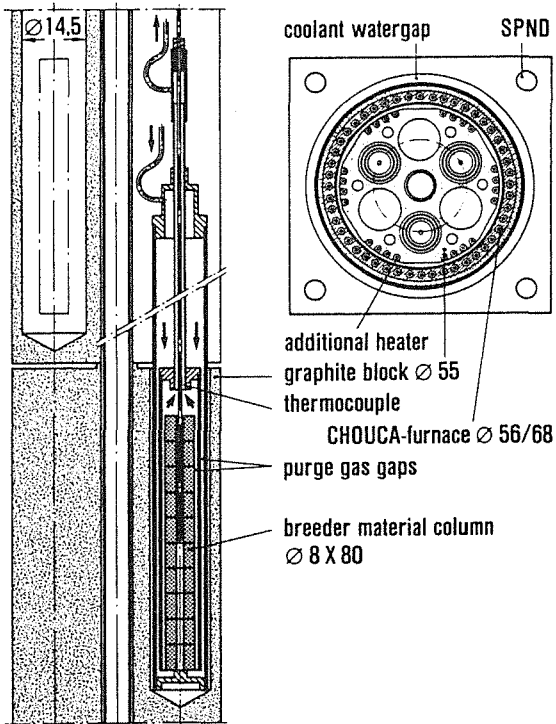


Fig. 48: Purged breeder material capsule with CHOUCA furnace in the SILOE reactor.

material variants, namely lithium orthosilicate, aluminum doped lithium orthosilicate and lithium metasilicate. Specimen temperatures of about 400-700 °C can be reached. The actual values can be adjusted by a gas gap and controlled by electrical heating. (Results obtained: see chapter tritium release.)

Staff:

H.E. Häfner  
K. Heckert  
K.D. Philipp

## BS BR-D-4 Tritium Release

In assessing the performance of ceramic breeders, tritium release is an important aspect. KfK concentrates on lithium silicates, especially orthosilicate, and metazirconate. In pile-tests (LISA) and out-of-pile annealing experiments are performed.

Two cycles of the first common CEA/KfK in-pile-test LILA/LISA-3 have been performed, one further is envisaged. Metazirconate samples of CEA, Mol and KfK and, in addition, pure and Al-doped orthosilicate of KfK have been tested. The main goal of the first cycle (June 23 - July 7, 1989) was to compare the release behavior for the reference purge gas He + 0.1 vol% H<sub>2</sub> in the temperature range 300-500°C. The main results are:

- 1) At lower temperatures (< 400°C) the residence times of the CEA and Mol metazirconate samples (grain size 1 μ) are more than one order of magnitude smaller than those of the KfK metazirconate (grain size several ten μ). This provided one criteria for the selection of metazirconate samples for in-pile test SIBELIUS (ceramic-Be interaction). The difference is attributed to the different grain size.
- 2) From the KfK samples, the metazirconate and the doped orthosilicate (Li<sub>3,7</sub>Al<sub>0,1</sub>SiO<sub>4</sub>) are slightly faster than the pure orthosilicate.

In the second cycle (July 18-August 11, 1989) it was tried to check the dependence of inventory on tritium production rate. This should provide information on the order of the release controlling process. In addition, release behavior with He + 100 vpm H<sub>2</sub>O was tested. The main results are:

- 1) The inventory changes for 500 → 400 and 500 → 450°C are (within the pretty large experimental error) proportional to the production rate. This indicates that the release controlling process is first order.
- 2) For all samples (metazirconate, pure and doped orthosilicate) the residence times with He + 100 vpm H<sub>2</sub>O are several times larger than with He + 0.1 Vol% H<sub>2</sub>. This is surprising, because out-of-pile experiments indicated a remarkable acceleration of tritium release with H<sub>2</sub>O addition in the range below several ten vpm.

The PIE tritium release measurements of DELICE01 have been finished. In DELICE01 clad and unclad metasilicate pellets (65 and 85% TD) were irradiated at 500 and 700°C for 26 full power days (fluence 7 · 10<sup>19</sup> 1/cm<sup>2</sup>) in the OSIRIS reactor at Saclay. Some results for the unclad samples (atmosphere stagnant He) are given in the Table 8.

Residence times (release / production rate) are for 85% TD a factor 2 to 3 larger than for 65% TD material and about two orders of magnitude larger than for orthosilicate.

Pellet 3 of sample 38 (F\*4) (85% TD, irradiation temperature 710°C) was heated in four successive runs with 5°C / min to increasing final temperatures. The measured release as a function of time is compared in Fig.49 with calculations taking into account diffusion in the grain and one first and one second order desorption process at the grain surface. To achieve satisfactory agreement, it was necessary to assume that the activation energy of the second order process increases with decreasing inventory. The main conclusion from this comparison is, that the release is controlled by a (first or second order) desorption process at the grain surface and that the activation energy of the controlling process increases with time (i.e. decreasing inventory).

DELICE01, unclad metasilicate pellets

				Irradiation		
TD	Sample	Av. mass/ pellet (g)	Av. release/ pellet (mC)	T(°C)	Prod. rate/ pellet (mC/h)	Residence time (h)
65%	41 (F*6) pellet 4,5	0.180	4.29	710	1.12	3.8
	41 (G*1) pellet 1	0.179	327	500	1.40	234
85%	38 (F*4) pellet 1-7	0.221	17.9	710	1.30	13.8
	38 (G*4) pellet 1	0.208	557	500	1.51	369

Table 8: Comparison of measured and calculated release for DELICE01 unclad metasilicate (85% TD, irradiation temperature 710°C). Sample heated in four successive runs with 5°C/min to increasing final temperatures. Purge gas He + 0.1 vol/H<sub>2</sub>.

Publications:

W. Breitung, M. Brieu, H. Werle; Fusion Eng. Design 8 (1989)  
323

Staff:

W. Breitung  
T. Eberle  
J. Lebkücher  
M. Mösche  
H. Werle

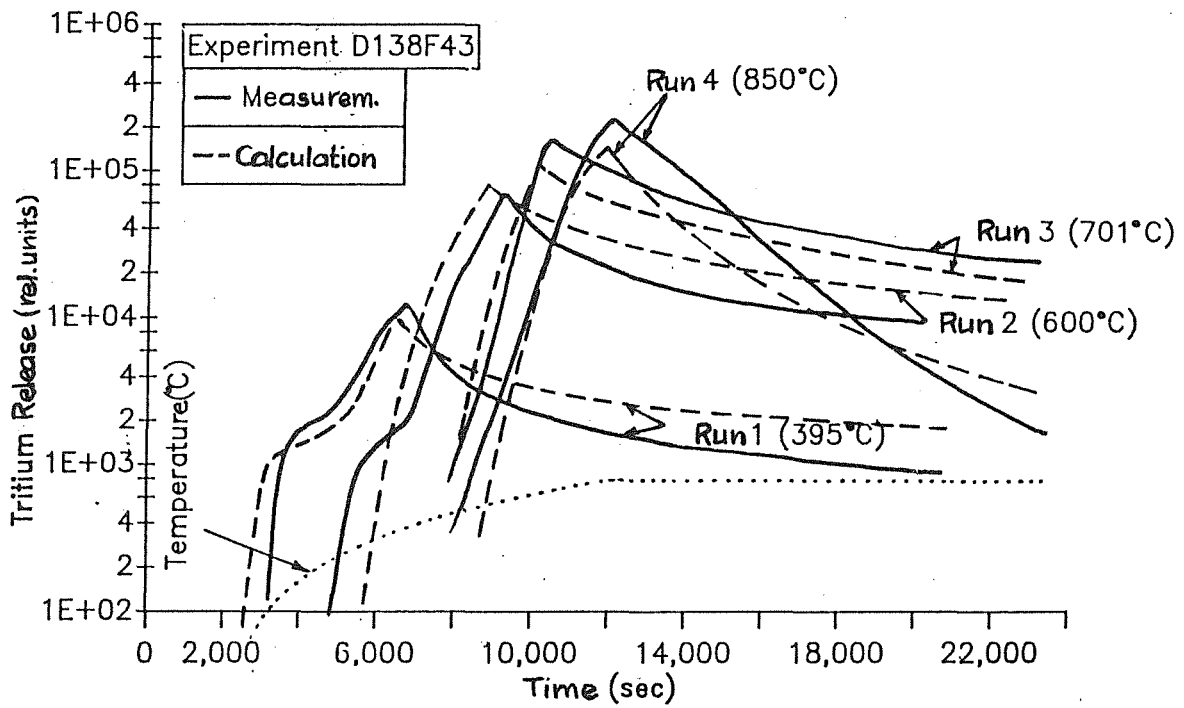


Fig. 49: Delice-1, Li<sub>2</sub>SiO<sub>3</sub> (85 % TD, irradi. temp. 710°C), comparison of measured and calculated release



## BS BR-D-5 Physical and Mechanical Properties

The determination of the thermal conductivity of  $\text{Li}_4\text{SiO}_4$  as a characteristic property of this compound was very difficult. Fig. 50 gives the state of the art at the begin of 1989. From

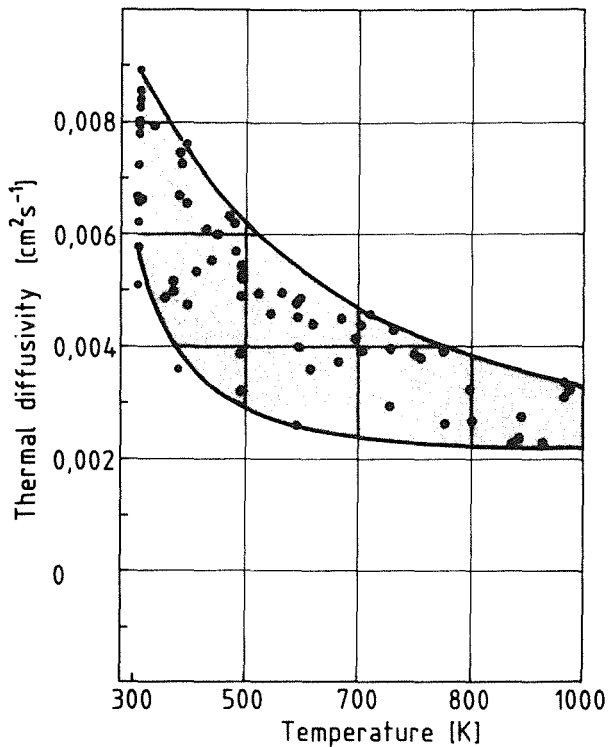


Fig. 50 : Thermal diffusivity of  $\text{Li}_4\text{SiO}_4$ .

this it followed that a detailed characterization of the two KfK-materials ( $\text{Li}_4\text{SiO}_4$ -INR and  $\text{Li}_4\text{SiO}_4$ -Elima) was absolutely necessary. We got the following results:

1. In DTA measurements on Elima samples the ( $\text{Li}_4\text{SiO}_4$ - $\text{Li}_2\text{SiO}_3$ ) eutectic peak at 1022 °C appeared during first heating up. This was not the case for INR samples.
2. Ceramographic investigations show the eutectic to be the matrix, in which  $\text{Li}_4\text{SiO}_4$  grains are dispersed (Fig. 51).
3. From calorimetric measurements it results that  $\text{Li}_4\text{SiO}_4$  in general absorbs  $\text{H}_2\text{O}$ . This can only be avoided if the samples are stored in vacuum in presence of  $\text{P}_2\text{O}_5$ .

Observing especially point 3 and measuring the thermal diffusivity in Ar ( $\sim 500$  mbar) for both kinds of  $\text{Li}_4\text{SiO}_4$ , reproducible data without any hysteresis could be generated.

The results are shown in Fig 52. The lower curve represents the thermal conductivity of  $\text{Li}_4\text{SiO}_4$  (100 % density), whereas the upper curve is the thermal conductivity of  $\text{Li}_2\text{SiO}_3$  (100 % density). As it must be, the thermal conductivity of the Elima material is higher than that of the pure  $\text{Li}_4\text{SiO}_4$  and lower

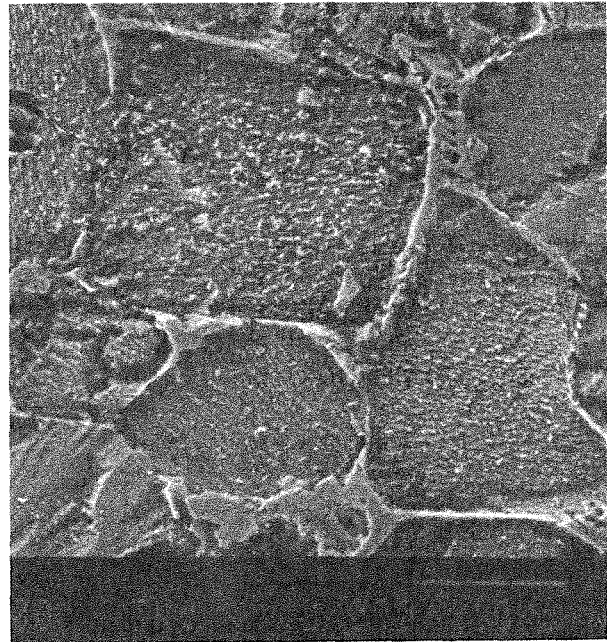


Fig. 51: Microstructure of  $\text{Li}_4\text{SiO}_4$ - $\text{Li}_2\text{SiO}_3$ .

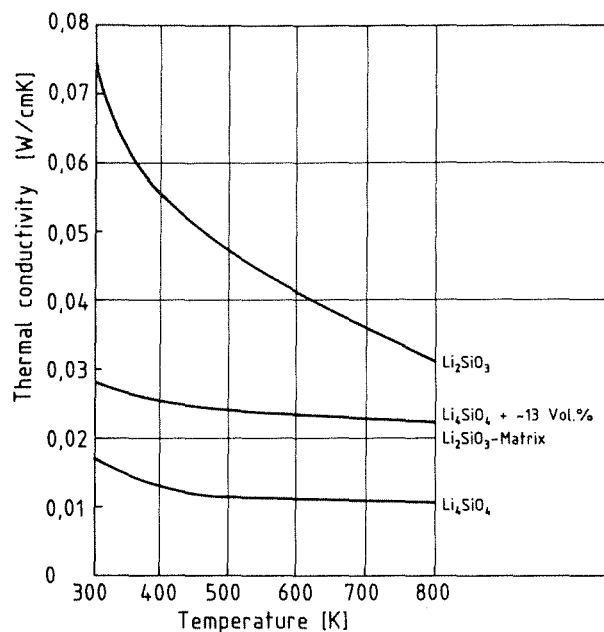


Fig. 52: Thermal conductivity of  $\text{Li}_2\text{SiO}_3$ ,  $\text{Li}_4\text{SiO}_4$  and  $\text{Li}_4\text{SiO}_4$ - $\text{Li}_2\text{SiO}_3$ .

than that of  $\text{Li}_2\text{SiO}_3$ . It is important to note that the eutectic forms the matrix, with an estimated volume content (quantitative image analysis) of  $\text{Li}_2\text{SiO}_3$  of  $\sim 13$  %.

Staff:  
G. Haase  
B. Schulz  
K. Spieler

## BS BR-D-6 Compatibility

In order to investigate chemical interactions of Li-silicates with stainless steel at defined  $H_2O$  partial pressures annealing experiments in a flowing gas atmosphere with a constant  $H_2O$  partial pressure of 10 Pa (100 vpm) and 100 Pa (1000 vpm) have been performed at 700 and 800 °C. The gas flow was about 25 l Ar/h. A sheet of AISI 316 stainless steel was embedded in  $Li_4SiO_4$  or  $Li_2SiO_3$  pellets each. The preparation was performed in a glove box under inert gas conditions. The Li-silicate powders were dried at 900 °C for 2 h.

First results obtained at 800 °C are shown in Fig. 53. It

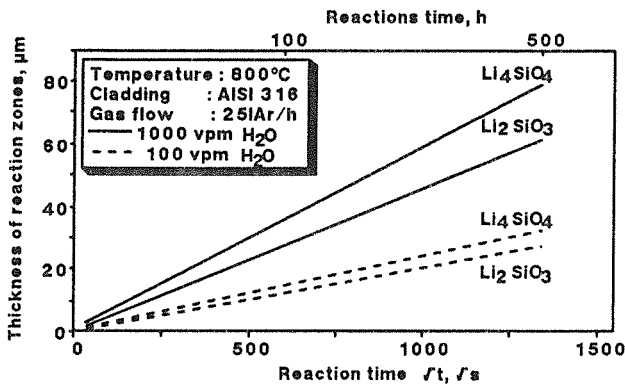


Fig. 53: Chemical interactions between Li-based oxide ceramics and stainless steel AISI 316 in dependence on  $H_2O$  partial pressure.

depicts the different reaction of  $Li_4SiO_4$  compared to  $Li_2SiO_3$  and the strong influence of moisture on the extent of the chemical interactions between the Li-silicates and stainless steel. The maximum reaction zone depths after 500 h at 800 °C were for  $Li_4SiO_4$ : 80/30 µm and for  $Li_2SiO_3$ : 60/26 µm for  $H_2O$  partial pressures of 100 and 10 Pa, respectively. Similar results were obtained at 700 °C, but with smaller reaction zones. In further experiments  $Li_2O$  will be considered in addition for comparison reasons.

### Staff:

J. Burbach

P. Hofmann

H. Metzger

## BS BR-D-7 Constitution, Interaction with Water Vapour

The investigation of the  $\text{Li}_2\text{O}-\text{ZrO}_2$  phase relations was continued and has been nearly completed. The results lead to a phase diagram with the following main features: Three intermediate stable compounds exist between  $\text{Li}_2\text{O}$  and  $\text{ZrO}_2$ . The compound with the highest  $\text{Li}_2\text{O}$  content,  $\text{Li}_8\text{ZrO}_6$ , melts congruently at 1345 °C and undergoes a higher order phase transformation at 420 °C which is detected by differential thermal analysis only, whereas high temperature X-ray diffraction does not give any indications of a change of the crystal symmetry or of the lattice parameters.  $\text{Li}_6\text{Zr}_2\text{O}_7$  melts incongruently at 1400 °C (peritectic), decomposing into  $\text{Li}_2\text{ZrO}_3$  and melt.  $\text{Li}_2\text{ZrO}_3$  melts congruently at 1690 °C. Three eutectics were observed in the system:

1. at 1100 °C between  $\text{Li}_2\text{O}$  and  $\text{Li}_8\text{ZrO}_6$ ,
2. at 1290 °C between  $\text{Li}_8\text{ZrO}_6$  and  $\text{Li}_6\text{Zr}_2\text{O}_7$ , and
3. at 1640 °C between  $\text{Li}_2\text{ZrO}_3$  and  $\text{ZrO}_2$ .

The phase transformations of  $\text{ZrO}_2$  (monoclinic  $\rightarrow$  tetragonal and tetragonal  $\rightarrow$  cubic) in the two-phase fields  $\text{Li}_2\text{ZrO}_3 + \text{ZrO}_2$  occur at 1190 °C and probably 1450 °C, respectively.

The investigations of the interaction with water vapour were extended to lithium orthosilicate ( $\text{Li}_4\text{SiO}_4$ ) spheres fabricated by Schott/Mainz and to Lithium metazirconate ( $\text{Li}_2\text{ZrO}_3$ ) powder of our own production.

$\text{Li}_4\text{SiO}_4$  spheres: This material has a content of 3 weight-%  $\text{Li}_2\text{SiO}_3$  for reasons of mechanical stability. It was loaded with water vapour isothermally at different temperatures (250, 300, 350 and 500 °C) under 1 mbar  $\text{H}_2\text{O}$  partial pressure ( $\approx$  1000 ppm  $\text{H}_2\text{O}$ ) for 65 hours and then cooled down to room temperature. The release of  $\text{H}_2\text{O}$  was measured by thermal gravimetry and  $\text{H}_2\text{O}$  analysis in a transient test (5 K/min) up to 850 °C under cover gas ( $\infty$  1 ppm  $\text{H}_2\text{O}$ ). It occurs in a single step with maximum release at  $\sim$  450 °C. The  $\text{H}_2\text{O}$  uptake measured is in the region between 0.015 and 0.09 weight-%.

$\text{Li}_2\text{ZrO}_3$  powder: This material was synthesized by solid state reaction from  $\text{Li}_2\text{CO}_3$  and  $\text{ZrO}_2$  and carefully dried (850 °C/5 hours). The loading with water vapour and the  $\text{H}_2\text{O}$  release tests were conducted in the same way as mentioned above for  $\text{Li}_4\text{SiO}_4$ . For  $\text{Li}_2\text{ZrO}_3$  powder, the  $\text{H}_2\text{O}$  uptake measured is rather low (0.001 - 0.005 weight-%).

### Staff:

V. Schauer  
G. Schlickeiser  
A. Skokan  
H. Strömann

**BS BR-D-8 Thermomechanical  
Characterization**

Several mass spectrometric studies have recently been published on the thermochemistry of lithium orthosilicate, which exhibit significant differences in their results. The discrepancies are at least partly caused by the chemical reactivity of  $\text{Li}_4\text{SiO}_4$  with air components ( $\text{H}_2\text{O}$  and  $\text{CO}_2$ ), which already at room temperature lead to the formation of stable products. These products tend to promote reactions with metals, e. g. even with platinum, a material often used to contain lithium ceramics in high temperature investigations, and disturb chemical equilibria. As a result variations in the Gibbs free energies and the enthalpy differences of the thermal decomposition reactions will occur.

In the present work two types of lithium orthosilicate pebbles were examined with respect to possible differences in reaction enthalpies. Samples of type A were prepared by a powder

metallurgical method. Type B samples were obtained at Schott Glaswerke, Mainz, F. R. G. by melting followed by spraying of the melt.

For the comparative study of the thermochemical properties of the two types of  $\text{Li}_4\text{SiO}_4$  the Knudsen effusion mass spectrometry technique was employed. From equilibrium constants obtained by mass spectrometric measurements of partial pressures as a function of temperature and from Gibbs free energy functions the enthalpy data given in table I were calculated. With the exception of equilibria (3) and (4) the reaction enthalpies found for both types of pebbles agree within the statistical errors given in table 9.

Staff:

H. R. Ihle  
R.-D. Penzhorn  
 P. Schuster

Reaction	$\Delta H^\circ_{298,r}$ (kJ/mol)	
	Type A	Type B
solid $\text{Li}_4\text{SiO}_4$		
$\text{Li}_4\text{SiO}_4(\text{cr}) = 2 \text{Li}(\text{g}) + 0.5 \text{O}_2(\text{g}) + \text{Li}_2\text{SiO}_3(\text{cr})$ (1)	960.70 ± 2.38	957.26 ± 4.06
$\text{Li}_4\text{SiO}_4(\text{cr}) = \text{Li}_2\text{O}(\text{g}) + \text{Li}_2\text{SiO}_3(\text{cr})$ (3)	520.43 ± 2.69	513.43 ± 2.16
$\text{Li}_2\text{O}(\text{g}) = 2 \text{Li}(\text{g}) + 0.5 \text{O}_2(\text{g})$ (5)	440.23 ± 1.44	442.71 ± 1.93
$\text{Li}_2\text{O}(\text{g}) = \text{LiO}(\text{g}) + \text{Li}(\text{g})$ (6)	360.61 ± 0.84	362.63 ± 1.69
liquid $\text{Li}_4\text{SiO}_4$		
$\text{Li}_4\text{SiO}_4(\text{l}) = 2 \text{Li}(\text{g}) + 0.5 \text{O}_2(\text{g}) + \text{Li}_2\text{SiO}_3(\text{l})$ (2)	946.34 ± 0.73	945.63 ± 4.54
$\text{Li}_4\text{SiO}_4(\text{l}) = \text{Li}_2\text{O}(\text{g}) + \text{Li}_2\text{SiO}_3(\text{l})$ (4)	510.87 ± 2.51	503.97 ± 2.78
$\text{Li}_2\text{O}(\text{g}) = 2 \text{Li}(\text{g}) + 0.5 \text{O}_2(\text{g})$ (7)	435.38 ± 2.15	438.13 ± 6.39
$\text{Li}_2\text{O}(\text{g}) = \text{LiO}(\text{g}) + \text{Li}(\text{g})$ (8)	361.91 ± 0.74	361.93 ± 1.84

Table 9: Standard reaction enthalpies

## **BS NN-D-1 Helium Blanket Test Loop**

In addition to the design work the planning of a helium blanket loop (HEBLO) was started and a draft program was prepared for the construction of the loop. The test facility first is to be used for thermomechanical experiments on blanket components. As from 1992, a special test facility will be available in HEBLO. Then, it will be possible to subject canister sections with about eight beryllium plates to long-term thermal cycling tests. Two gas streams are generated with a temperature of 260°C and 460°C, respectively. By reversing the valves, the streams are led through the cooling pipes in the beryllium plates in an alternating manner. The

test facility can also be used for isothermal operation of original NET test canisters. The providing of the special helium circulation compressor required was initiated. Its major technical parameters include an operating pressure of 80 bars, a pressure head of 1.5 bars, and a helium flow rate of 330 g/s.

### Staff:

E. Bojarsky  
M. Dalle Donne  
H. Reiser  
H. Deckers

## BL DE-D-1 Liquid Metal Test Blanket Design

### Neutronics

The power production of a blanket segment and its spatial distribution have been calculated by means of three-dimensional Monte Carlo calculations with the MCNP-code. A realistic torus sector model of the DEMO double null configuration, developed previously from a corresponding model of the NET reactor, has been used for these calculations. 150 000 neutron histories have been followed to assure a sufficient statistical accuracy of the calculated poloidal-radial power distribution.

Based on a fusion power of 2400 MW a total power production of 34.2 MW has been obtained for an outboard blanket segment of 7.5°. The DEMO reactor with 48 blanket segments therefore produces about 1640 MW, without the power produced at the inboard side of the torus (there is a steel reflector), in the vacuum vessel, in the divertors and other reactor components.

Fig. 54 shows a radial-toroidal cross section of the outboard

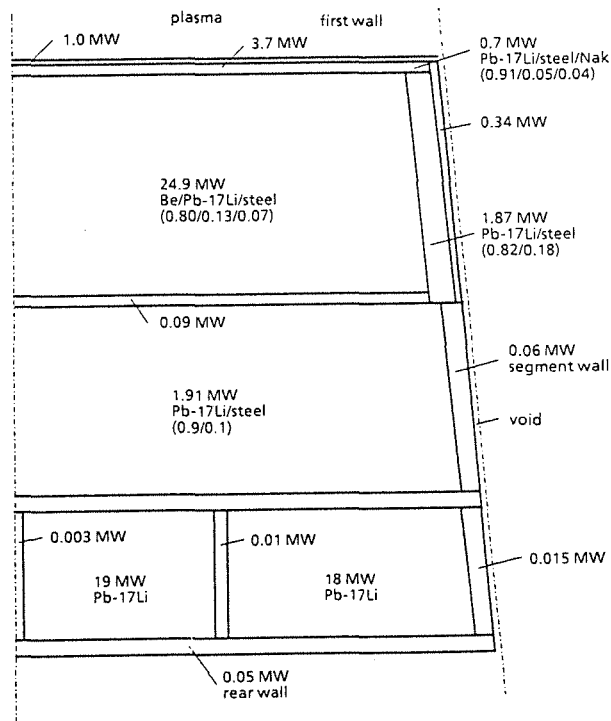


Fig. 54: Radial-toroidal cross-section of the outboard blanket segment in the torus mid-plane along with the calculated power of the blanket segment

blanket segment in the torus mid-plane along with the calculated power in the segment. Note that more than 90 % of the power is produced in the front part - first wall and beryllium zone - of the blanket, whereas the power produced in the large liquid metal channels of the back blanket part nearly is negligible.

### Conceptual design, temperature distribution and stress analysis

The concept of an outboard blanket segment with DEMO specific dimensions, beryllium neutron multiplier and MANET as the structural material was worked out on the basis of earlier designs. Figure 55 shows a section through the

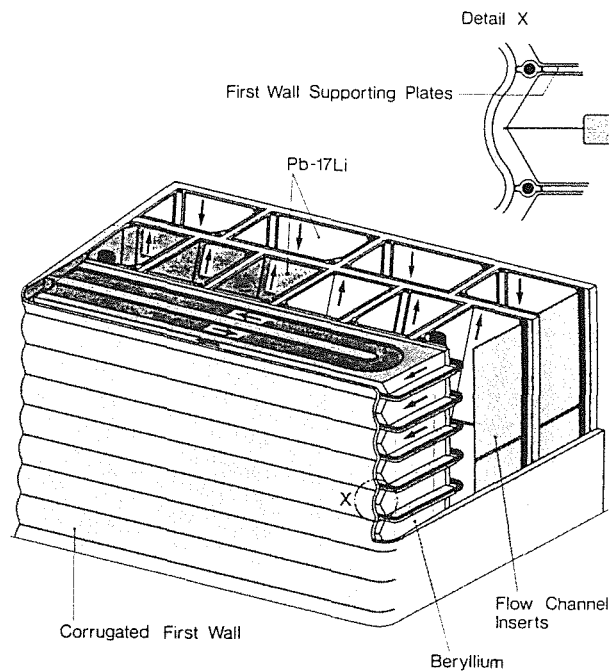


Fig. 55: DEMO-blanket mid-plane

blanket mid-plane. The coolant is supplied in the rear channels. It is subsequently - mainly in toroidal direction - carried through coolant channels running along the first wall and within the beryllium bodies. This type of coolant transport is optimum for cooling the front part of the blanket.

The critical component of the blanket segment is the first wall of about 6 mm wall thickness. It is given a corrugated shape in order to achieve maximum strength and welded with a stiffening sheet between two corrugations each. The numerous partitioning walls produce the effect that the whole front part of the blanket is an inherently stiff body.

For the blanket cross section represented in Fig. 56 temperature and stress computations were made using the ABAQUS finite element code. It was assumed that the flow rates in the coolant channels were the same over the entire cross section in the absence of cross mixing. This means that heat is transported across the flow direction solely by heat conduction. Figure 563 shows by way of example the temperature distribution in the zone of the first wall coolant channel. The computation yielded that mean coolant heating up to 400 °C is possible without any special corrosion problems to be expected.

To be able to evaluate material loading in the blanket structure the primary stresses resulting from a maximum coolant pressure of 50 bar, on the one hand, and the

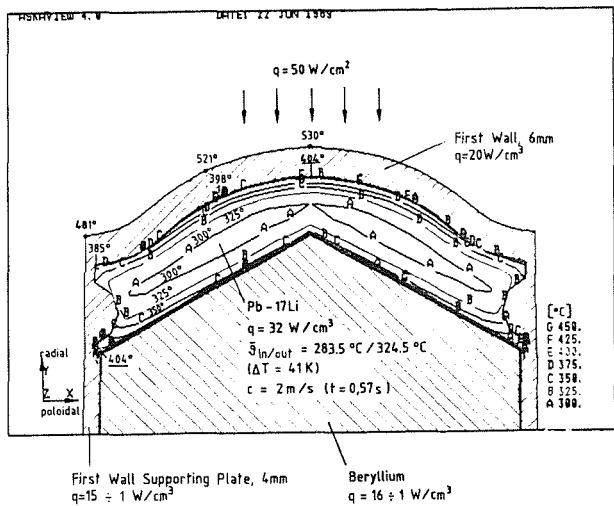


Fig. 56: Temperature distribution in the zone of the first wall coolant channel

temperature induced secondary stresses in combination with the primary stresses, on the other hand, were calculated. The evaluation is based on the ASME pressure vessel code with the von Mises reference stresses used. It was possible to show that the limits of stress prescribed by the ASME code are observed with the MANET material.

MHD-Pressure Loss and Absolute Pressure in Flow Channels

In detail conceptual work on the self-cooled liquid metal blanket segment with DEMO specific dimensions the importance was recognized more clearly of additional MHD pressure losses of unknown amount. The problems involved are all poloidal-radial-toroidal-radial-poloidal 3D-effects associated with the reversals as well as the interactions induced by multichannel effects. As these essential contributions to the total pressure loss will not be amenable to quantification until successful completion of relevant R&D tasks (validation experiments for the MHD theory) a "window" was used for these unknown pressure losses being the difference between a maximum admissible internal pressure and the sum of the MHD pressure losses which can be estimated today.

The maximum admissible internal pressure was estimated at 50 bar for the time being using a 2D-computation and with simplifying assumptions made.

The calculated pressure losses were attributed an uncertainty of ± 20 % (category 1) or + 50 % (category 2). The results of pressure loss calculations are evident from Fig. 57 where the internal pressure has been plotted versus the flow path and the 3D and multichannel effects have not been taken into account. The parameter in Fig. 57 is the level of installation of the circulating pumps because it determines the static portion of the coolant pressure in the blanket. This static portion is of the same order of magnitude as the portion resulting from the MHD pressure losses. The critical point for the mechanical stresses in the blanket segment lies in the zone of the first wall between points B (blanket foot) and C

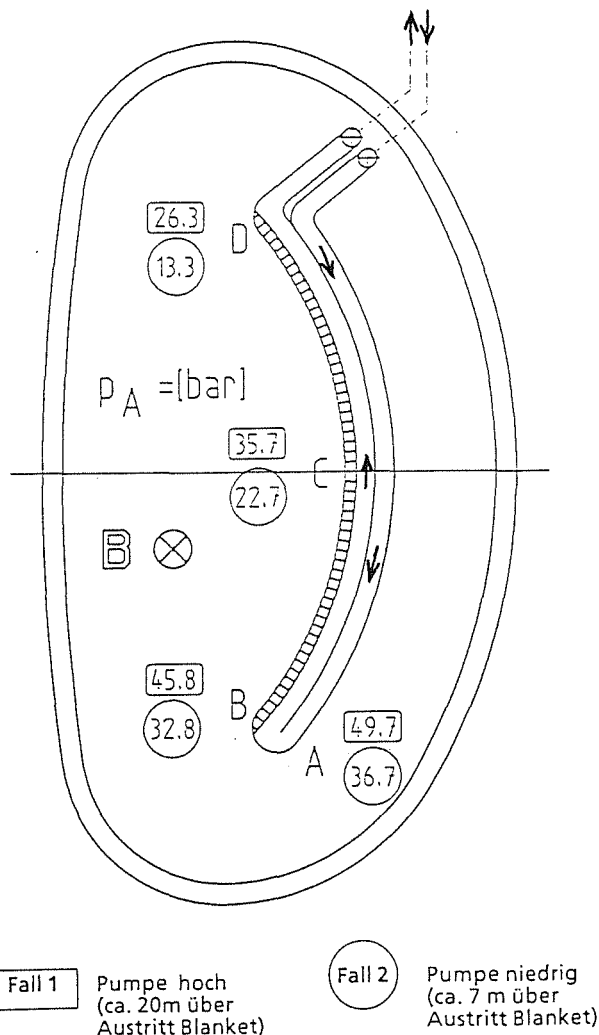


Fig. 57: Pressure distribution in the blanket (without 3D-multichannel effects)

(blanket center). The "window" for the presently still unknown MHD pressure losses resulting from 3D and multichannel effects is obtained under the assumed boundary conditions as a bandwidth from 29 bar (pump low, no safety allowances) to 14 bar (pump high, safety allowances).

The major boundary conditions are:

- steady state operation,
- magnetic flux densities between 4 and 5 T,
- all flow channels equipped with flow channel inserts (except for the first wall),
- wall thicknesses of flow channel inserts for MHD currents ≤ 0.5 mm,
- admissible internal pressure of the flow channels ≤ 50 bar.

The estimate of the MHD pressure losses in a self-cooled outside Pb-17Li blanket of DEMO geometry has been described in detail in an internal report. Problems have been listed which have emerged during these activities. They will have to be discussed, evaluated and tackled, if they turn out to be feasibility questions.

Staff:

K. Arheidt  
V. Casal  
H. Deckers  
U. Fischer  
C. Günther  
H. John  
S. Malang  
R. Möller  
P. Norajitra  
H. Reiser



**BL PC-D-1 Corrosion of Structural Materials in Flowing Pb-17Li**

The test series to evaluate the corrosion of the MANET steel in flowing Pb-17Li at 550 and 500°C were completed. The material losses measured in these tests are shown in Fig. 58. A preceding incubation period was observed at both

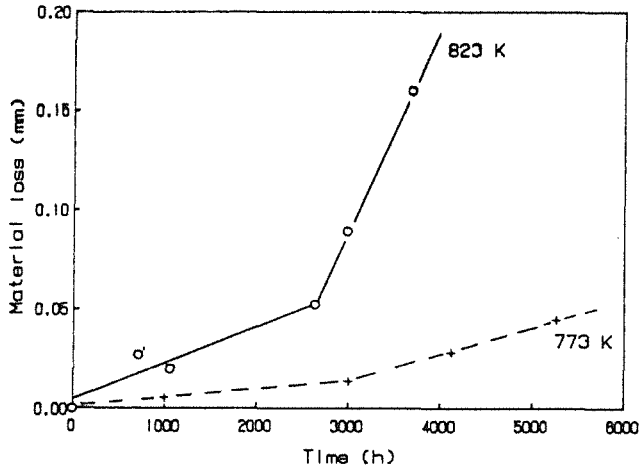


Fig. 58: Material loss in corrosion tests in Picolo as a function of time

temperature levels, the corrosion rates of the linear steady state corrosion are dependent on the temperature, as is shown in the Table 10. The activation energy of the overall reaction is in the order  $\Delta H_{act} \sim 200$  kJ/g-atom. Metallographic examinations showed that internal corrosion effects in the MANET steel did not occur.

Very few specimens of the reference steel AISI 316L (Ispra material) were exposed up to 3000 h at 500°C. The corrosion rate of this material was very close to that of the MANET steel at 50K higher temperature (see Table). Under the conditions in PICOLO, the steel 316L was not internally corroded as described in the literature. The internal ferritic layer is in the order of 0.2 mm and does not contain large amounts of cavities.

Material	Temperature (°C)	Material loss (mm/h)	Weight loss (mg/cm <sup>2</sup> h)
MANET	550	$1.04 \cdot 10^{-4}$	$8.10 \cdot 10^{-2}$
MANET	500	$1.47 \cdot 10^{-5}$	$1.145 \cdot 10^{-2}$
AISI 316L	500	$1.14 \cdot 10^{-4}$	$8.879 \cdot 10^{-2}$

Table 10: Steady State Corrosion in PICOLO

Staff:

- Ch. Adelhelm
- H.U. Borgstedt
- G. Drechsler
- G. Frees
- D. Linder
- Z. Peric
- G. Streib

Publications:

1. H.U. Borgstedt, Chemische Eigenschaften des flüssigen Blanketstoffs Pb-17Li, Bericht KfK 4620, August 1989

**Fatigue of Structural Material in Pb-17Li**

The evaluation of lcf tests with the MANET steel in Pb-17Li indicated a decrease of the strength with increasing number of cycles. The decrease is larger in Pb-17Li at small strain amplitudes, the effect is, however, not significant. The metallographic studies do not show an influence of the liquid metal on the bulk material, some differences are seen in the surface region. The small surface cracks which are formed in the lcf tests in the liquid metal are shorter than in the reference tests and the crack tips are rounded.

Staff:

- H.U. Borgstedt
- M. Grundmann
- Z. Peric
- B. Seith

## BL EX-D-1 Tritium Extraction by Permeation and Cold Trapping

The selected tritium removal technique for the self-cooled Pb-17Li blanket with an intermediate NaK loop consists of tritium permeation into the NaK and precipitation as tritide in a cold trap. For tritium recovery, the cold trap is heated up and the tritium is pumped off.

Presently, the WAWIK test facility for hydrogen (protium) precipitation is in the start-up phase. Figure 59 shows

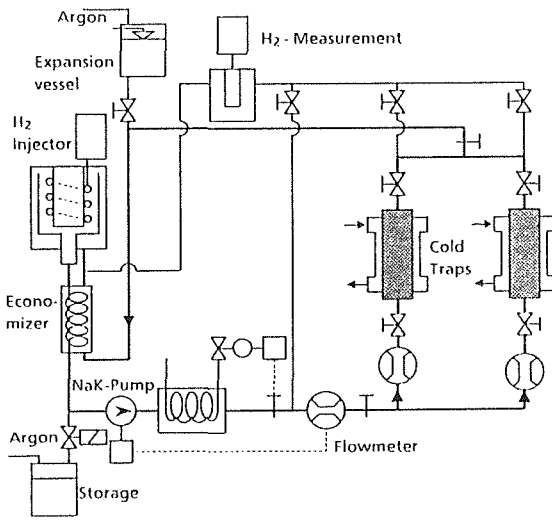


Fig. 59: WAWIK Test Loop for Hydrogen Removal

schematically the set-up: The NaK is pumped by an electro magnetic pump. There are two experimental cold traps in parallel consisting of vertical tubes with a height of 0.6 m and a diameter of 0.1 m which can be equipped with different inserts (wire mesh, rings etc.) Up to 30 thermocouples are installed in one cold trap to measure accurately the temperature distribution.

The hydrogen is injected into the NaK by permeation through a coiled nickel tube 3 mm in diameter, 20 m long and with a 0.3 mm wall thickness. Hydrogen concentrations will be measured upstream and downstream of the cold traps with a hydrogen meter of the nickel membrane diffusion type.

After loading the cold trap with hydrides, the drained cold traps will be transferred to a glove box for analyzing the distributions of the precipitations. Hydrogen recovery by thermal decomposition will be performed by heating up the hydride covered cold trap inserts in that electrically heated vessel which was already used for previous experiments /1/.

The loop was operated with NaK and the different heating and cooling control systems were adjusted. The hydrogen injection system is working well. Presently, the hydrogen concentration measurement system is taken into operation.

Theoretical investigations were performed to determine the temperature, velocity and concentration distribution in mesh-packed cold traps /2/. For characteristic operational conditions mixed convection occurs which influences significantly the velocity distribution and the local deposition rate.

### References:

- /1/ J. Reimann, H. John, S. Malang: Tritium Separation and Recovery from NaK by Cold Traps: Results on Hydrogen Recovery from Na and NaK; Fusion Technology 1988, Elsevier Science Publishers, 1989, p. 1306-1311.
- /2/ L. Bühler, J. Reimann: Mass Transfer at Mixed Convection in Vertical Cylinders; VII Symp. Heat & Mass Transfer, Jadwison, Poland, Oct. 23-26, 1989.

### Staff:

L. Bühler  
R. Kirchner  
D. Rackel  
J. Reimann

## BL EX-D-2 Tritium Extraction by Solid Getters

The loop TRITEX (1) was built for the investigation of the behavior of deuterium in a molten Pb-17Li system. The first experiments with the loop were concerned with measurements of the hydrogen background.

During corrosion of the structural material with (humid) air, H<sub>2</sub> is formed, diffuses through the walls into the LM and is partly released to the different covergas spaces. Typically at 450°C for one of the test sections, 0.02 cm<sup>3</sup>H<sub>2</sub> is released per hour to the covergas; this are about 6.10<sup>-8</sup> mol H<sub>2</sub>/second for one square meter of gas-LM interface. The release rate is different for each part of TRITEX, and nearly constant over a long time. Also, when refilling the loop after several weeks without operation, within a factor of two the same values were obtained. This background is of special interest for the planned experiments, because hydrogen transport rates are expected in the same order of magnitude. Therefore deuterium will be used in the tests.

In parallel to the operation of TRITEX, experiments using thermal convection loops continued (2). Figure 60 shows the

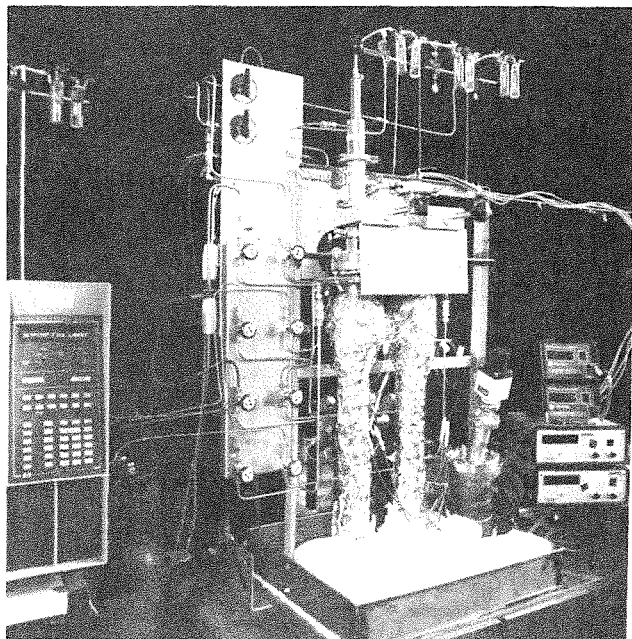


Fig. 60: Thermal Convection Loop THERCOL-4

loop THERCOL-4. Very good results could be obtained (3). The process of dissolution of deuterium in Pb-17Li, and its release rate from a surface, are controlled by diffusion through a liquid metal boundary layer. Transfer rates as well as solubilities of D<sub>2</sub> in the LM could be measured (Fig. 61). The found solubilities are smaller than reported in the literature (4).

Furthermore transport rates for helium and neon could be measured and the solubility of helium in molten Pb-17Li evaluated. The found value of 10<sup>-6</sup> appm/bar at 400°C is extremely low. In many irradiation experiments the

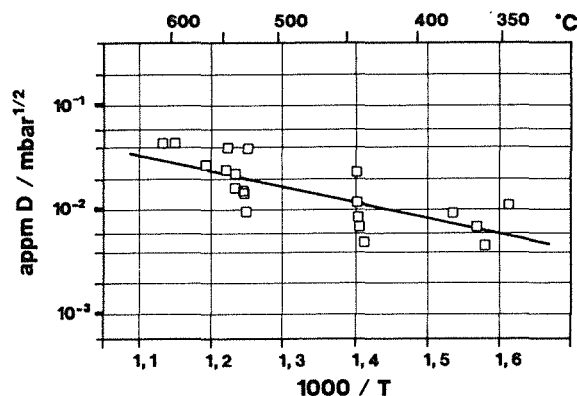


Fig. 61: Solubility of Deuterium in molten Pb-17Li

formation of helium bubbles - even in micro size - may have influenced the tritium release. The experiments with thermal convection loops will continue to study the influence of oxide layers at the LM surface on deuterium transport.

### References:

- [1] H. Feuerstein et. al., J. Nucl. Mat. 155-157 (1988) 520 ICFRM-3, Karlsruhe 1987
- [2] H. Feuerstein et. al., KfK 4418, EUR 10541e (Juli 1988)
- [3] H. Feuerstein et.al., J.Nucl.Mat., to be published, ICFRM-4, Kyoto 1989
- [4] F. Reiter et.al., Proc. 14th SOFT Conf. Avignon 1986

### Staff:

H. Feuerstein  
H. Gräbner  
S. Horn  
J. Beyer  
J. Oschinski  
G. Kieser (DTI)

## BL MH-D-1 Liquid Metal MHD

For the present design of the selfcooled liquid metal blanket, characterized by the poloidal-toroidal flow concept, we re-evaluated the key problems and the state of the knowledge to calculate MHD pressure drop, pressure distributions, velocity and mass flow distributions, and the related heat transfer problems.

To define the priorities of the future test programme the main problem areas of the MHD flow and their importance to validate the feasibility of this concept was worked out. Fig. 62 shows a schematic view of the selfcooled liquid metal blanket and the key problems.

In Table 11 the problems are listed according to the sequence of the liquid metal flow through the blanket, their characteristic features, the direction of the flow with respect

to the magnetic field, an assessment of the problem with respect to the MHD pressure drop and flow distribution, the order of magnitude of the characteristic numbers and a final assessment of their validation. The three evaluation steps are:

- 1 = knowledge not sufficient, but not decisive for the concept
- 2 = Important for the concept
- 3 = Decisive for the feasibility

With respect to the MHD pressure drop it can be concluded from Table 11 that the losses in the poloidal channels and the 3-dimensional effects and the multichannel effects are decisive for the feasibility of the concept. The velocity and flow distribution and therefore the heat transfer from the first wall are dominated by the radial-toroidal bend, the MHD flow in the toroidal channels and by the mass flow distribution. The latter depends on the 3-dimensional effects.

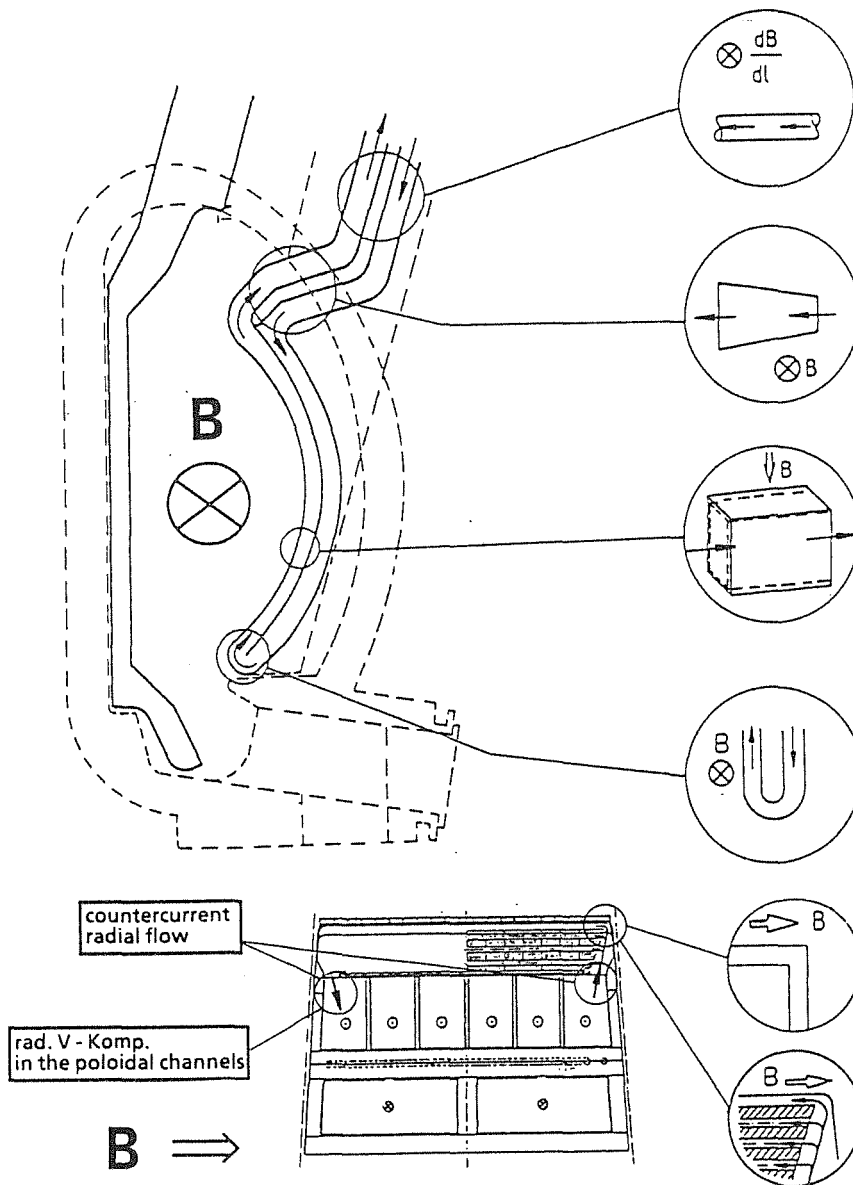
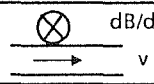

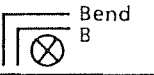
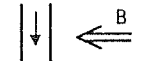


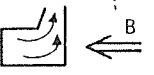

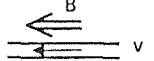
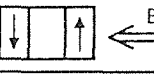


Fig. 62: MHD key problems of a selfcooled liquid metal blanket

Nr.	Problem	Feature	Direction	Evaluation		Scaling Parameters			Experiment				Analysis		
				$\Delta p$	$\frac{V}{Q}$	M	N	C	M	N	C	Code-Verif.	Method	M	N
1	Entrance Magn.	 dB/dl v	v $\perp$ B	1	1	0- 3x10 <sup>4</sup>	0- 800	0.003	7x10 <sup>3</sup>	>200	0.04 0.004	yes	CFS*)		$\infty$
2	In- and Outlet	 Expans.C ontract.	v $\perp$ B	1	2	1x10 <sup>5</sup>	4x10 <sup>3</sup>	0.004	6x10 <sup>3</sup>	>200	0.014	yes	CFS		$\infty$
3	In- and Outlet	 Bend B	v $\perp$ B	2	2	2x10 <sup>4</sup>	600	0.005					CFS		$\infty$
4	Back Poloidal Channels	 B	v $\perp$ B	3	1	2x10 <sup>4</sup>	600	0.005	6x10 <sup>3</sup>	>500	0.07	yes	SFM**)		
5	U-Bend	 B	v $\perp$ B	1	2	2x10 <sup>4</sup>	600	0.005							
6	Poloidal Manifold	 B	v $\perp$ B	3	2	1x10 <sup>4</sup>	400	0.007					SFM? CFS		$\infty$
7	Inlet $\rightarrow$ Radial Channels	 B	v $\perp$ B v  B	3	2	1x10 <sup>4</sup> 2x10 <sup>3</sup>	400 50	0.007 0.02	7x10 <sup>3</sup> 2x10 <sup>3</sup>	400 $\geq 50$	?	no	?		
8	Radial-toroidal Bend	 B	v $\perp$ B v  B	2/3	3	2x10 <sup>3</sup>	50	0.02	9x10 <sup>3</sup> 2x10 <sup>3</sup>	1900 $\geq 130$	0.05	yes	CFS		$\infty$
9	Toroidal Channels	 B v	v  B	1	3								?		
10	Multi-Channel	 B	v $\perp$ B	3	3	2x10 <sup>3</sup>	50	0.02	9x10 <sup>3</sup> 2x10 <sup>3</sup>	2x10 <sup>3</sup> $\geq 130$	?	?	CFS		$\infty$

\*) Core Flow Solution \*\*) Slug Flow Model

Table 11: Li-Pb-Blanket: Problems, Evaluation and Assessment of the Validation

The problems of pressure drop and flow distribution in the poloidal channels, as far as they are related to the present design, are rather well understood.

Therefore it was decided to focus the future work on:

- the radial-toroidal bend
- the inlet flow from the poloidal manifold to the radial channels and
- the countercurrent flow problems.

Staff:

L. Barleon  
 L. Bühler  
V. Casal  
 M. Gegenheimer  
 W. Hartmann  
 H. Kreuzinger  
 L. Lenhart  
 K.J. Mack  
 K. Thomauska

## LAM 2.1 LAM Element Activation

In the report period activity calculations for potential low-activation materials have been started. In a first step the well established FISPACT activation code and the related nuclear data libraries UKACT 1 and UKDECAY 2 were transferred from Harwell to Karlsruhe and implemented for use with the KfK central computer. As for all other currently existing activation codes, one weakness of the Harwell code at its adoption was the neglect of so-called "sequential (x,n) reactions" which can produce important contributions to the totally induced radioactivity in fusion reactor materials. Therefore, a special computer program was written, which can handle the additional reactions within the global FISPACT code. The inclusion of sequential (x,n) reactions required also the production of a new library for nuclear data not contained in UKACT1 and UKDECAY2: 1) Double-differential neutron-induced charged-particle-emission cross sections, 2) differential charged-particle-induced reaction cross sections, and 3) stopping powers for the relevant charged particles and target elements. The required data base was collected from published experimental results, recent compilations, evaluations, calculations and systematics.

With the new program capability it was demonstrated for the first time that sequential (x,n) reactions play an important role in element activation of fusion materials. One stressing example is shown in Fig. 63. In this case the activity-related surface  $\gamma$ -dose rates beyond  $\sim 200$  y cooling time are increased by 9 orders of magnitude due to the inclusion of the sequential  $^{23}\text{Na}(\alpha, n)^{26}\text{Al}$  reactions. Inclusion of this type of reactions even places the resulting dose rates at long cooling times clearly above the "hands-on" level of  $2.5 \times 10^{-5}$  Sv/h.

In the meantime the new KfK library KFKXN has been largely extended, which contains now data for a complete coverage of all sequential (p,n), (d,n) and (α,n) reactions on all stable isotopes of the elements Na, Mg, V, Cr and Fe. Further work is in progress to expand the present possibilities to other elements and other sequential reactions, e.g. (x,n'p), (x,n'd), (x,n'α) or (t,n) and ( $^3\text{He}$ ,n). It is, however, expected that sequential (x,n) reactions become less important for high-Z elements and the less frequent charged particles, t and  $^3\text{He}$ . Therefore, future work aims primarily on appropriate systematics needed to establish quantitative criteria for suitable cut-off levels for these reactions.

With the improved activation code first comparative calculations for a few Fe-basis alloys have been made. Together with the induced activities, also the related surface  $\gamma$ -dose rates, the decay heats and the biological hazards are calculated. In addition to all major constituents of the alloys, also the lowest currently attainable impurities of critical elements are treated in such calculations. Work is in progress to study the dependence of the induced activities on largely different fusion reactor spectra.

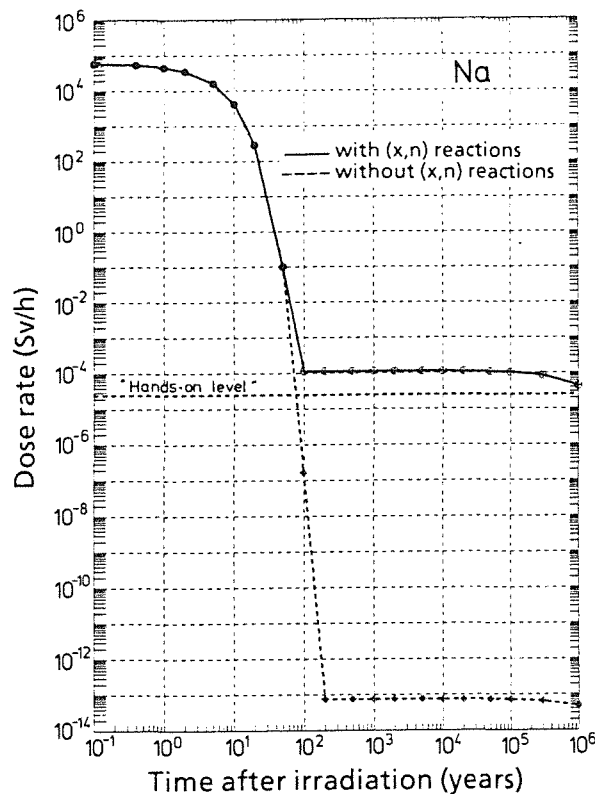


Fig. 63: Calculated surface  $\gamma$ -dose rate vs cooling time for Na. The difference between the two curves is a measure of the contribution of the  $^{26}\text{Al}$  activity produced by sequential  $^{23}\text{Na}(\alpha, n)^{26}\text{Al}$  reactions.

Staff:

S. Cierjacks

Y. Hino

### LAM 3      Development of Low Activation Ferritic-Martensitic Steels

Various heats of a martensitic steel containing 9 to 14% of chromium were used to study, in tensile, creep-rupture and notch impact tests, the influence of the  $\delta$ -ferrite content (0 to 25%) upon the mechanical properties.

The creep-rupture properties are hardly influenced by low  $\delta$ -ferrite contents. At 20%  $\delta$ -ferrite and above the creep-rupture strength decreases and the ultimate elongation increases strongly at high test temperatures (650°C). Further studies will have to be conducted to find out whether this is primarily an effect of chromium or of  $\delta$ -ferrite - content.

Tensile properties are less influenced than creep-rupture properties. Only at 25%  $\delta$ -ferrite, the tensile strength and the yield point are clearly lower.

By analyzing the impact fracture behaviour it could be shown that small amounts of the  $\delta$ -ferrite phase (0.5%) improve the toughness (lowering of the ductile-brittle transition temperature DBTT and increased bending deformation until onset of cleavage fracture). On the other hand, higher amounts of the  $\delta$ -phase significantly favour cleavage fracture

and increase the DBTT. As REM investigations revealed, these opposing effects are caused by the formation of a brittle  $M_{23}C_6$ -layer in the interface between larger  $\delta$ -ferrite grains and the martensitic matrix. The influence of the carbide on the impact properties is especially detrimental if it occurs in a dendrite-like shape. The formation conditions of this constituent have been studied by dilatometry during continuous cooling. It could be shown that  $\delta$ -ferrite without the interface carbides increases ductility. An interpretative model has been presented to rationalize the observed effects.

Depending on the application and type of loading, more or less  $\delta$ -ferrite can be permitted in martensitic steels. For creep and tensile loading, the allowed percentage is below 20%. Under impact loads, small amounts of  $\delta$  may be advantageous, and in the case of larger amounts care must be taken to avoid carbide precipitations forming a continuous layer between the  $\delta$ -ferrite grains and the martensite matrix.

#### Staff:

K. Anderko

E. Materna-Morris

W. Meyer

L. Schäfer

M. Schirra

**MAT 1.9 Pre- and Post-Irradiation Fatigue Properties of 1.4914 Martensitic Steel (MANET)**

Thermal cycling of large components is a serious problem for the designer. The structure considered in the present case is the first wall of a fusion reactor. Its surface, in the actual design concept, will be subjected to radiation heating from the plasma facing side which may lead to severe thermal stresses. Due to the discontinuous operational mode thermal cycling will generate oscillating temperature gradients. These, depending on the loading conditions, will cause elastic or elasto-plastic reversed deformation giving rise to thermal fatigue which at present is considered as the most detrimental lifetime phenomenon for the structure considered. The investigations of MAT 1.9 are devoted to this problem.

The studies to be reported within MAT 1.9 are:

- The influence of temperature upon isothermal low-cycle fatigue behaviour of MANET 1 (H-GRIM specimens).
- Cyclic stress behaviour of MANET 1 (H-GRIM specimens) at 450°C.
- Installation of a new laboratory for thermal fatigue testing.

1. Isothermal fatigue

A test program has been started to study the influence of strain range  $\Delta\epsilon_t$  upon the number of cycles to fracture  $N_f$  of MANET 1 at different temperatures. The results of solid specimens (S-GRIM) have been reported previously. Now first results of hollow specimens (H-GRIM) are available. In Fig. 64 the number of cycles to fracture as function of total strain

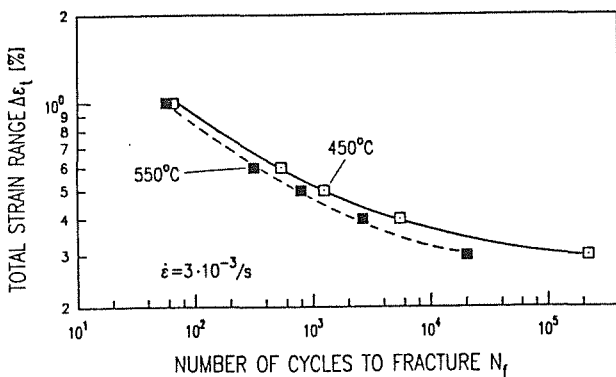


Fig. 64: Total strain range vs. number of cycles to fracture for H-GRIM specimens of MANET 1.

range  $\Delta\epsilon_t$  for 450 and 550°C is shown. From the figure it is obvious that there is only a slight influence of temperature upon  $N_f$ -values for larger strain ranges. This LCF-behaviour of H-GRIM specimens is principally similar in comparison

with results obtained on S-GRIM specimens. For smaller strain amplitudes ( $\Delta\epsilon_t \leq 0.4\%$ ), however, a more pronounced difference of the number of cycles to fracture can be observed for 450°C as compared to  $N_f$ -data obtained at 550°C.

In Fig. 65 the maximum tensile stress  $\sigma_{max}$  is plotted versus

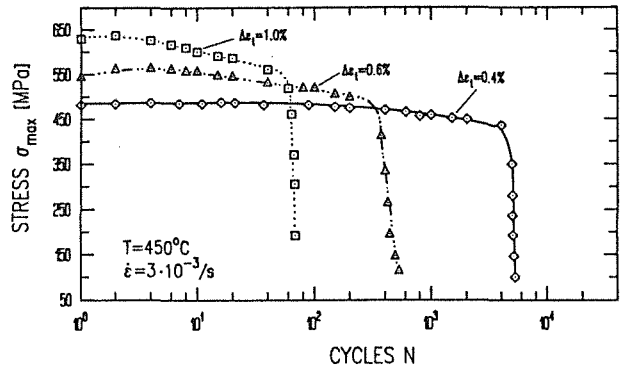


Fig. 65: Maximum tensile stress vs. number of cycles to fracture for MANET 1 (H-GRIM specimens).

the number of cycles  $N$  for different strain ranges. For  $\Delta\epsilon_t = 0.6$  and 1% a small cyclic hardening can be seen. Coming up to the maximum value, a gradually cyclic softening of stress-values occurs. For a strain range of 0.4% the stress remains nearly constant right before specimen fracture occurs.

2. Thermal fatigue

2.1 Installation of a new laboratory for thermal fatigue testing

Nine test rigs, consisting of a heating device, a load frame (four of these until the end of 1989) and the data acquisition system - containing also the load and strain transducer feeding electronics - are installed in a new laboratory for thermal fatigue testing. Fig. 66 shows the final design of such a test rig. As a tenth facility an INSTRON 8000 closed loop material testing machine equipped with a similar heating system is under installation to run thermo-mechanical fatigue tests.

2.2 Thermal fatigue of AISI 316 L

A first data set of thermally cycled AISI 316 L was generated under several thermal conditions and compared with thermomechanical and isothermal data. Thermal fatigue lives are shorter than the isothermal fatigue life at a temperature equal to the mean temperature of thermal cycle and also they are, in some cases, shorter than isothermal fatigue lives at a temperature equal to the maximum temperature of the cycle.

An empirical formula is found to be useful as an approximate life prediction of thermal fatigue lives from isothermal life data of this steel.



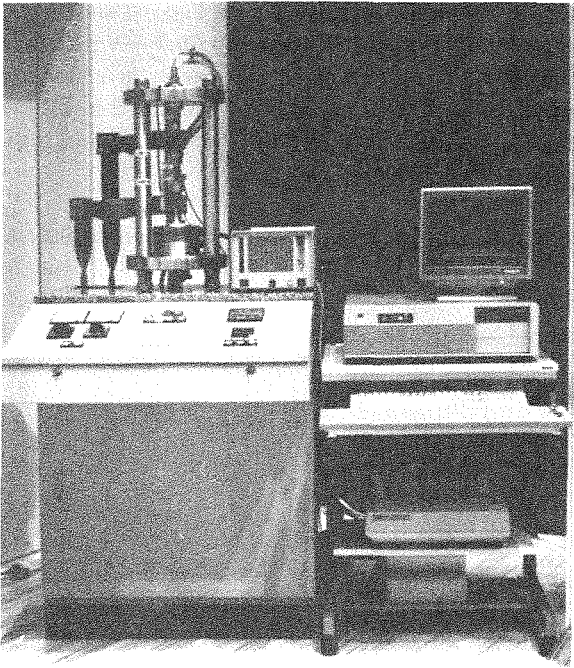


Fig. 66: Thermal fatigue test facility.

Staff:

W. Baumgärtner

M. Bocek

C. Petersen

D. Rodriam

W. Scheibe

R. Schmitt

H. Schneider

W. Schweiger

### MAT 1.11 Post-Irradiation Fracture Toughness of MANET Steel

The influence of neutron irradiation on impact and fracture toughness properties of martensitic/ferritic steels of MANET type will be studied by determining impact energy, ductile to brittle-transition temperature, hardening and microstructural changes in function of the irradiation conditions. In the reporting period an instrumented notched-bar impact bending test device has been completely developed and successfully tested. This new device allows in addition to the determination of the total impact energy also the measurement and recording of the power-path and/or power-time history of each test. This can be achieved by an instrumented hammer fin where a strain gauge extensometer delivers voltage (power) signals which are recorded by a special high-speed analog-digital convertor with a very high resolution rate of one value per  $10^{-6}$  seconds. These power-time data can then be converted by an appropriate computer software into other entities like velocity, momentum or

energy in dependence of time or path. Figs. 67 and 68 give such examples for tested miniaturized Charpy-V-specimens from Manet (1.4914) material. The device is now being installed at the HOT CELL facility of KfK and it is expected that the first tests with preirradiated samples can start in the fourth quarter of 1989.

Regarding the status of the irradiation experiment SIENA-E-198-14 in HFR, the first series of MANET samples irradiated to 5 dpa at 300, 400 and 475°C resp., has been delivered to KfK. The loading scheme for this irradiation experiment, which initially had foreseen fluences up to 30 dpa, has now been revised so that the fluence levels at given temperatures range from 5, 10 to 15 dpa.

Staff:

- B. Dafferner
- K. Ehrlich
- E. Materna-Morris
- (M. Rieth)

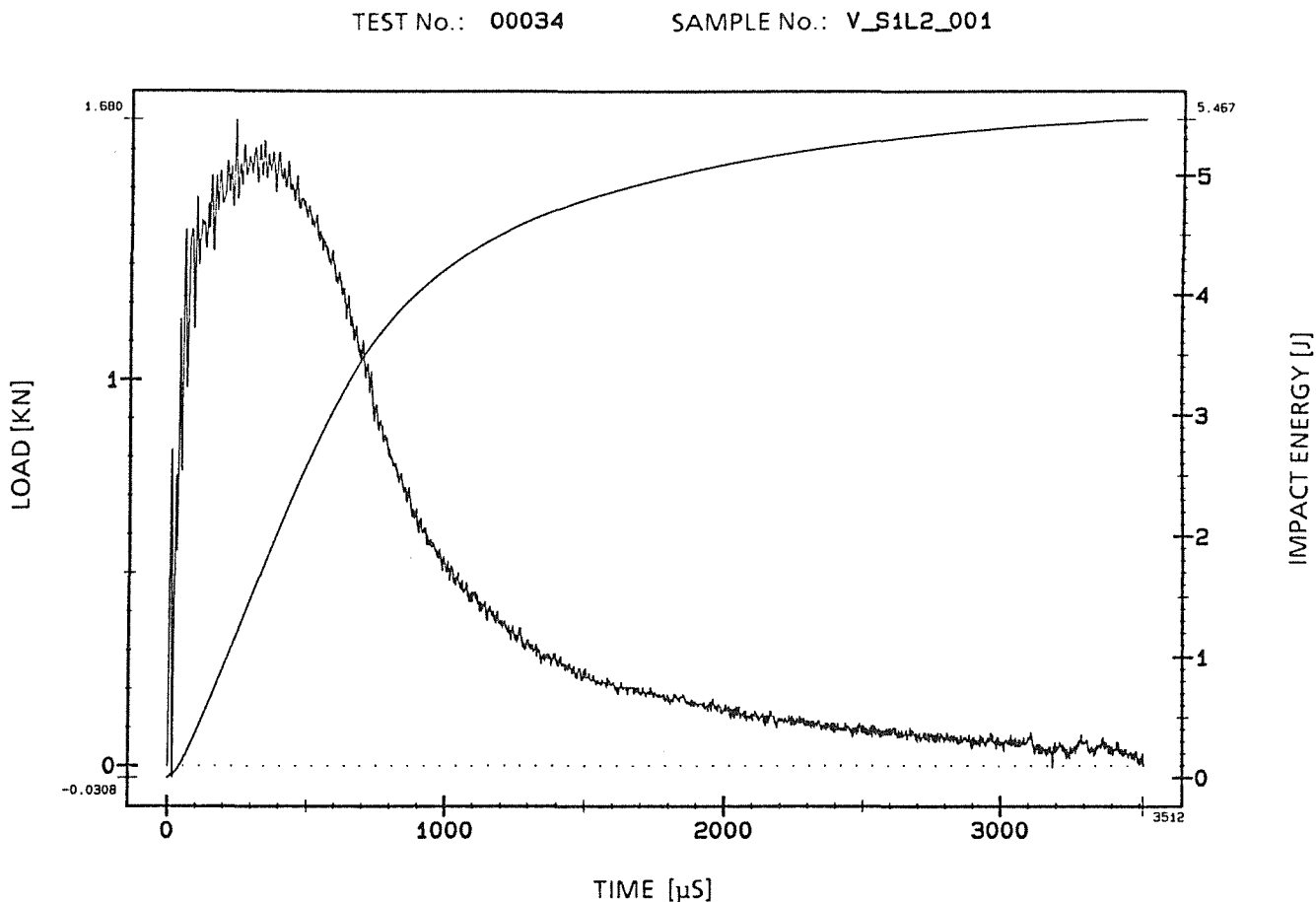


Fig. 67: Load-time-impact-energy time-curves

TEST No.: 00034

SAMPLE No.: V\_S1L2\_001

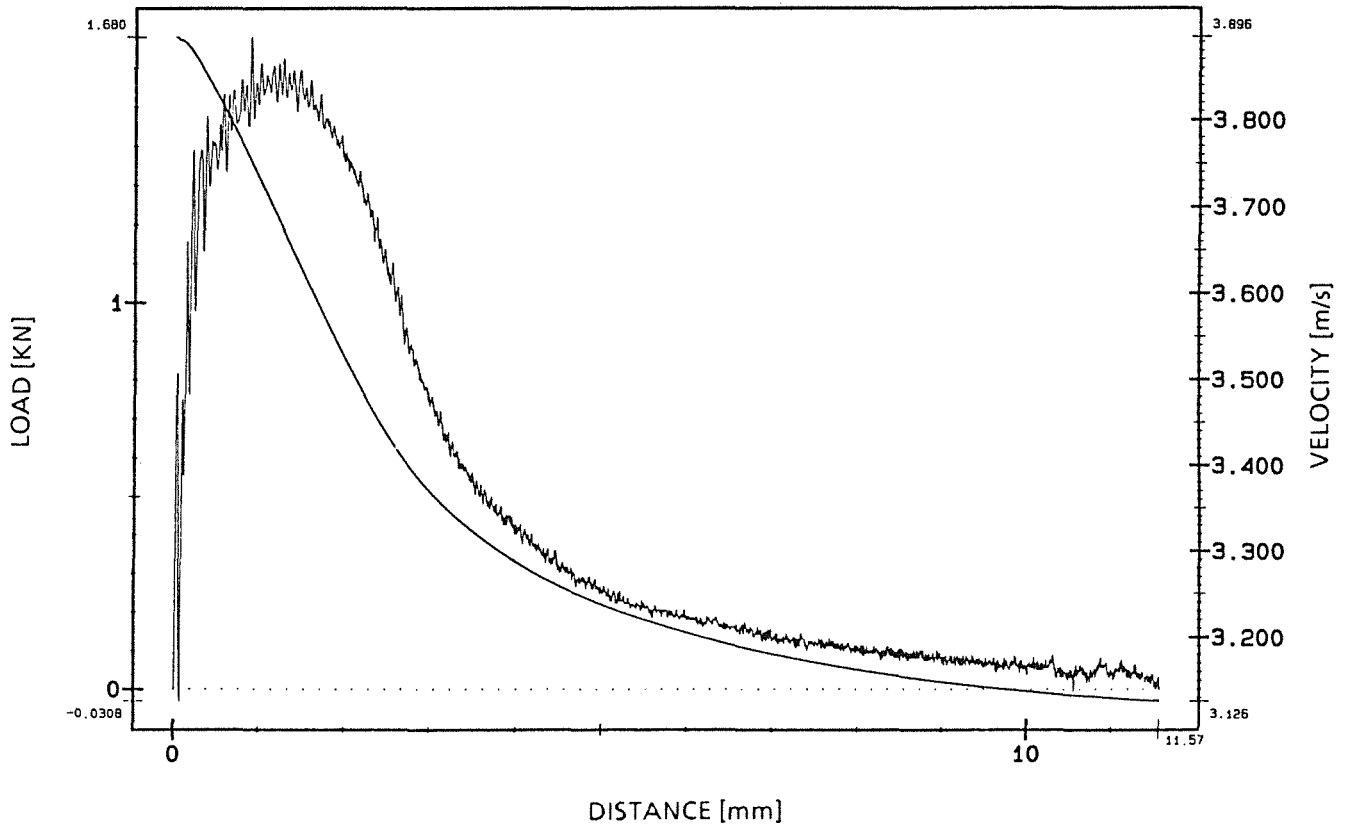


Fig. 68: Load-distance-velocity-distance-curves

## MAT 2.2 In-Pile Creep-Fatigue Testing of MANET

To study the deformation and fracture behavior of the candidate structural martensitic material MANET, DIN 1.4914, a loading device has been constructed which allows cyclic pressurisation of tubes both inside and outside of the reactor KNK II. The long capillary lines connecting the specimens with the compressor, however, result in a gross distortion of the originally square wave pressure pulse to an almost triangular one, as has already been reported. This unavoidable technical problem has to be taken into account when evaluating the data of time-to-rupture experiments carried out with pulsed loading.

The most simple assumption one can make for the evaluation of experiments with changing loads is the so-called life-fraction rule. It is assumed that the damage at different stress levels is accumulative according to the following scheme: The holding times are converted into fractions of the life-time at that particular stress derived from constant stress experiments. It is assumed that rupture occurs when the sum of those fractions reaches unity. The evaluation of an experiment with - as in this case - a more complex, time dependent load history will be outlined in the following with the help of actual time-to-rupture data for the MANET material.

The time-to-rupture under constant load was determined at 560°C for tubes with the dimensions  $\phi$  7.6×0.5 mm. The results can be described to a very good accuracy by the equation

$$\sigma = 482 - 71.9 \log(t_r),$$

where  $\sigma$  is the gas pressure [bar] and  $t_r$  the time-to-rupture [h]. For two different stresses levels  $\sigma_n$ , resp.  $\sigma(t)$ , where the index  $n$  refers to the reference state (in this case  $\sigma_n$  is nominally 450 bar) and  $\sigma(t)$  to the stress at time  $t$ , the momentary ratio of the corresponding rupture times  $t_n/t_r(\sigma(t))$  is

$$t_n/t_r(\sigma(t)) = \exp(0.032(\sigma(t) - \sigma_n)) \text{ or}$$

$$t_n = t_r(\sigma(t)) \times \exp(0.032(\sigma(t) - \sigma_n))$$

In other words,  $t_r(\sigma(t))$  has to be corrected by a normalized weight  $w(t)$

$$w(t) = \exp(0.032(\sigma(t) - \sigma_n))$$

if we refer all momentary rupture times to the reference state.

The effective time  $t_{\text{eff}}$  for each pressure pulse is then

$$t_{\text{eff}} = \int w(t) dt.$$

The time dependence of the pressure build-up in the tube has been determined for a number of nominal pressure values. The hold-time of the square pressure pulse directly on the compressor amounts to 15 sec; the actual pressure in the tube was measured every 0.05 sec and digitally recorded. An example of such a curve is shown in Fig. 69 for a nominal

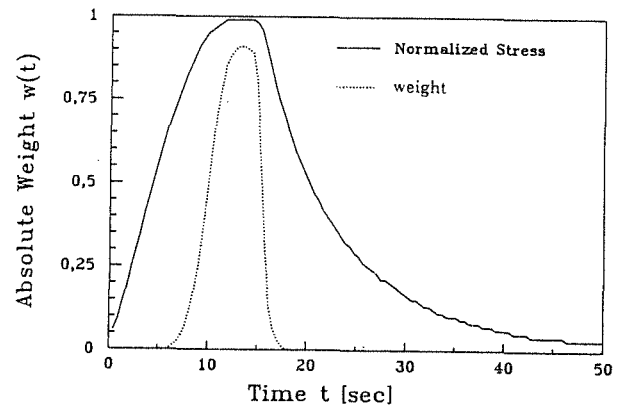


Fig.69 : Time dependence of normalized stress and weight for 450 bar.

pressure of 450 bar; the weight function  $w(t)$  calculated as outlined above is also shown. The most predominant feature of the latter is its narrowness; this is a consequence of the high stress dependence of the time-to-rupture. The curve also never reaches unity; this again is a consequence of the high stress dependence together with the fact that the actual maximum pressure was 2 bar short of its nominal value! The effective time  $t_{\text{eff}}$  is 5.3 sec while the effective time for the pulse is 18.4 sec! Less than 1/3 of the pulse duration is therefore affecting a damage to the sample. Since the time-to-rupture for 450 bar is 2.8 h, 1900 cycles would be required to achieve rupture if the simple damage accumulation mechanism operates in the manner assumed here. This to prove or to disprove would be a relative simple experiment; however, because of the high stress dependence a very high accuracy in the pressure measurements is required.

Staff:

K. Ehrlich

K. Herschbach

G. Reimann

L. Schmidt

## MAT 9.2 Investigation of Fatigue under Dual-Beam Irradiations

The Dual Beam Facility of KfK, where alpha-particles (104 MeV) and protons (15-40 MeV) are focussed on to a target, was developed as a research tool for materials within the European Fusion Technology Programme. This Dual Beam Technique allows the simulation of fusion neutrons by the systematic variation of hydrogen, helium and damage production in thick metal and ceramic specimens as well as the simulation of Tokamak relevant thermal and mechanical loadings in proposed first wall materials.

### 1. Development of the Irradiation Facility

Efficient operation of high energy ion beams from accelerators depends very much on the measurement of the relevant beam parameters within a wide range of ion currents. The beam current may be measured usually by means of faraday cups. However, a complete stop of the beam can not always be tolerated during the experiment. Therefore, we have developed isolated target holders for tensile and low cycle fatigue (LCF) specimens allowing a continuous ion current measurement at the specimen surface and thus the direct destination of damage and implantation doses.

To determine the experimental range of protons (40 MeV) and alpha-particles (104 MeV) in unknown materials the current of the degrader and specimen passing ions can now be measured as a function of the degrader thickness. The range and the longitudinal range straggling can then be determined from the slope of the current decrease.

At the Dual Beam facility homogeneous beam density profiles are necessary. In order to measure absolute beam density profiles within a wide range of densities, a monitor system was installed consisting of a profile harp with 18 wires, a slit collimator, a microprocessor controlled electronic, and a plot software recently developed. This beam density profile monitor allows the quick generation of beam density profiles. The density profiles in Fig. 70 measured 10 cm in front of the specimen are typical for the proton beam. Degrader passing particles lead to a fairly uniform profile within an area of about 100 mm<sup>2</sup>.

In the reporting period also the detailed specification and construction of the vacuum irradiation chamber for in-beam LCF-experiments could be finished together with the adaption of the pulling rods.

### 2. Tensile deformation behaviour of helium implanted steel DIN 1.4914

Tensile specimens of the fully martensitic 12% Cr-steel DIN 1.4914 (1075°C/30' + 750°C/2h) were homogeneously helium implanted within the wide temperature region 200°-720°C. These implantations were performed at a high He/dpa ratio of 1850 appm He/dpa. However, the damage rate was very similar to that predicted for NET being in the range of  $3 \times 10^{-7}$

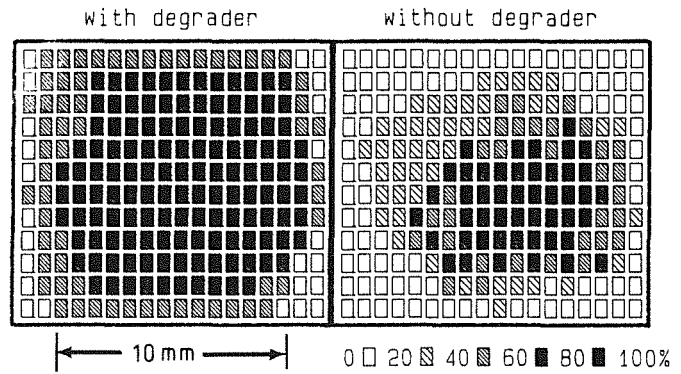


Fig. 70: Beam density profiles of the proton beam (30 MeV, 20  $\mu$ A) measured with a developed profile monitor. Protons passing the degrader cause a fairly uniform profile with  $10 \times 10$  mm<sup>2</sup>

dpa/s. After irradiation tensile tests were conducted mainly at temperatures  $T_T$  equal to the irradiation temperature  $T_I$  in a vacuum furnace. Part of the experimental data including TEM, SEM and metallography were already described in previous annual reports. These investigations were continued and combined with calculations taking into account helium and defect induced strengthening and work hardening mechanism. In the following a picture of the structural evolution is summarized.

The measured yield strength increases below implantation temperatures of 400° and decreases above 450°C. The underlying phenomena can be understood by an overlapping of hardening induced by submicroscopic defect agglomerates below 300°C, small sized He-bubbles above 300°C and microstructural softening induced by dislocation climb and annihilation resulting in a decrease of dislocation density during irradiation. The temperature dependent hardening contribution can be well described by a modified statistical barrier model which describes dislocation motion over barriers including equilibrium He-bubbles and defect clusters. Assuming superposable strengthening components, the softening contribution can then be deduced by subtracting the hardening contribution from the experimental change in yield strength. In this way the irradiation softening was deduced and shown in Fig. 71 as function of displacement damage. This softening component which usually cannot be determined directly agrees well with predictions of the irradiation induced decrease in dislocation density given by the final heat treatment.

The work hardening behaviour observed agrees with the observations on strengthening results. Contrary to fcc metals the initial strain hardening coefficient increases with yield stress and the values are higher. A comparison with neutron irradiated specimens shows that the main hardening is induced by displacement damage, which in the neutron irradiated specimens is about two orders of magnitude higher than in the helium implanted ones resulting in a formation of distinct dislocation loops.

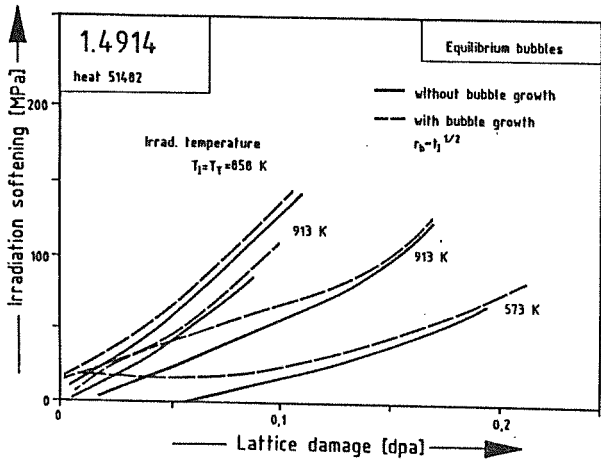


Fig. 71: The irradiation softening deduced from the experimentally determined yield strength and the calculated irradiation hardening as function of displacement damage;  $r_b$  and  $t_1$  are He-bubble radius and irradiation time, respectively.

### 3. Postirradiation Low Cycle Fatigue Experiments

To investigate the effect of helium and damage on the low cycle fatigue behaviour at different temperatures, LCF specimens (H-GRIM geometry) made of steel DIN 1.4914, heat MANET 1 were irradiated between 300°C and 600°C with helium contents up to 200 appm and damage levels up to 1.2 dpa in vacuum ( $0.5 \times 10^{-4}$  Pa) at a typical defect rate of  $2 \times 10^{-6}$  dpa/s. The irradiations were performed using both beams simultaneously. The irradiation temperature was controlled within a few degrees by the flow rate of the helium

gas inside the tubular specimens. After irradiation the specimens were transferred to the hot cells and LCF-tested in air at test temperatures equal to the irradiation temperature. The strain controlled LCF-experiments (Fig. 72) show that in specimens with 200 appm He and 1.2 dpa the stress amplitude is increased at 300°C by 11% whereas it is slightly decreased by 1% at 600°C. At 450°C the stress amplitude remains unaffected by He-implantation. This behaviour is in accordance with tensile results. Fig. 3 also shows that the ratio of the stress-amplitude  $\Delta\sigma_{irr}/\Delta\sigma_{unirr}$  is practically independent of the number of cycles  $N$ . Consequently the hardening or softening behaviour can be determined within the first cycle, that means with tensile experiments which are comparatively easy to perform. An important result of the LCF-experiments is that under all irradiation conditions only small changes in the number of cycles to fracture  $N_f$  were found. Helium contents up to 200 appm corresponding to about 200% of the total amount of helium in a first wall (NET 1) tend to decrease  $N_f$  up to 20%. Such small differences can be established because of the specimen geometry which allows the determination of  $N_f$  within 8-10%. The specimens are now going to be investigated with metallographic and electron microscopic methods.

#### References:

- [1] A. Möslang  
Jahrestagung Kerntechnik '89, May 09-11, 1989  
(Düsseldorf), p. 625; ISSN 0720-9207
- [2] D. Preininger and A. Möslang  
Hauptversammlung der DGM '89, May 16-19, 1989  
(Karlsruhe)

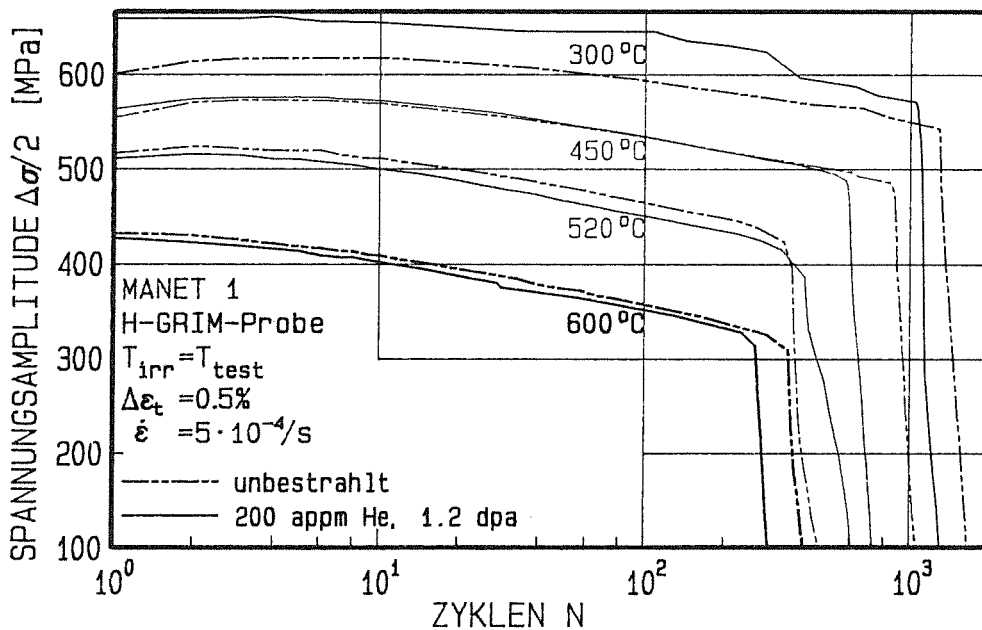


Fig. 72: Evolution of the stress amplitude during strain controlled low-cycle fatigue testing in unirradiated and dual-beam irradiated fatigue specimens.

- [3] A. Möslang, S. Cierjacks and R. Lindau  
Inv. paper presented at 12th Intern. Conf. on  
Cyclotrons and their applications; May 08-12, 1989  
(Berlin)

Staff:

S. Baumgärtner

G. Bürkle

R. Lindau

A. Möslang

D. Preininger

G. Przykutta

## Development of ECRH Power Sources

The task aims at developing mm-wave power to supply current plasma experiments and NET / ITER with electron cyclotron heating (ECRH).

During a test period from March to August 1989 the 140 GHz modular gyrotron was operated with a modified resonator, which had a lower Q-value and hence reduced surface losses. The cavity (length 16.5 mm, radius 3.45 mm, taper angle 0.1°) was designed to generate power in the TE<sub>031</sub>-mode at 140 GHz. The nominal beam voltage and current were 70 kV and 8 A, respectively. The magnetic field in the cavity has provided by a superconducting magnet system. For operation at 140 GHz a magnetic field of 5,42 T is required in the interaction region.

The output power travels from the cavity through the collector and leaves the tube through a couple-disc ceramic window (Al<sub>2</sub>O<sub>3</sub>). The spent electron beam follows the diverging magnetic field lines out of the cavity and is deposited on the copper walls of the water cooled collector.

Following the reassembly of the tube with the new resonator an outgassing heat treatment procedure at 480°C was done in an inertial gas furnace.

During the first tests of the tube, peak output powers up to 215 kW at 25 % efficiency were produced with pulse durations of 0,5 ms in the TE<sub>03</sub>-mode at 139.57 GHz. A plot of output power and efficiency versus beam current is shown in Fig. 73.

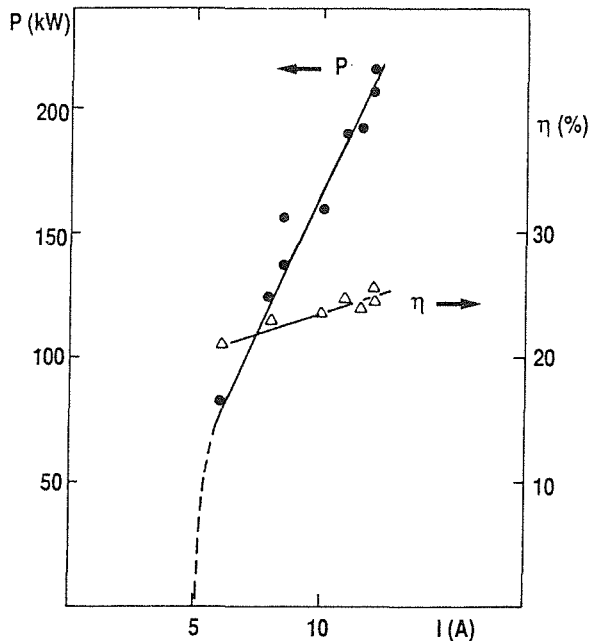


Fig. 73: Output power and efficiency versus current for a beam voltage of 70.5 kV

In course of these measurements, the cavity magnetic field, the beam voltage and the gun-anode voltage were optimized.

The output window was tuned by changing the distance between the ceramic discs. The maximum output power for the TE<sub>03</sub>-mode was found at a distance of 4.06 mm in agreement with previous measurements with the 10 mm resonator.

The TE<sub>23</sub>-mode at 136.74 GHz was measured, too. A maximum output power of 128 kW at 16.4 % efficiency was obtained.

In addition to the short pulse measurements (0.5 pps repetition, 0.5 ms duration) tests were carried out up to 100 ms pulse duration. This operation uses the new high voltage power supply having a 3 MW CW capability. Operation with long pulse duration showed some instabilities of the high voltage power supply and of the electron gun related to vacuum problems during the furnace treatment. Measurements with the optimized parameters of beam voltage and gun-anode voltage were not possible because of excessive gun current. Therefore, the long pulse duration measurements were carried out at reduced output power. A pulse power of 50 to 90 kW was obtained when operating at a duty cycle of 0.5 % (0.05 pps, 100 ms duration). In Fig. 74 the

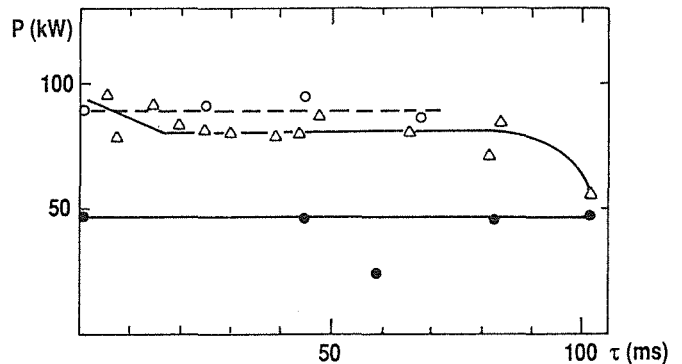


Fig. 74: Output power versus pulse duration for different beam parameters (beam voltage/gun-anode voltage: 73.0 kV/23.4 kV, 74.2 kV/25.0 kV and 73.0 kV/25.4kV respectively)

output power versus pulse duration is plotted for three test runs with different operating parameters.

The output window was cooled with nitrogen gas during most long pulse duration experiments. Finally FC-75 cooling of the output window using a system of IPP Garching has been successfully tested.

The resonator was water-cooled for the long pulse operation. Nevertheless the power losses in the cavity wall were too high, consequently the cavity geometry changed. This could be seen by the frequency of the tube, which increased by 500-600 MHz systematically in all modes during the long pulse measurements. Subsequent to the tests, the tube was disassembled and examined for possible damage. A portion of the inner cavity surface was significantly damaged.



The industrial prototype gyrotron was manufactured and heat conditioned in the meantime. This gyrotron was placed in the second test stand using a new superconducting magnet with enlarged borehole and a new high voltage assembly. A series of tests is now in progress, which already shows promising results: 300 kW with ~35% efficiency at 0.5 ms pulse length were obtained in the first run.

Staff:

W. Baumgärtner  
E. Borie  
H. Budig  
G. Dammertz  
O. Dumbrais  
U. Feißt  
G. Gantenbain  
T. Geist  
P. Grundel  
G. Hochschild  
A. Hornung  
M. Kuntze  
R. Lehm  
N. Münch  
H.U. Nickel  
H. Oppermann  
B. Piosczyk  
G. Redemann  
R. Vincon  
H. Wenzelburger

## NET Study Contracts

### Electrical Connectors for Remote Handling

The report performed under contract No. 201-85-1FuAF has been reviewed.

As far as the preliminary status of the NET-layout permits connector applications and environmental conditions at NET have been investigated.

The results have been documented in a Requirement Definition Document (RDD) which was presented to NET mid 1989.

The draft of the design proposal for a family of connectors has been made and presented to NET.

A set of data sheets has been completed and attached to the design proposal to be included in the remote handling manual by NET.

#### Staff:

H. Haas

M. Selig

### Study of a Plasma Exhaust Purification System for NET Based on Catalytic Reduction of Impurities: Phase 2 - Engineering Study

The engineering design of a catalytic plasma exhaust gas clean-up facility for NET II / ITER is being carried out jointly by KfK and KAH, as the industrial subcontractor, within the frame of a second contract with the Commission of the European Communities and in close contact with staff members of the NET Team.

The essential features of the process concept have been discussed in previous reports. The basic flow sheet proposed for NET II (Fig. 75) comprises two main routes: i) processing of the plasma exhaust gas from burn and dwell, bake out, carbonization and helium / deuterium glow discharge and ii) processing of the gas from air in-break or from helium flooding.

As shown on the process flow sheet in Fig. 76 the bulk separation of molecular hydrogen from impurities is achieved with a commercial palladium / silver permeator (approx. 1 m<sup>2</sup> permeation area). Hydrogen isotope pumping is carried out with a commercial oil-free 600 N m<sup>3</sup>/h NORMETEX pump, which is also the largest single process component. The combination permeator / pump is redundant to ensure that the main hydrogen flow can always be processed. The loop used for the semi-continuous processing of the permeator bleed gas consists of a 10 kg commercial Ni catalyst bed, an

approx. 1 kg commercial water gas shift catalyst bed and another 1 m<sup>2</sup> palladium / silver permeator evacuated by a 15 Nm<sup>3</sup>/h NORMETEX pump coupled to a D7 NORMETEX pump. Both catalyst beds are designed to last for the complete period of operation of the NET II / ITER reactor.

Pump-down gases from reactor flooding with air or helium are processed in a once-through modus. For this purpose hydrogen and the impurities are first oxidized to water and carbon dioxide on a noble metal catalyst bed and the produced water retained in an appropriate cryotrap. Condensed water is first volatilized employing carbon monoxide as a carrier gas and then sent through a water gas shift catalyst bed (approx. 50 kg). Next, the effluent gas from the catalyst bed is passed through the first 1 m<sup>2</sup> permeator and afterwards through a second water gas shift catalyst bed (1 kg catalyst) as well as through the permeator of the loop described above. The off-gas from this once-through process is discharged directly into the tritium retention system.

Engineering flow sheets including control circuits and instrumentation, together with component lists, and data sheets are available. Preliminary safety considerations and cost estimates are in preparation.

The catalytic process has been selected as one of two options for ITER during an Expert Meeting in August 1989.

#### Staff:

M. Glugla

R.-D. Penzhorn

D. Herbrechter (KAH)

### NET Remote Workstation

The remote handling equipment at NET like the in-vessel handling unit (IVHU), the bridge mounted transporter and others will be controlled from the Remote Handling Control Room via the NET Remote Handling Workstations (NRWS). These workstations represent the operator's interface to the equipment control systems and the remote handling site. But interfacing is not the only purpose: the NRWS shall help the operator in performing his maintenance tasks.

The NRWS is the top-level (task level) component of the hierarchical remote handling control system shown in Figure 77. The remote handling control system is partitioned into so-called RH-(remote handling) areas as for example the IVHU area. The basic principle of the remote handling control system is to provide a mixed-mode control, such that the operator may work manually with computer support or may start an automatic preprogrammed procedure with the possibility to intervene in case of malfunction or unforeseen events. The

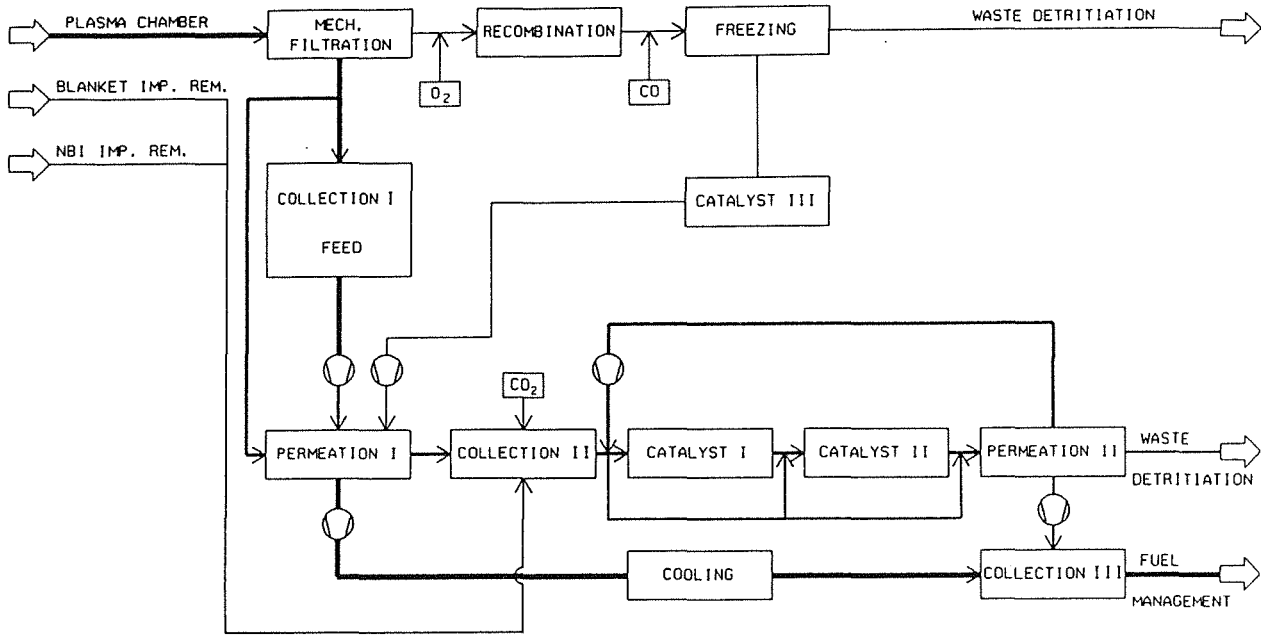


Fig. 75: Basic flow sheet

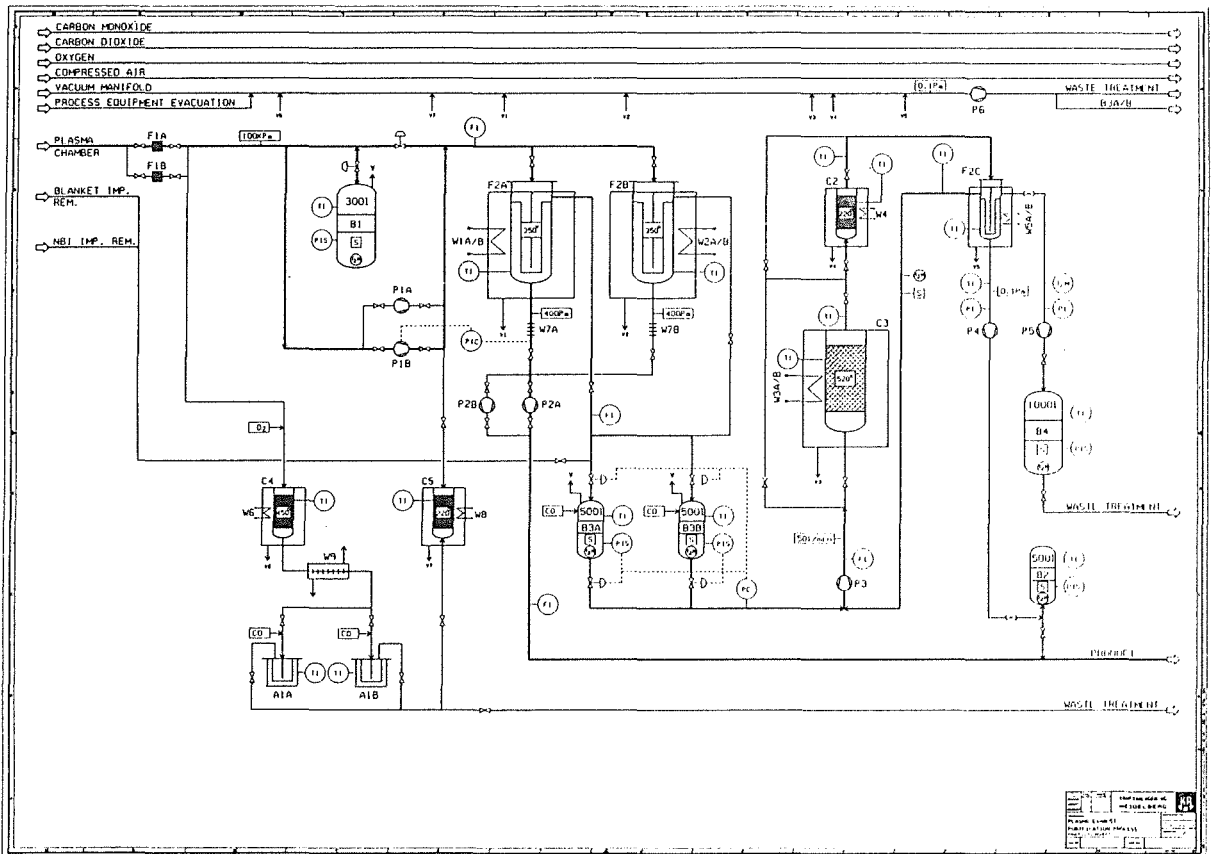


Fig. 76: Process flow sheet of catalytic gas clean up process concept for NET II / ITER

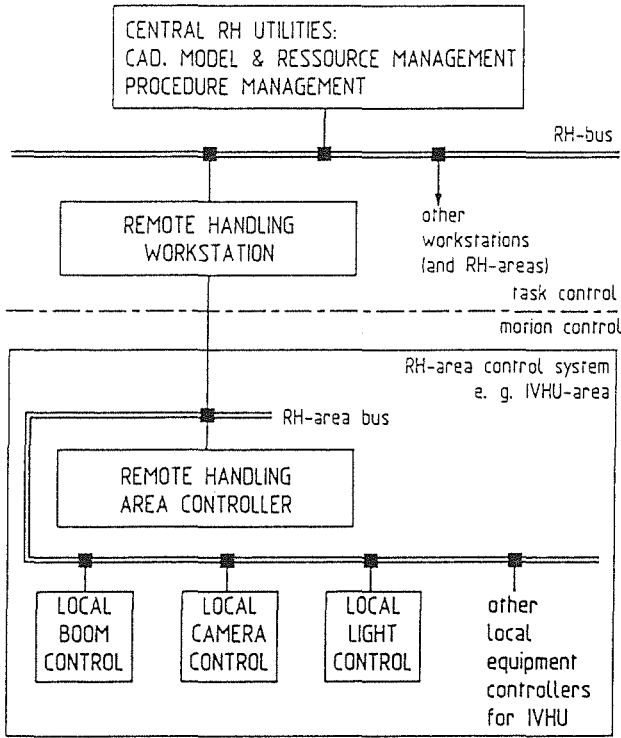


Fig. 77: Hierarchical NET remote handling control system: The NRWS provides the man-machine interface to the control system and general support tools

NRWS may be configured for usage at different area control systems.

In a state-of-the-art review the JET remote handling workstation and its environment was studied but also workstations used in similar applications like space station construction and maintenance, off-shore oil platforms repair, reprocessing plant maintenance and others.

Three alternative general concepts for the development of the NRWS were investigated:

- a general purpose NRWS adaptable to all remote handling control systems;
- a special purpose NRWS, scissored to the related control system,
- an off-line NRWS, which is not connected to a control system and provides only general support tools. In this case the man-machine interface is integrated into the control system.

The basic arguments for a general purpose NRWS are (1) multiple usage, (2) uniform interface for all operations, (3) provision of a pool of operating support tools, and (4) high performance hardware can be advocated because of multiple usage. The recommendation for the NRWS is a combination: to develop a general purpose NRWS for the general support tools (see below) but enable the integration of special purpose

operating software interfaces (Bedienoberflächen) of the different control systems into the NRWS.

Based on the general concept and the state-of-the-art studies a requirements definition document for the NRWS was worked out. The following functions and aids for the operator should be provided by the NRWS:

- Man-machine interface management
- Integrated viewing, combining TV-viewing and computer graphics supported viewing
- Spatial (geometric/kinematic) simulator for motion simulation
- Functional simulator for remote handling procedures simulation
- Planning support for procedure as well as motion planning
- Advisory support to guide the operator through planned maintenance procedures
- Execution monitoring to ensure right execution of planned maintenance procedures
- Failure detection in case of malfunction of the remote handling equipment
- Collision detection
- Training support

The compatibility with the NET overall control system is guaranteed by using the same hardware and software standards important for integration and maintenance.

Staff:

K. Leinemann

**Doses due to Tritium Releases by NET - Data Base and Relevant Parameters**

The assessment of the radiological impact of tritium releases is an essential part of the safety considerations which go in parallel with the development of fusion reactor technology. In the current stage of development it is necessary to predict the impact of probable tritium releases for licencing purposes. Mathematical models and computer codes, which are based on the current understanding of the problems and on existing relevant data, are effective tools for this task. But necessarily they simplify the real system.

This study reviews the current knowledge on the tritium behaviour in biological systems after a tritium release to the atmosphere considering different chemical forms of tritium that can be released by fusion reactors. It deals with tritium

uptake by plants, standing at the beginning of the food chain, the tritium turnover in animals, the different pathways by which tritium can reach man, and finally its behaviour in man, representing the end of the food chain. Existing models, which are intended to estimate the dose consequences from tritium releases to the atmosphere, are compared with respect to the assumptions which are made to describe this nexus of problems.

The intermediate report has been submitted to NET in July 1989. The draft final report is expected in October and the final report in November 1989.

Publications

The study will be published as KfK-report.

Staff:

Dr. S. Diabaté

Dr. S. Strack

**Fatigue Characterization of Jacket Materials at 4 K**

The cryogenic materials investigation program has been initiated by NET with the purpose of the dynamic load characterization of the jacket materials designed for the NET OH-coil. The reference conductor will be a cable in conduit Nb<sub>3</sub>Sn wind and react type. The conductor development is within the responsibility of Asea Brown Boveri (ABB). The materials testing and the materials qualification program are under contract with EMPA, Switzerland. Cryogenic fatigue investigations are required as the OH coil shall be exposed to frequent dynamic loading KfK is equipped to carry out these qualification tests at low temperatures and under cyclic loading.

Two types of materials will be tested. The plate material A 410 (~ 316 LN), supplied by Böhler, and Incoloy 908. Main interest is to characterize the dynamic materials performance in the heat treated condition (50 h/700°C). Therefore these investigations comprise specimens in heat treated condition and in addition in their base and welded configuration. The welding process has been chosen from ABB as a flush butt welding, which produces a very narrow uniform weld profile along the thickness. The investigation carried out by KfK will be conducted in the newly installed cryogenic test facility (Fig. 78). The testing system allows to measure the materials fatigue crack growth rate (FCGR) as well as the fatigue life performance. The FCGR specimens are compact tension type (63 x 60 x 6 mm<sup>3</sup>) with a starting crack length/crack width ratio of  $a/W \sim 0.3$ . The smooth-bar axial fatigue-life measurements are carried out with cylindrical specimens of 5 mm and/or 3,5 mm diameter reduced section. Length of the reduced section is 20 mm.

Figure 78 shows the overall view of the already working machine. Details of this system are given schematically in

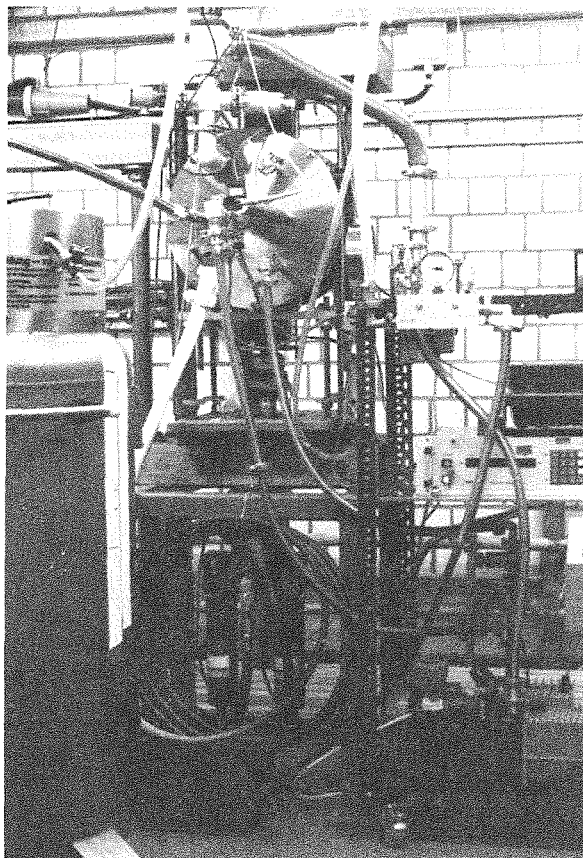


Fig. 78: Overall view of the cryogenic test facility

Fig. 79. This facility comprises a 25 kN servohydraulic unit

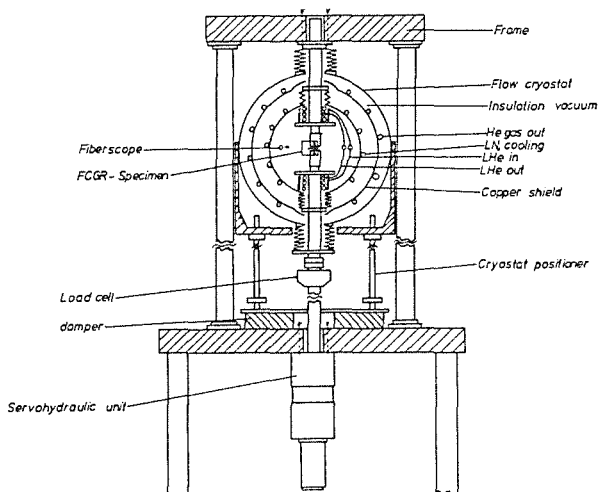


Fig. 79: Details of the cryogenic dynamic materials test facility. The flow cryostat allows continuous testings between 300 K - ~ 6 K within  $\pm 1$  K.

(MTS, Model 244.12), which is coupled with a helium flow cryostat in a special load frame allowing to test specimens in cryogenic regime < 10 K. The cryostat has a 260 mm inner diameter and is equipped with two 30 mm diameter pulling rods. The cool down procedure is carried out in two stages (LN<sub>2</sub> and LHe). Figure 80 shows a typical cool down plot. The cool down procedure is semi automatic, thus may start during

the night time. This gives the possibility of a test duration time of ~ 6 hours daily. Two tests can be carried out weekly.

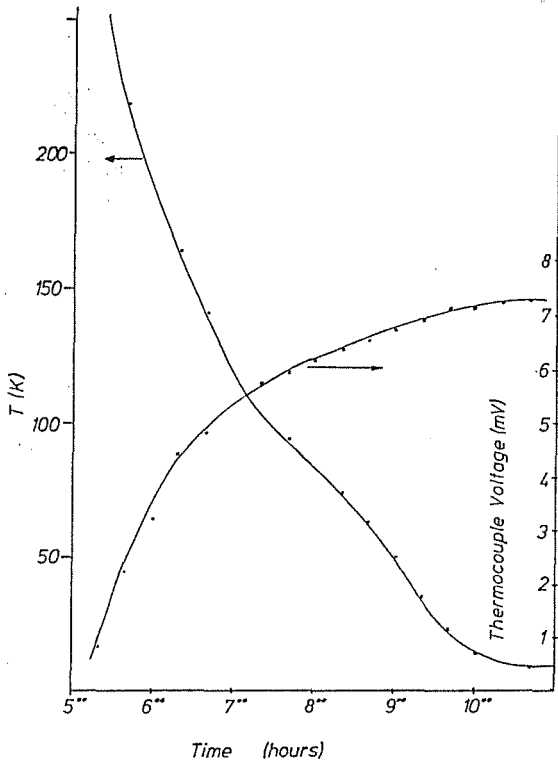


Fig. 80: Cool down plot of the specimen consisting base metal (A 410). The thermocouple (NiCr/Ni) was positioned in the fillet region of the specimen 4 mm apart of the reduced section.

**Results**

Figure 81 shows the 10 K fatigue-life results of the material A 410 (~316LN).

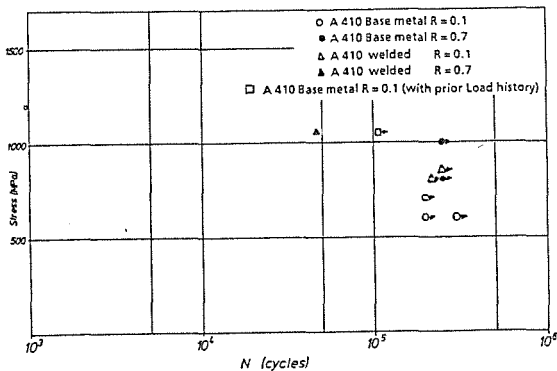


Fig. 81: 10 K fatigue-life (S-N) results of the materials A 410 base and welded condition. The arrows indicate the survival of the specimen.

Cycling of the specimens up to  $N = 2.5 \cdot 10^5$  cycles below the maximum stress level of 1000 MPa results in no failures. This

is true for the base and as well as for the welded condition. The load ratio 0.1 and 0.7 show in this testing regime no detectable effect. Because of the limited load capacity (25 kN) of the actuator the diameter of the specimen was decreased from 5 mm  $\varnothing$  to 3,5 mm  $\varnothing$ . With the 3,5 mm  $\varnothing$  specimens we could then perform 10 K stress-strain measurements after a given load history. Figure 82 shows the stress-strain property of a welded specimen, which was cycled before the tensile test at a maximum stress of 850 MPa and  $R = 0.1$  for 250 000 cycles. The 10 K tensile data show no mechanical degradation, which confirm the superior characteristics of this material. In addition, a specimen with 5 mm  $\varnothing$  consisting of A 410 base metal was prepared to detect the eventual temperature increase during cycling. A NiCr/Ni thermocouple was positioned in the interior of the fillet region (4 mm apart of the reduced section). The cool down plot is given in Fig. 80. The prior load history of this specimen was  $2 \cdot 10^5$  cycles at 600 MPa and  $R = 0.1$ ,  $T = 10$  K. The load frequency of 12 Hz and 1050 MPa maximum stress at  $R = 0.1$  ( $T = 10$  K) showed no detectable temperature rise. Increase of the load by stroke control resulted in serrations starting above 1200 MPa. The temperature increase could be measured to be ~ 5 K after each serration. This specimen sustained also the stress level of 1050 MPa for a cycle number of  $1.1 \cdot 10^5$  cycles and no failure could be detected. Again this incidence show the high performance of the material A 410 (~ 316 LN) at cryogenic temperatures..

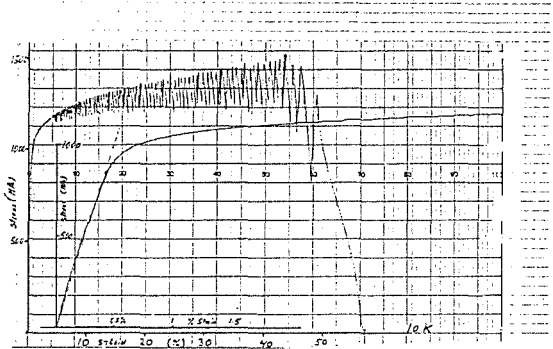


Fig. 82: 10 K stress-strain curve of the base metal A 410 in the welded condition after  $2.5 \cdot 10^5$  cycles at 850 MPa maximum stress and  $R = 0.1$ . Measured mechanical properties at 10 K are:  $\sigma_y = 998$  MPa, UTS = 1523 MPa and Elongation = 49 %.

Staff:

H.P. Raber

A. Nyilas

### Doses due to Activation Product Releases by NET Plasma Facing Components - Review and Procurement of Data Base

The program system UFOMOD is being used for NET to calculate acute and long term doses to individuals and the general public for accidental releases of activation products. At present, the list of nuclides considered in the ingestion model contains data for 30 nuclides only, which do not include all relevant activation products possibly released from fusion reactor devices like NET.

Therefore a contract has been given to the Gesellschaft für Strahlen- und Umweltforschung (GSF) mbH, Neuherberg, to calculate with ECOSYS specific activity concentrations for 8 foodstuffs and for nuclides of the elements Cr, V, Mn, Fe, Ni, Co, Mo and W as basic input data for the ingestion model of UFOMOD.

The phase of data collection and evaluation will be finished at the beginning of November 1989. Then these data will be fed into the dynamic model ECOSYS and calculations will be made for a deposition of radionuclides for the characteristic dates January 1 and July 1. The time-dependent activity concentrations as well as the time-integrated activity concentrations will be calculated as requested in the contract.

Then the data will be implemented in the program system UFOMOD and preliminary dose calculations for activation product releases will be completed.

Staff:

J. Ehrhardt

### Vacuum Pumping Support

(Follow-up of: Investigation on the Vacuum and exhaust Performance of NET)

The final report of the study contract: Investigation on the Vacuum and Exhaust Performance of NET was completed and has been approved by NET. Continuation of the cooperation in the field of vacuum technology will take place within the frame of a new study contract titled: Vacuum Pumping Support. The main topics of this contract concern exhaust duct-, cryopump-, bakeout- and dwell-time calculations including the development and improving of the required computer codes.

Work was started with calculations of the conductivity of different exhaust duct layouts (including the complex shaped divertor channel) in close contact with the NET/ITER design team. To reach adequate performance data it was necessary to increase the divertor channel height as much as possible because of the limited

horizontal space available between the shielding of the 16 toroidal coils. A first acceptable design of the inner portion of the exhaust duct is shown in Fig.83.

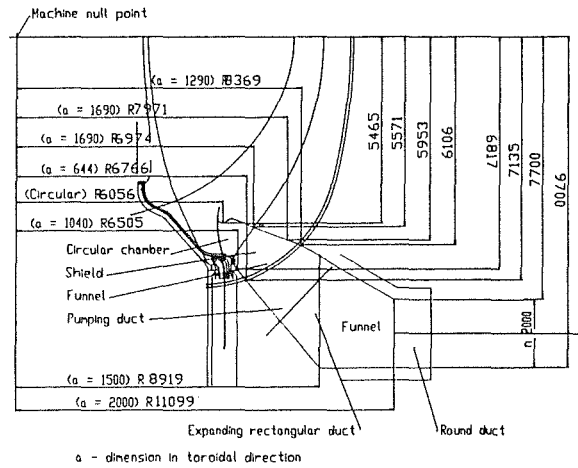


Figure 83 : Inner portion of the exhaust duct (first design with adequate vacuum performance)

Staff:

R.A. Müller

### Fracture-Mechanical Investigation for the NET Microwave Window

(Contribution to anticipated NET-Study Contract)

After calculating the temperature and stress state in the HF-window as well as determining the failure-relevant material data as inert strength, subcritical crack growth parameters and fracture toughness, lifetime predictions could be performed. In Fig. 84 the failure probabilities for spontaneous and delayed failure are represented for the two candidate materials Al<sub>2</sub>O<sub>3</sub> and AlN in dependence of the power W. From this result it is obvious that AlN is superior to Al<sub>2</sub>O<sub>3</sub>. Whilst for W = 200 kW the Al<sub>2</sub>O<sub>3</sub>-window will fail by spontaneous crack extension the AlN-window shows an only extremely low probability of spontaneous failure, and also the probability of delayed failure by subcritical crack growth is very low.

Since the HF-source operates in a non-steady-state mode, cyclic fatigue can occur and the lifetimes may be significantly reduced. This failure behaviour will be investigated in future.

Staff:

T. Fett

D. Munz

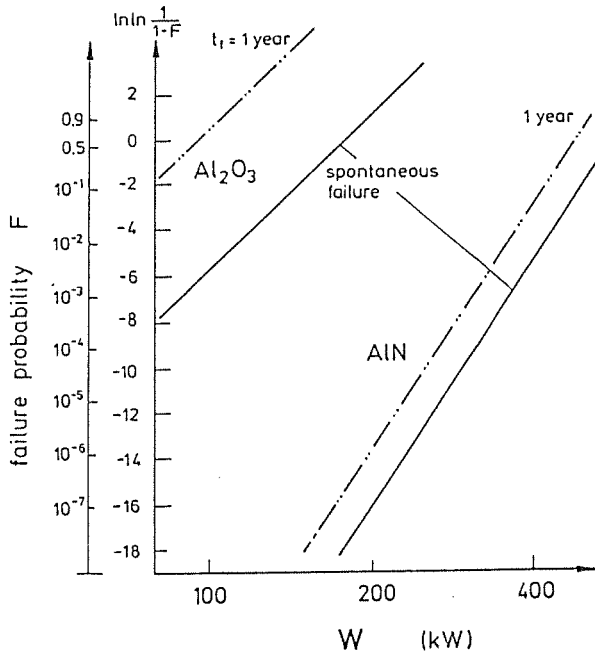


Fig. 84: Failure probabilities for HF windows



**Appendix I: Allocation of Tasks**

Task No.	Title	KfK Departments
<b><u>Plasma Facing Components</u></b>		
PSM 3	Pre- and Post-Irradiation Low Cycle Fatigue of Reference 316 L Steel and Welds	IMF I
PSM 8	Coatings and Surface Effects on 316 L	IMF I, IMF IV
PPM 1	Material Characterization and Neutron Irradiation Effects in Graphites, CFCs and Ceramic Composites	IMF I
PPM 4	Material Characterization and Irradiation Effects in Ceramic Insulators	IMF I
PDT 1	Thermomechanical Tests of First Wall Mock-ups	IMF IV, IRB
PDT 2	Tests of Divertor Samples and Mock-ups	IRE
<b><u>Magnets</u></b>		
MTC 1	Industrial Manufacturing of a few km of React-and-Wind Nb <sub>3</sub> Sn Conductors and of TF Model Coils	ITP
MIC 1	Manufacturing and Testing of Short Length Full-Size A 15 W/R Conductor (Inner Coil)	ITP
MOC 1	Manufacturing and Testing of Short Length Full -Size NbTi Conductor (Outer Coil)	ITP
MOC 2	Design and Manufacture of one Outer Coil (NbTi) and Installation in TORE SUPRA	ITP
MTF 2	Upgrade of the TOSKA Facility for Model Coils Testing	ITP, HIT
MSA 1	Safety Relevant Models and Experiments for NET Magnets	ITP
<b><u>Tritium (Fuel Cycle)</u></b>		
TPV 1	Development of Solid Particle Separators for Plasma Exhaust	HIT
TPV 2	Optimization of the Cryogenic Vacuum Pumping of Helium	HIT
TEP 1	Cryosorption on Molecular Sieves or Alternative Cryosorbents	IRCH
TEP 2	Plasma Exhaust Processing Alternative Options	IRCH
TEP 3	Tritium Storage	IRCH
TCP 3	Atmospheric Processing	IRCH
<b><u>Nuclear Engineering / Basic Blanket</u></b>		
NSN 1	Neutronics Data Base for Shielding	INR

**Remote Handling / Maintenance**

RHS 1	Qualification of Standard Components	HIT
RHS 2	Material Tests for Remote Maintenance Equipment	HIT, IRE
RHS 3	Mock-up of In-Vessel Components and Test Facilities	HIT
RHI 1	Blanket Handling Device (BHD)	HIT, IRE
RHT 1	In-Vessel Handling Unit (IVHU)	HIT, IRE, IDT
RHT 2	Upgrading of Existing Force Reflecting Servomanipulators	HIT

**Safety and Environment**

SEC 3	Safety Analyses of Superconducting Magnets	IRE
SEP 1	Radioactivity Source Terms	IRE
SEP 2	Environmental Impact of Tritium and Activation Products	INR
SEA 1	Specific Safety Related Recommendations for the Design	IRE
SEA 3	Reference Accident Sequences	IRE
SEA 5	Assistance in Preparation of a Safety Report	IRE

**Blankets**

**BS - Solid Breeder Test Blankets**

BS DE-D-1	Solid Breeder Test Blanket Design	IMF III, INR
BS BR-D-1	Preparation of Ceramic Breeder Materials	IMF III
BS BR-D-2	Characterization	IMF III
BS BR-D-3	Irradiation Testing	IMF III
BS BR-D-4	Tritium Release	INR
BS BR-D-5	Physical and Mechanical Properties	IMF I
BS BR-D-6	Compatibility	IMF I
BS BR-D-7	Constitution, Interaction with Water Vapour	IMF I
BS BR-D-8	Thermomechanical Characterization	IRCH
BS NN-D-1	Helium Blanket Test Loop	IMF III, INR

**BL - Liquid Metal Test Blankets**

BL DE-D-1	Liquid Metal Test Blanket Design	IMF III, INR, IRB
BL PC-D-1	Corrosion of Structural Materials in Flowing Pb-17Li	IMF III
BL EX-D-1	Tritium Extraction by Permeation and Cold Trapping	IRB
BL EX-D-2	Tritium Extraction by Solid Getters	HIT
BL MH-D-1	Liquid Metal MHD	IRB

**Long Term Program**

LAM 2.1	LAM Element Activation	IMF II
LAM 3	Development of Low Activation Ferritic-Martensitic Steels	IMF II
LAM 5	Development of Non-Ferrous Low Activation Alloys	IMF II
MAT 1.6	Characterization and Qualification of 1.4914 NET Heats MANET 1 and 2	IMF II
MAT 1.9	Pre- and Post-Irradiation Fatigue Properties of 1.4914 Martensitic Steel (MANET)	IMF II
MAT 1.11	Post-Irradiation Fracture Toughness of MANET Steel	IMF II
MAT 2.2	In-Pile-Creep-Fatigue Testing of MANET	IMF II, IMF III
MAT 9.2	Investigation of Fatigue under Dual-Beam Irradiations	IMF II

**Development of ECRH Power Sources**

ITP, IDT

**Appendix II: Table of NET Contracts**

Theme	Contract No.	Working Period
Electrical Connectors for Remote Handling	313/88-7 FU-D/NET	09/88 - 05/89
Study of a Plasma Exhaust Purification System for NET Based on Catalytic Reduction of Impurities: Phase 2 - Engineering Study	322/88-8/FU-D/NET	10/88 - 10/89
NET Remote Workstation	332/88-11 FU-D/NET	12/88 - 11/89
Doses due to Tritium Releases by NET-Data Base and Relevant Parameters	364/89-2/FU-D/NET	3/89 - 8/89
Fatigue Characterization of Jacket Materials at 4 K	372/89-4/FU-D/NET	5/89 - 6/90
Doses due to Activation Product Releases by NET Plasma Facing Components - Review and Procurement of Data Base	377/89-5/FU-D/NET	6/89 - 12/89
Vacuum Pumping Support	394/89-8/FU-D/NET	9/89 - 12/90

**Appendix III: KfK Departments contributing to the Fusion Project**

Kernforschungszentrum Karlsruhe GmbH Telephone (07247) 82-1  
 Postfach 3640 Telex 17 724 716  
 D-7500 Karlsruhe 1 Telefax/Telecopies (0) 07247/825070  
 Federal Republic of Germany

KfK Department	KfK Institut/Abteilung	Director	Ext.
Institute for Data Processing in Technology	Institut für Datenverarbeitung in der Technik (IDT)	Prof. Dr. H. Trauboth	5700
Institute for Materials and Solid State Research	Institut für Material- und Festkörperforschung (IMF)	I. Prof. Dr. K.-H. Zum Gahr	3897
		II. Dr. K. Anderko	2902
		III. Prof. Dr. K. Kummerer	2518
		IV. Prof. Dr. D. Munz	4815
Institute for Neutron Physics and Reaktor Engineering	Institut für Neutronenphysik und Reaktortechnik (INR)	Prof. Dr. G. Keßler	2440
Institute for Reaktor Components	Institut für Reaktorbau- elemente (IRB)	Prof. Dr. U. Müller	3450
Institute for Radiochemistry	Institut für Radiochemie (IRCH)	Prof. Dr. H. J. Ache	3200
Institute for Reaktor Development	Institut für Reaktor- entwicklung (IRE)	Prof. Dr. D. Smidt	2550
Central Engineering Department	Hauptabteilung Ingenieur- technik (HIT)	Dr. H. Rininsland	3000
Institute for Technical Physics	Institut für Technische Physik (ITP)	Prof. Dr. P. Komarek	3500
Institute for Meteorology and Climate Research	Institut für Meteorologie und Klimaforschung	Prof. Dr. F. Fiedler	2093
Project Division Plant	Projektbereich Anlagen (PBA)	Dr. Engelhardt	2057
Central Experimental Engineering Department	Hauptabteilung Versuchstechnik (HVT)	Dr. Schubert	2114
- Hot Cells	- Heiße Zellen	DI. Enderlein	3650
- Tritium Laboratory Karlsruhe	- Tritiumlabor Karlsruhe	DP. Jourdan	2514

Appendix IV: Fusion Project Management Staff

<b>Project Manager</b>	Dr. J. E. Vetter	ext. 5460
Secretariat:	Fr. I. Sickinger	ext. 5461
	Fr. I. Pleli	ext. 5466
<b>Project Administration, Documentation</b>	BW G. Kast	ext. 5462
<b>Studies, NET Contacts</b>	Dr. J.E. Vetter	ext. 5460
<b>Blanket Development and Test Facilities</b>	DI H. Sebening	ext. 5464
<b>Superconducting Magnets Gyrotron Development</b>	Dr. J.E. Vetter	ext. 5460
<b>Tritium Technology Structural Materials</b>	Dr. H.D. Röhrig	ext. 5463
<b>Safety and Environmental Impact, Remote Handling</b>	DI A. Fiege	ext. 5465

Address: Kernforschungszentrum Karlsruhe GmbH, Nuclear Fusion Project Management

Post Office Box 3640, D 7500 Karlsruhe / Germany

Telephone No: 07247-82- Extensions .....

Telefax No: 07247 - 82 - 5467

Telex No: 17 724 716